Diffuse Radio Emission and Magnetic Fields in Galaxy Clusters

Dissertation

zur Erlangung des akademischen Grades

Doctor rerum naturalium (Dr. rer. nat.)

vorgelegt dem Rat der Physikalisch-Astronomische-Fakultät

der Friedrich-Schiller-Universität Jena

eingereicht von **M.Sc.-Phys. Kamlesh Rajpurohit**

geboren in Mount Abu, India

Name: Kamlesh Rajpurohit

Geboren: Mount Abu, India

1. Gutachter: Prof. Dr. Artie Hatzes
                                Thüringer Landessternwarte Tautenburg

2. Gutachter: Prof. Dr. Annalisa Bonafede
                                INAF/Istituto di Radioastronomia, Bologna

3. Gutachter: Prof. Dr. Harald Lesch
                                Ludwig Maximilian University of Munich

Abstract

Observations at radio wavelengths demonstrate the existence of cosmic rays and magnetic fields in the Universe. Studies of galaxy clusters have revealed sources of diffuse radio emission associated with the merger driven shocks and turbulence in the ICM: relics and halos. This thesis present the results obtained from deep radio observations of two individual galaxy clusters.

The galaxy cluster 1RXS J0603.3+4214 hosts a bright relic, known as the Toothbrush, and a giant radio halo. The cluster was observed with the VLA covering a frequency range of $1-2\,$GHz.

The new VLA images provide an unprecedented view of the Toothbrush, revealing enigmatic filamentary structures. The complexity of the filamentary structures rule out the fact that relics are caused by a smooth shock surface. In L-band, the handle of the Toothbrush is strongly polarized, as high as 60 %, while the "brush" is almost completely depolarized. The fractional polarization in the "handle" decreases only moderately towards longer wavelength. Rotation Measure (RM) synthesis analysis reveals that the filamentary features in the low density region (B3) show a shift in RM of $\sim 30\,\mathrm{rad\,m^{-2}}$ while in the denser region (B2), the shift in RM increases to $\sim 50\,\mathrm{rad\,m^{-2}}$.

The VLA observations confirm the presence of extended halo. The average spectral index of the halo is -1.16 ± 0.05. The southern part of the halo is steeper and is possibly related to a shock. Excluding the southernmost part, the halo morphology is strikingly similar to the X-ray morphology. The sensitive high resolution radio maps also reveal thirty-two previously undetected compact sources within the halo region.

For another cluster CIZA J0649.3+1801, we confirm the presence of a diffuse emission source. The cluster was observed with the WSRT. The source is polarized, has a steep spectrum, and shows a hint of spectral gradient towards the cluster center. This evidence suggests that it is a radio relic.

Abstrakt

Radiobeobachtungen bestätigen immer wieder aufs Neue die Existenz von kosmischer Strahlung und Magnetfeldern im Universum. Studien über Galaxienhaufen haben Quellen diffuser Radioemission entdeckt, welche mit dem Haufengas assoziiert sind: relikte und halos. Diese Arbeit zeigt die Ergebnisse der tiefen Radiobeobachtungen von zwei verschmelzenden Galaxienhaufensystemen.

Der Galaxienhaufen 1RXS J0603.3+4214 zeigt ein leuchtkräftiges Radiorelikt, bekannt als Toothbrush, und einen ausgedehnten, riese Radiohalo. Das System wurde mit dem VLA im Frequenzbereich von $1-2\,$GHz beobachtet.

Die in dieser Arbeit erstellten Bilder zeigen das Toothbrush in einem bisher unerreichten Detail. In diesen Bildern sind die faszinierenden filamentartigen Strukturen des Relikts sichtbar. Die Polarisationsanalyse zeigt erstmals, dass 'der Griff' (B3) des Toothbrush im Bereich von $1-2\,$GHz stark polarisiert ist. 'Die Bürste' hingegen ist fast vollständig depolarisiert. Der Polarisationsgrad in der Region geringerer Dichte (B3) innerhalb des L-Bandes nimmt nur moderat zu längeren Wellenlängen hin ab.

Die VLA-Beobachtungen bestätigen ebenfalls die Emission eines ausgedehnten Radiohalos. Der mittlere Spektralindex von des halos beträgt $-1,16 \pm 0,05$. Der südliche Teil des Radiohalos weist ein steileres Spektrum auf und steht wahrscheinlich direkt mit einer Stoßfront im Zusammenhang. Ausgenommen dieses südlichen Teils ähnelt die Morphologie des Radiohalos auffällig der Morphologie im Röntgenbereich. Die hohe Güte der Radiokarten erlaubt die Detektion mindestens dreiundzwanzig zuvor unbekannter kompakter Radioquellen.

Der Galaxienhaufen CIZA J0649.3+1801 wurde mit dem WSRT im L-band beobachtete. Diese Beobachtungen bestätigen die Existenz einer diffusen Quelle. Die Quelle hat ein steiles Radiospektrum, polarisiert und zeigt Hinweise eines Spektralindexgradienten zum Haufenzentrum hin. Wir klassifizieren diese Quelle als Radiorelikt.

Acknowledgements

First and foremost I am extremely grateful to my supervisor Dr. Matthias Hoeft for the invaluable guidance and advice he has provided throughout my research work. His vast experience and knowledge has helped me immensely in learning the subject. I would like to thank him for encouraging my research, providing me every bit of guidance and for allowing me to grow as a researcher. I quite simply cannot imagine a better supervisor. I convey my sincere gratitude to Dr. Reinout van Weeren for his valuable scientific help and concise comments on my research work. I thank him for responding to my questions and queries so promptly despite his busy schedules. I consider it as a great opportunity to perform the VLA data reduction part under his guidance and to learn from his research expertise.

I thank Prof. Artie Hatzes, Director, Thüringer Landessternwarte Tautenburg (TLS), for the academic support and the facilities provided to carry out my research work. I shall express my special thanks to Prof. Helmholtz Meusinger for reading my thesis. His feedback have been absolutely invaluable.

The members of the radio group: Dr. Alexander Drabent, Cosmos Dumba, and Jakob Gelszinnis, have contributed immensely to my personal and professional time at TLS Tautenburg. I am indebted to them for their continuous help throughout this work. I would like to thank Bernd Fuhrmann for providing computer facilities and fixing software related issues. I also thank the rest of the faculty and staff at TLS for being very amibale and helpful in all respect. I thank my fellow research students at TLS for all their help and co-operation. My special appreciation goes to my dearest friend and office room mate Silvia Sabotta for all the help, support and friendly advice, in particular related to the University paper work. This work would not be possible without her constant help. I will never forget her kindness.

I am deeply thankful to my family, my mother, my brother Dr. Arvind Rajpurohit, and my sister, who supported me in every possible way to see the completion of this work. I dedicate this work to my mother and my brother, their role in my life was, and remains, immense. Thanks for all the love, sacrifices, and encouragement throughout my life.

Contents

List of Figures

List of Tables

List of Abbreviations

AGN	Active galactic nucleus
CASA	Common Astronomy Software Applications
CRe	Cosmic ray electrons
CRs	Cosmic rays
DSA	diffusive shock acceleration
EFD	External Faraday dispersion
FD	Faraday dispersion
FWHM	full width at half maximum
GMRT	Giant Metrewave Telescope
IC	Inverse Compton
ICM	Intracluster medium
IFD	Internal Faraday dispersion
LOS	Line of sight
LAS	Largest angular size
LOFAR	Low Frequency Array
LLS	Largest linear size
NVSS	NRAO VLA Sky Survey
PyBDSF	Python Blob Detector and Source Finder
RM	Rotation Measure
rms	root mean square
RMSF	Rotation measure spread function
RFI	radio-frequency interference
VLA	Karly Jansky Very Large Array
WSRT	Westerbork Synthesis Radio Telescope
ZOV	Zone of Avoidance

List of Symbols

c	speed of light
ω	angular frequency
α	spectral index
α_{inj}	injection spectral index
α_{int}	integrated spectral index
$\mathcal{M}$	Mach number
σ_{rms}	rms noise level
v_{shock}	speed of the shock
ψ	polarization angle
ϕ	Faraday depth
B	magnetic field
E	electric field
z	redshift
b	galatic latitude
m	polarization fraction
S_ν	flux density at frequency ν
ν	frequency
λ	wavelength
T	temperature
L_{x}	X-ray luminosity
n_{e}	electrons density
G	Gauss
μ	micro
σ_{T}	Thomson cross-section
σ_{RM}	dispersion in Rotation Measure
ν_{c}	critical frequency
g_{ff}	Gaunt factor
γ	Lorentz factor
C	compression radtio
ψ_{int}	intrinsic polarization angle
$F(\phi)$	Faraday dispersion
$R(\phi)$	Rotation Measure Spread Function

Chapter 1

Introduction

The primary targets of the research carried out in this thesis are large scale diffuse radio emission sources observed in galaxy clusters. In this chapter, we give an overview of galaxy clusters, their properties, and the physics of relevant emission mechanisms. The multi-wavelength observations of galaxy clusters provide interesting insights into cluster physics, in particular about diffuse radio emission. Since the majority of the work presented in the present thesis is based on radio observations, the synchrotron emission is discussed in detail in this chapter. The remaining part of the present thesis is structured as follows:

In Chapter 2, we introduce diffuse radio emission, namely radio relics, radio halos, and radio mini-halos. We review their properties and describe the underlying acceleration mechanisms responsible for the origin of these large scale structures.

In Chapter 3, 4, 5, 6, and 7, we present the deep Karl G. Jansky Very Large Array (VLA) observations of the merging galaxy cluster 1RXS J0603.3+4214. These observations were performed with four principal questions in mind: (i) to understand the origin of diffuse radio emission; (iii) to study the total intensity features at high resolution, as high as 1 arcsec; (iii) to investigate the magnetic field structure through the polarization analysis; (iv) to measure the Rotation Measure (RM) fluctuations at high resolution using Rotation Measure Synthesis technique.

In Chapter 8, we present Westerbork Synthesis Radio Telescope (WSRT) observations of the little studied galaxy cluster CIZA J0649.3+1801. The aim was to investigate the spectral and polarization properties of a perviously detected diffuse emission source.

In the end, we summarizes the main findings of this thesis.

1.1 Galaxy clusters

The formation and evolution of large scale structures of the Universe are dominated by the flow of dark matter (i.e., an invisible material that does not emit or absorb light but can be detected through its gravitational effects), which under the action of gravity form knots, filaments, and halos, collectively known as the cosmic web (Jõeveer et al., 1978; Springel et al., 2005). The baryonic matter moves in the gravitational potential

of the dark matter distribution, along these cosmic filaments. At the intersection of cosmic filaments, where the densest concentrations of dark matter exist, lie the largest virialized systems in the Universe: massive clusters of galaxies.

Galaxy clusters are the most massive, gravitationally bound systems in the Universe. They are characterized by masses of the order of $10^{14}-10^{15}M_\odot$ and sizes of the order of $1-4\,\mathrm{Mpc}$ [1]. (Ettori et al., 2013). Galaxy clusters form by accretion of gas and by mergers with other clusters and galaxy groups.

Observations of galaxy clusters in different bands of the electromagnetic spectrum can probe different structural components. From optical observations, we can study the tens to thousands of galaxies, concentrated in large over-density regions that make up a cluster. Weak gravitational lensing allow us to study the distribution of mass in clusters through the coherent distortion it produces on the images of background galaxies (Clowe et al., 2006). Indeed, it is well known that 70%−80% of the cluster mass is in the form of dark matter. The remaining mass is baryonic matter, distributed among galaxies (2%−3%) and a hot plasma, the so called intracluster medium (ICM) (see Section 1.2), which typically represents 15%−25% of the cluster mass. The X-ray observations provide information about the ICM and the dynamical state of a cluster. In recent years, a large number of clusters has been detected in the microwave regime using the Sunyaev-Zel'dovich (SZ) effect, a result of cosmic microwave background (CMB) photons interacting with the energetic ICM electrons (Sunyaev and Zeldovich, 1972).

The comic rays electrons (CRe) and magnetic fields in clusters can be studied through radio observations. Cluster radio emission is mainly the result of synchrotron radiation, indicating the presence of magnetic fields and comic rays (CRs) in the emission region. Cosmic rays exist in the jets and lobes originating from active galactic nuclei (AGN), but there is also a population of CRs permeating the ICM that is not associated with individual galaxies but has been found in the form of large scale diffuse radio emission. The primary focus of this thesis is to understand the particle acceleration mechanisms which explain the existence of these large scale diffuse radio emission in clusters and to investigate the magnetic field structure through the polarization analysis.

Diffuse radio emission is enigmatic since the cosmic ray electrons (CRe), necessary for synchrotron emission, cannot diffuse far through the ICM because the life time of the CRe is rather small compared to the diffusion time (Jaffe, 1977). This clearly indicates that somehow the electrons must be accelerated in-situ in the ICM itself. In order to understand the diffuse radio emission originating in galaxy clusters, it is important

---

[1] A parsec (pc) is the unit of distance. One parsec is about 30 trillion kilometers or over three light-years.

and crucial to understand the physics of the ICM (Section 1.2) and the magnetic field properties within the ICM (Section 1.3).

1.2 The intracluster medium

The space between galaxies in galaxy clusters is filled with a hot and diffuse gas, the intracluster medium. The galaxy clusters grow through infall of matter and merging events, creating shocks and turbulence in the ICM, which heats up the ICM to tens of millions of Kelvin ($T \sim 10^7-10^8$K, which correspond to $kT \sim 0.8-10$ keV). At such high temperatures, the ICM is completely ionized, and the radiation resulting from the collisional interactions between electrons and ions is bremsstrahlung. The bremsstrahlung emission is discussed in detail in Section 1.4.2.

The intracluster medium is observed in the X-ray regime. A typical energy range for X-ray observations is $0.1-10$ keV. The ICM emission can reach X-ray luminosities of $L_{\mathrm{X}} = 10^{43}-10^{46}$ erg s^{-1}, thus making galaxy clusters one of the most luminous object types in the Universe.

Most of the observed ICM gas has densities in the range $10^{-2}-10^{-4}$cm^{-3} (Böhringer and Werner, 2010; Ettori et al., 2013). In fact, the X-ray emission is proportional to the square of the gas density (Section 1.4.2), which means the X-ray emission is relatively concentrated and therefore can be used for cluster identification (Rosati, 1997; Ebeling et al., 1998; Reiprich and Böhringer, 2002; Böhringer et al., 2004). However, the density dependence makes it difficult to measure the emission at the outer region of the cluster, where the electron density can be as low as 10^{-7}cm^{-3}, and the emission becomes extremely faint. Therefore, X-ray observations are usually confined within r$_{500}$, i.e., the radius at which the mean mass density is 500 times the critical density.

X-ray observations allow us to study the dynamical state of a cluster by probing the morphology of the ICM. A spherically symmetric X-ray morphology with some small-scale substructures in the central region, i.e., X-ray cavities and jets, are assumed to reflect relaxed clusters (i.e., non-interacting). In relaxed clusters, the X-ray emission is strongly centrally peaked and falls off radially with the decreasing gas density. In contrast, merging clusters show an overall irregular morphology and often show two peaks in the X-ray emission, reflecting the two cores of the merging clusters.

Moreover, X-ray observations of the ICM enable us to determine the temperature of the ICM, its thermodynamic state and the abundance of chemical elements. On the basis of the temperature profiles, clusters can be divided into two categories, cool-core and non-cool-core cluster. Cool-core clusters are typically relaxed clusters, in which the

ICM gas near the centre cools and condenses (Mann and Ebeling, 2012). This results in a sharp rise in the X-ray surface brightness and a drop in the X-ray temperature at the center (core) of the cluster (Molendi and Pizzolato, 2001; Hudson et al., 2010). In addition, cool-core clusters commonly host a central AGN. Non-cool-core clusters have had their core disrupted and do not show a central drop in temperature. However, outside of the core, the temperature profile decreases slowly with radius.

1.3   Cluster magnetic fields

Magnetic fields are ubiquitous throughout the Universe and are found on all scales, from fields surrounding the planets up to fields in the intracluster medium. The existence of magnetic fields associated with the ICM in galaxy clusters is now well established. One of the direct evidences of the cluster magnetic fields is the presence of large scale diffuse radio emission in galaxy clusters.

The magnetic field plays a key role in understanding the large scale structure formation and CRs generation. The magnetic field can be investigated by different approaches based on both, the radio and X-ray observations. However, the most relevant and commonly used tracer of magnetic fields is the synchrotron radiation. The total synchrotron emission from a source provides the strength of the total magnetic field, while the linear degree of polarization is an important indicator of the structure of the magnetic field and its uniformity.

The diffuse synchrotron emission in galaxy clusters requires a coexistence of a population of GeV relativistic electrons and a magnetic field of μG level (Govoni and Feretti, 2004; Feretti et al., 2012; Brüggen et al., 2012; Ferrari et al., 2008). The radio observations show that the typical field strength in galaxy clusters are of the order of a few μG (between 1-10 μG) and fields are widespread in the ICM. In some areas, such as the cores of some clusters, the magnetic field is very strong, i.e., between $10-40\,\mu$G (Carilli and Taylor, 2002; Ferrari et al., 2008). However, simulations suggest that the mean magnetic field in galaxy clusters, voids, and cosmic filaments are of the oder of a few nG (Vazza et al., 2014).

Despite being detected in many locations throughout the cluster, the origin and evolution of the intracluster magnetic fields remains unclear. To discriminate between different models of the origin and evolution of the intracluster magnetic field, the comparison with observations plays a key role.

1.4   Emission mechanisms in galaxy clusters

Galaxy clusters are observed through their constituent galaxies and the ICM. The ICM emission coming from the thermal pool of electrons is mainly due to bremsstrahlung while the relativistic electron population generates synchrotron and IC emission. In this section, we briefly summarize the relevant emission mechanisms:

1.4.1   Synchrotron radiation

In the radio regime, synchrotron emission (i.e., magnetobremsstrahlung for ultra-relativistic particles) is one of the most prevalent form of emission in astronomical objects, which is generated when a relativistic, charged particle undergoes acceleration in the presence of a magnetic field. In galaxy clusters, synchrotron emission is found in radio galaxies, i.e., currently active galaxies or in the lobes of formerly active ones, as well as in regions of diffuse radio emission.

The emitted power for a relativistic particle of charge e under an acceleration a is given by the Larmor's formula

$$P = \frac{2e^2}{3c^3}|a|^2 = \frac{2e^2}{3c^3} \times \left(\frac{evB}{mc}\right)^2 = \frac{2}{3c}r_0^2\gamma^2 B^2 |\mathbf{v}|^2 \sin^2\theta. \tag{1.1}$$

The electrons in a magnetic field usually have a wide range of pitch angles (θ). Assuming an isotropic distribution and integrating over all pitch angles yields the total power emitted

$$P \approx \frac{4}{3}\sigma_T c\gamma^2 U_B, \tag{1.2}$$

where $\sigma_T = (8\pi/3)r^2$ is the Thomson cross-section of the electron and $U_B = B^2/(8\pi)$ is the energy density of the magnetic field.

The synchrotron lifetime (t) of the electrons of energy E is given by

$$t = \frac{E}{P} = \frac{m_e c}{\frac{4}{3}\sigma_T \gamma U_B}. \tag{1.3}$$

For typical extended powerful radio source, $\gamma \sim 10^3$ and $B \sim 0.1\,\mu$G, so the lifetime of the electrons are expected to be $t \leq 10^7 - 10^8$ years.

The synchrotron radiation is strongly beamed in the direction of the motion of the particle, resulting in a cone of radiation with an opening angle that is inversely proportional to the Lorentz factor, i.e., $\theta \approx 1/\gamma$, which can thus be tiny. Consequently, an external observer does not have a continuous view, but only sees radiation from a

relativistic electron when the beam sweeps over the line of sight. The corresponding frequency, known as critical frequency (ν_c), is given by

$$\nu_c = \frac{3}{2}\gamma^2 \frac{eB}{m_e c} \sin\theta. \tag{1.4}$$

The critical frequency corresponds to the duration of pulses, and therefore represents the largest frequency in the synchrotron spectrum. The spectrum of an individual electron peaks near the critical frequency. Above the critical frequency, the spectrum falls rapidly. Note that $\nu_c \propto \gamma^2 \propto E^2$ (where E is energy), so the high energy electrons radiate at higher frequencies. The beaming of the radiation has a very important effect on the observed spectrum emitted by the electron.

1.4.1.1   Spectrum for a distribution of electrons

The electrons which emit synchrotron radiation have a (wide) range of energies. The number density of electrons with energy between E and $E + dE$ is a power-law and can be written as

$$dN(E) = \kappa E^{-p} dE. \tag{1.5}$$

where κ is a normalization factor.

The synchrotron emissivity can be approximated to ([Longair, 1981](#))

$$j(\nu) = \frac{2\sigma_T c}{3\mu_0 (m_e c^2)^{p-1}} \kappa B^{\frac{(p-1)}{2}} \nu^{\frac{-(p-1)}{2}} \tag{1.6}$$

The important result of Equation 1.6 is that in the synchrotron emission regime, the brightness decreases with increasing frequency.

The resulting synchrotron spectrum, constructed by summing the contribution from the individual electrons, is a power-law in frequency according to the relation

$$S(\nu) \propto \nu^{-\alpha}, \tag{1.7}$$

where S_ν is the flux density at frequency ν and α is the spectral index which depends only on the exponent of the electrons distribution such that

$$\alpha = \frac{(p-1)}{2}. \tag{1.8}$$

1.4.1.2 Polarization characteristics

An important characteristic of synchrotron emission is its polarization. For an isotropic distribution of electrons, following a power-law energy distribution, the linear degree of polarization of synchrotron emission is given by

$$\Pi = \frac{p+1}{p+\frac{7}{3}} \frac{B_0^2}{B_0^2 + B_t^2}, \tag{1.9}$$

where B_0 and B_t are the ordered and the turbulent magnetic field components, respectively.

Typically, the spectral index in the range of -0.5 to -2, flatter spectra are seldom and steeper spectra are too faint. Therefore, the maximum fractional linear polarization achievable is roughly between $73\% - 75\%$.

The polarization state of the electromagnetic radiation is described by Stokes parameter (I, Q, U, and V), first defined by George Gabriel Stokes in 1852. The Stokes parameter I gives the total intensity, Q and U contains information about the linear polarization while V contains information about the circular polarization.

In radio astronomy, Stokes V has a very small value and thus can be neglected. Therefore, the degree of linear polarization is given by

$$\Pi = \frac{\sqrt{Q^2 + U^2}}{I}. \tag{1.10}$$

Finally, the polarization angle can be determined from Stokes Q and U

$$\psi = \frac{1}{2} \tan^{-1} \left(\frac{U}{Q} \right). \tag{1.11}$$

The polarization angle provides information about the orientation of the observed electric field perpendicular to the line of sight.

1.4.2 Thermal Bremsstrahlung

Bremsstrahlung is the term for radiation that is produced when a charged particle (e.g., an electron) is deflected through the Coulomb interaction with another charged particle (e.g., an ion). Thermal bremsstrahlung is produced when the relative motion of the charged particles is due to the fact that they are in a hot gas that is fully or partially ionized with a Maxwellian distribution of electron energies.

From an astrophysical point of view, the thermal bremsstrahlung is the dominant continuum emission mechanism of thermal plasmas, such as the X-ray emission from the ICM in galaxy clusters and the radio emission from HII regions in galaxies.

Consider a gas with a number density n_e of the free electrons (each with charge $-e$) and a number density n_i of the positively charged ions (each with charge $+Ze$). If the electrons are moving relative to the ions, with a typical velocity v, the gas will emit bremsstrahlung radiation with a specific intensity

$$I = v^{-1} Z^2 n_e n_i g_{\text{ff}}(\nu, v), \tag{1.12}$$

where $g_{\text{ff}}(\nu, v)$ is the Gaunt factor. If the relative motion of the electrons and ions is due to thermal motions, we expect that $v^2 \sim kT/m_e$, and thus

$$I = T^{-1/2} Z^2 n_e n_i g_{\text{ff}}(\nu, T), \tag{1.13}$$

where T is temperature and k is the Boltzmann constant. More precisely, an integration over the Maxwell distribution of the electron velocities at a given temperature yields the relevant equation for the spectrum (Rybicki and Lightman, 1979)

$$\epsilon_\nu = \frac{2^5 \pi e^6}{3 m_e c^3} \left(\frac{2\pi}{3 m_e k} \right)^{1/2} Z^2 n_e n_i T^{-1/2} g_{\text{ff}} e^{\frac{-h\nu}{kT}}. \tag{1.14}$$

1.4.3 Inverse Compton Scattering

The scattering of the low energy photons to higher energies by relativistic electrons is called inverse Compton (IC) scattering. Here, the photon gains energy while the electron loses energy. The process is called inverse because the charged particle, i.e., an electron, loses energy rather than the photon, which is just opposite to the standard Compton scattering.

In a variety of astrophysical processes, the IC scattering is one of the principle emission mechanisms, e.g., in pulsars, AGN and in extended sources like supernova remnants. It is also important in galaxy clusters since the cosmic ray electrons propagate through the radiation field of the CMB and lose part of their energy through IC scattering. However, it is really difficult to distinguish between synchrotron and IC losses, based on the shape of the radio spectrum alone, as both of these radiation have similar energy dependencies.

After discussing the main emission mechanisms of interest, it is prudent to consider loss mechanisms. There are two principal mechanisms which are important when considering radio emission from clusters, namely synchrotron and inverse Compton losses.

1.5 Radiation losses

The high energy particles undergo a number of energy-loss processes as they propagate. These energy-loss processes deform the energy distribution of electrons from the original acceleration spectrum. The energy dependencies of the energy-loss rate determine the spectral deformation. The energy-loss rate of a single particle, as a function of the Lorentz factor, is given by

$$b(\gamma) = -\left(\frac{d\gamma}{dt}\right).$$

(1.15)

According to Equation 1.15, the instantaneous timescale for particle losses can be defined as

$$t_{loss} = \frac{\gamma}{b(\gamma)}.$$

(1.16)

The CRe lose their energy by emitting Coulomb, synchrotron, bremsstrahlung, and IC radiation. Generally, at low energies, the energy-loss of electrons is dominated by Coulomb collisions due to collisions between the thermal electrons (Rephaeli, 1979), see left panel of Figure 1.1. The loss-rate due to the Coulomb collision is given by

$$b(\gamma)_{\mathrm{coulomb}} \simeq 1.27 \times 10^{-12} n_e \left[1.0 + \frac{\ln(\gamma/n_e)}{75}\right] \mathrm{s}^{-1}.$$

(1.17)

For galaxy clusters, the thermal electron density is typically of the order of $10^{-7} \mathrm{cm}^{-3}$. In a very low density limit, the loss rate due to bremsstrahlung is (Blumenthal and Gould, 1970)

$$b(\gamma)_{\mathrm{bremss}} \simeq 1.51 \times 10^{-16} n_e \gamma \left[\ln(\gamma) + 0.36\right] \mathrm{s}^{-1}.$$

(1.18)

As shown in Figure 1.1 left panel, the intermediate energy regime is mainly dominated by bremsstrahlung loses.

At higher energies, synchrotron radiation becomes an important channel to lose energy radiatively. Galaxy clusters are filled with a large scale magnetic field which plays a crucial rule for the energy losses. The expression for the loss rate due to synchrotron
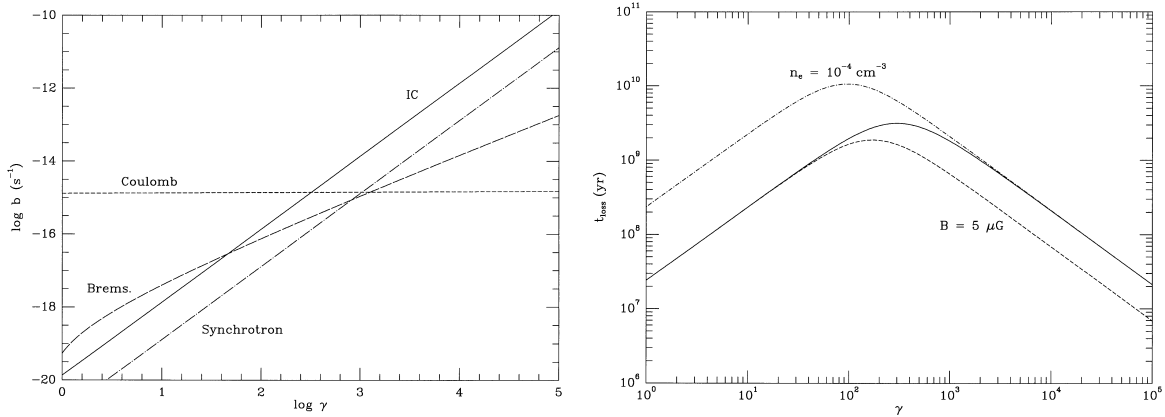
Figure 1.1: *Left*: Energy losses $b(\gamma)$ as a function of γ for inverse Compton emission, Coulomb losses, synchrotron losses, and bremsstrahlung losses. Both the figures are taken from (Sarazin, 1999). The solid curve gives values assuming an average electron density $n_{\mathrm{e}} = 10^{-3}\,\mathrm{cm}^{-3}$ and a magnetic field of $B = 1\mu\mathrm{G}$. *Right*: Instantaneous loss timescale t_{loss} as a function of γ, assuming an electron density $n_{\mathrm{e}} = 10^{-3}\,\mathrm{cm}^{-3}$, a magnetic field of $B = 1\,\mu\mathrm{G}$ (solid curve) and $B = 5\,\mu\mathrm{G}$ (dashed curve). The dot-dashed curve assume an electron density $n_{\mathrm{e}} = 10^{-4}\,\mathrm{cm}^{-3}$ and a magnetic field of $B = 5\,\mu\mathrm{G}$.

radiation is given by (Rybicki and Lightman, 1985)

$$b(\gamma)_{\mathrm{synch}} \simeq 1.3 \times 10^{-21} \gamma^2 \left(\frac{B^2}{1\mu\mathrm{G}} \right) \mathrm{s}^{-1}. \tag{1.19}$$

The effect of the magnetic fields on the energy spectrum is shown in right panel of Figure 1.1. An increase in the magnetic field, for instance to $B = 5\,\mu\mathrm{G}$, results in an increase in the energy losses at high energies with shortened timescale (dashed curve). However, if the electron density is lowered, for instance to $n_{\mathrm{e}} = 10^{-4}\,\mathrm{cm}^{-3}$, then the loss time increases and the losses at lower energies get reduced (dot-dashed).

The loss rate for IC scattering is

$$b(\gamma)_{\mathrm{IC}} \simeq 1.37 \times 10^{-20} \gamma^2 (1 + z)^4 \,\mathrm{s}^{-1}. \tag{1.20}$$

Note that IC losses are independent of the magnetic field of the cluster. Finally, the ratio between IC and synchrotron losses is given by

$$\frac{b(\gamma)_{\mathrm{sync}}}{b(\gamma)_{\mathrm{IC}}} \simeq 0.095(1 + z)^{-4} \left(\frac{B}{1\mu\mathrm{G}} \right). \tag{1.21}$$

Hence, if the magnetic field is not too strong then IC losses will dominate over synchrotron losses. Evidence of IC losses is provided by detections of hard (i.e., high energy) X-rays from the ICM, and has also been detected in the lobes of Fanaroff-Riley galaxies (Croston et al., 2005; Hardcastle and Croston, 2005).

Chapter 2

Diffuse non-thermal radio emission in galaxy clusters

Radio observations of galaxy clusters revealed the presence of diffuse emission that is not associated with any of the individual galaxies in the cluster. Such diffuse radio emission was first detected in the Coma cluster (Large et al., 1959). The radio spectra of such emission are steep and follow a power-law over a wide range of frequencies, suggesting synchrotron radiation to be the underlying emission mechanism.

The diffuse radio sources in galaxy clusters have been divided into three main types: **relics, halos and mini-halos**. This classification is based on their observed properties such as morphology, size, location with respect to the cluster center and polarization. Relics and halos are associated with merging clusters suggesting that the cluster merger plays a major role in their formation while mini-halos are mainly found in relaxed clusters.

In this chapter, we review the properties of diffuse radio emission sources and the physical mechanisms responsible for the large-scale radio emission that is detected in many merging clusters of galaxies. We begin with radio relics since they are the main objects of this thesis.

2.1 Radio relics

Radio relics are Megaparsec sized irregular shaped synchrotron sources that are found in peripheral regions of galaxy clusters. They are characterized by low surface brightness, a steep integrated radio spectrum ($-1.0 \geq \alpha \geq -1.6$), and a high degree of polarization (10 % to 60 % in some regions). Therefore, radio relics are unique probes of the magnetic field properties in the outskirts of galaxy clusters.

2.1.1 Classification

Radio relics show a wide variety in size, morphology and distance from the cluster center. Depending on their morphology and origin, relics are further subdivided into

three groups (Kempner et al., 2004; Ferrari et al., 2008): radio gischt, AGN relic and radio phoenix. The first class is believed to be related to merger shocks in the ICM and the other two are mainly associated with a previous AGN activity.

Radio gischt objects are generally Megaparsec sized and often show elongated arc-like morphology. They are found to spatially coincide with the X-ray detected shocks. Therefore, this class of objects are found only in merging system. One of the well-studied example of this class is the so called "Sausage relic" (van Weeren et al., 2010; Stroe et al., 2013), shown in Figure 2.1. A few galaxy clusters also show the presence of multiple extended relics located symmetrically with respect to the cluster center (Rottgering et al., 1997; Bonafede et al., 2009; Bonafede et al., 2012; Bonafede et al., 2017).
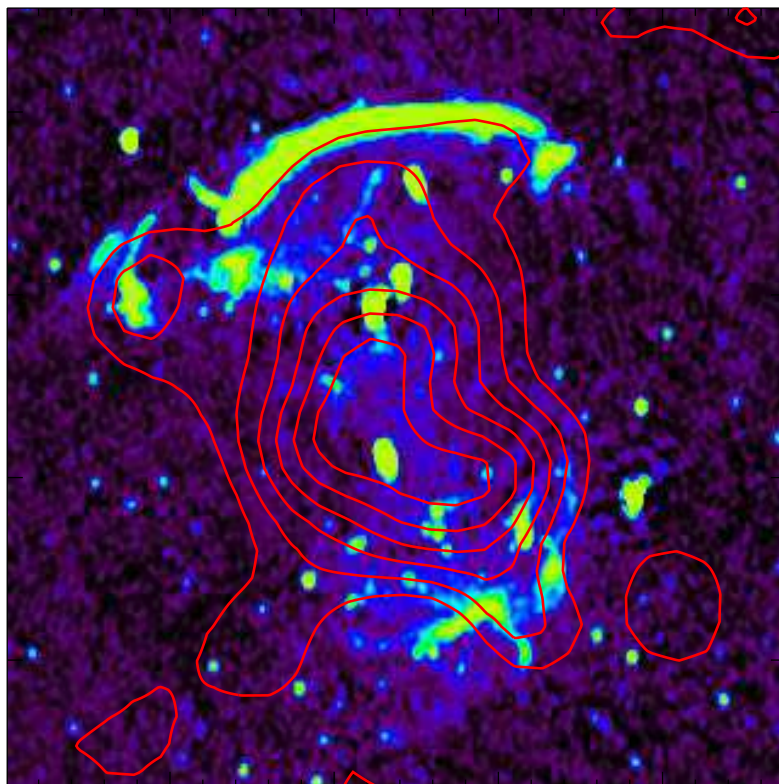
Figure 2.1: The radio relic in CIZA J2242.8+5301. Observation at 1.4 GHz in colors, X-ray surface brightness in red contours. (Figure adopted from van Weeren et al., 2010).

Radio phoenix objects are smaller in size, have curved and steeper spectra, and a lobe-like of morphology. They are thought to be related to the fossil radio plasma ejected in the past by AGN, which has been re-energized via the process of adiabatic compression (Enßlin and Gopal-Krishna, 2001; Enßlin and Brüggen, 2002).

AGN relic objects are remnants of radio galaxies where the AGN activity maintaining the lobes is switched off, leaving the radio plasma (Komissarov and Gubanov, 1994) that emits at radio frequencies.

In this thesis, we focus on so-called radio gischt relics that show up to 1 Mpc or larger and are related to the shocks in the ICM.

2.1.2 Origin of radio relics

There is strong evidence that relics are connected with shock fronts induced by cluster mergers (see Brunetti and Jones, 2014, for a review). It is widely accepted that the source of the radio emission is a population of relativistic electrons, emitting at the location of the shock. Because of the short radiative lifetime of relativistic electrons, the radio emission must only be produced close to the location of the shock, which is consistent with the geometry of the observed relics, i.e., an elongated shape perpendicular to the merger axis. These shocks are capable of accelerating particles to the higher energies (Blasi, 2000; Miniati et al., 2000; Fujita and Sarazin, 2001; Ryu et al., 2003).

The X-ray observations allow us to estimate the strength of a shock front via temperature and X-ray surface brightness jump. The dimensionless number that characterizes the strength of a shock is the Mach number ($\mathcal{M}$), which is the ratio of the upstream shock velocity and the speed of sound in the ICM, i.e., $\mathcal{M} = v_{\mathrm{shock}}/c_{\mathrm{s}}$. For several radio relics, the jump related to the shock in X-ray surface brightness and temperature has been identified (Sarazin et al., 2013; Stroe et al., 2013; Shimwell et al., 2015; van Weeren et al., 2016; Eckert et al., 2016). The X-ray observations of galaxy clusters suggest that the Mach numbers of merger driven shocks are in the range of 2 to 4 (maxmimum).

In order to understand the origin of radio relics, it is important to investigate how particles are accelerated to relativistic energies. The particle acceleration mechanism in relics is a matter of debate because the low Mach number shocks, namely $\mathcal{M} \leq 3$. This implies a steep spectrum which means there are not enough electrons in the radio relevant energy regime, posing a severe challenge for the standard scenario for relics. However, the most favored particle acceleration mechanism is the diffusive shock acceleration (DSA). In the next section, we discuss the DSA in detail.

2.1.2.1 Diffusive shock acceleration mechanism

Diffusive shock acceleration is a Fermi I process where CRs interact with a shock and are accelerated to very high energies (Drury, 1983; Blandford and Eichler, 1987;

Ensslin et al., 1998; Hoeft and Brüggen, 2007; Kang and Ryu, 2011). The CRs responsible for the radio emission are effectively trapped, bounce back and forth between the upstream/pre-shock (region that the shock has not yet passed in) and downstream/post-shock regions (region that the shock has already passed) of the shock. After crossing a shock front, reflection at a moving medium increases the energy of the CRs, and after a large number of crossings, the particle is accelerated to a very high energy. In this process, both the electron and proton present in the ICM get accelerated at the shock surface. According to Equation 1.4.1, the total synchrotron power emitted by a particle is inversely proportional to the second power of the particle mass. Therefore, in a cluster lifetime, the relativistic protons lose only a small fraction of their energy. On the other hand, high energy electrons have much shorter radiative lifetime.

During the DSA process, the accelerated particles show a power law energy distribution whose spectral index is determined by the shock parameter, namely the compression ratio C. This shock parameter determines the energy distribution of the particles and the overall synchrotron spectrum (Blandford and Eichler, 1987) as

$$p_{\mathrm{inj}} = \frac{3C}{C - 1}. \tag{2.1}$$

By applying the Rankine-Hugoniot jump conditions, we get

$$p_{\mathrm{inj}} = \frac{4\mathcal{M}}{\mathcal{M}^2 - 1}. \tag{2.2}$$

The synchrotron radiation spectrum, produced by this underlying population of electrons, will have a spectral index of

$$\alpha_{\mathrm{inj}} = -\frac{1}{2} + \frac{\mathcal{M}^2 + 1}{\mathcal{M}^2 - 1}. \tag{2.3}$$

Here, α_{inj} is the injected spectral index (i.e., a spectral index of just the accelerated electrons). From Equation 2.3, we can derive the Mach number of a shock from the radio spectral index maps and can compare it with the Mach number derived from the X-ray observations. Once the relativistic electrons are injected at the shock location, they naturally lose energy in the downstream regions. Hence a clear spectral index gradient is expected towards the cluster center. Moreover, the shock also compresses the field, i.e., magnetic field vector distribution is anisotropic.

According to the DSA, for a stationary shock in the ICM (i.e., the electron cooling time is much shorter than the time scale on which the shock strengths or geometry changes), the integrated spectrum (α_{int}), is 0.5 steeper than the injection spectrum,

i.e.,

$$\alpha_{\text{int}} = \alpha_{\text{inj}} + 0.5. \tag{2.4}$$

For strong shocks, $\mathcal{M} \to \infty$ and therefore, $p_{\text{inj}} \to \infty$ (i.e., the limit of the spectral index $\alpha_{\text{inj}} \leq -0.5$). For strong shocks, the electron population is generally accelerated to higher energies, whereas for weak shocks, the electrons gain little energy before escaping downstream.

For most of the relics, the observed properties, such as the gradual spectral index steepening toward the cluster center, the high degree of polarization with magnetic field lines parallel to the source extension, and the integrated spectrum with a power-law form, can be well explained by the DSA model. However, several recent observations have challenged the DSA model. These observations have revealed that for some relics the derived X-ray Mach numbers are low, namely $\mathcal{M} \leq 2$(Akamatsu et al., 2012; van Weeren et al., 2016; Pinzke et al., 2013; Vazza and Brüggen, 2014). For such a low Mach number shocks, DSA is not efficient in accelerating cosmic ray electrons from the thermal pool to relativistic energies.
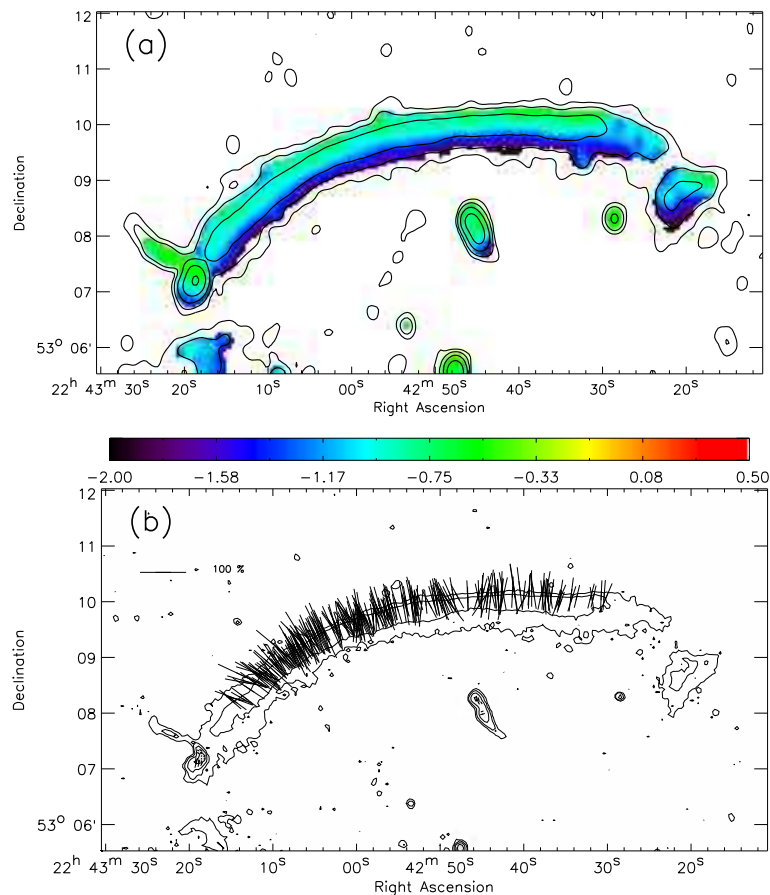
Figure 2.2: Spectral index and E-vector map of the Sausage-relic. Contours represent the total intensity emission obtained from the 610 MHz GMRT image *Top*: spectral index map between 320 MHz and 610 MHz. *Bottom*: polarization map showing the electric field vector distribution. The E-vectors are corrected for the Faraday rotation effect. (Adopted from van Weeren et al., 2010).

2.1.2.2 Alternative mechanism

To solve the low Mach number issue, several alternative models were proposed, such as the shock re-acceleration model of pre-accelerated electrons in the ICM which is a more efficient mechanism for weak shocks (Giacintucci et al., 2008; Kang and Ryu, 2011; Kang et al., 2012; Pinzke et al., 2013; van Weeren et al., 2017b; van Weeren et al., 2017a). It is speculated that AGNs in radio galaxies might provide a pool of relativistic seed electrons, which are re-accelerated through the shock. For low Mach number shocks, the re-acceleration of electrons, while passing though a shock, changes the spectrum since the fossil population is still mildly relativistic so the efficiency and spectral slope issues could be solved. Recently, van Weeren et al. (2017b) reported a clear observational evidence that a relic is found to be connected to a head-tail radio galaxy.

2.1.3 Spectral and polarization properties

Detailed studies of the spectral index distribution of radio relics, indeed, provide evidence of a gradual spectral index steepening toward the cluster center (van Weeren et al., 2012a; van Weeren et al., 2010; Stroe et al., 2013). Relics trace shock fronts which propagate outwards over the time with certain velocity. At the front of the shock, the electrons get injected into acceleration process while in the post-shock regions, we get energy losses because the accelerated electrons radiate synchrotron emission. The high energy particles lose energy faster, as a direct consequence the spectrum gets curved and the break frequency shifts downstream towards lower frequencies (i.e., the radio spectral index steepens). Hence, the spectral index maps of relics should show a spectral gradient with a flat spectrum in the front of the shock and a steep spectrum further downstream, i.e., in the post-shock region. The spectral index map of the Sausage relic is shown in Figure 2.2, where a clear spectral index gradient is visible. We see a young electron population, i.e., electrons populations associated with a flat spectral index, close to the location of the shock. In the post-shock regions, we see an old electron population associated to synchrotron emission of a steep spectral index.

Several radio relics are reported to be polarized, some with a very high polarization fraction (Bonafede et al., 2009; van Weeren et al., 2010; van Weeren et al., 2012a; Kale et al., 2012; Lindner et al., 2014; de Gasperin et al., 2015; Kierdorf et al., 2016) and the magnetic field aligned towards the relic extension. The magnetic field alignment is believed to be due to the magnetic field amplification. As a consequence, the plasma is compressed, stretched, and aligned along the shock front. Hence, the synchrotron luminosity of the region is increased and high polarization levels are expected.

2.2 Radio halos

Radio halos are diffuse, Megaparsec sized sources that are found in clusters, filling a large fraction of the cluster area (or volume). They are characterized by a low surface brightness emission and often a smooth regular shaped morphology. The surface brightness distribution of halos is, generally, peaked at the X-ray cluster center and decreases towards the cluster outskirts, see Figure 2.3. They are usually unpolarized. In fact, just two halos are currently reported to be polarized, i.e., A2255 (Govoni et al., 2005; Pizzo et al., 2011) and MACS J0717.5+3745 (Bonafede et al., 2009). Most halos are found only in merging galaxy clusters possessing X-ray substructures (Liang et al., 2000; Cassano et al., 2010; Basu, 2012; Cassano et al., 2013), suggesting that cluster mergers play a major role in their formation. The radio emission from the halo typically follows the X-ray emission from the thermal gas (Govoni et al., 2001b), indicating an association between the thermal and non-thermal components of the ICM.
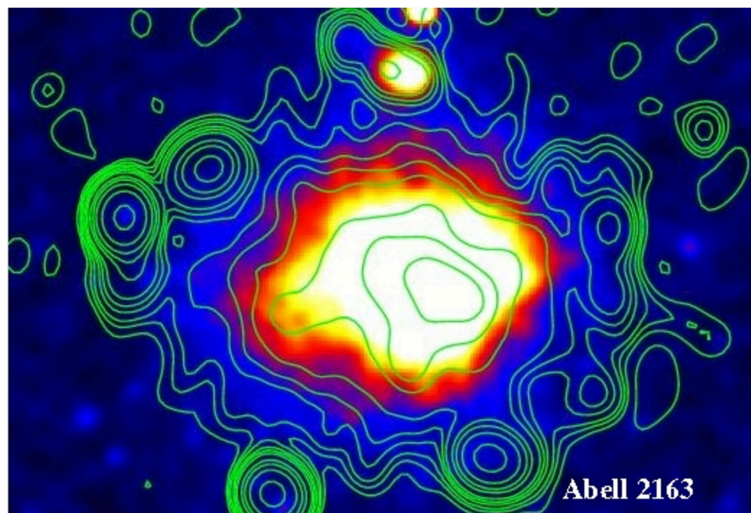
Figure 2.3: VLA 1.4 GHz image of the radio halo in Abell 2163. The radio contours are from the VLA 1.4 GHz, overlaid on the XMM-Newton image (Adopted from Feretti et al., 2001).

2.2.1   Origin of radio halos

The origin of radio halos is still under debate. However, there are two main models that have been proposed over the past two decades to explain their origin.

Primary electron (re-acceleration) model: In the primary electron model a long-lived, mildly relativistic population of electrons is re-accelerated to higher energies by magneto-hydrodynamical turbulence induced during cluster mergers (Brunetti et al., 2001; Petrosian, 2001). This relativistic electron population, which is sufficient to

produce observable synchrotron emission, is accelerated via a Fermi II process. There are some predictions from this model: (1) radio halos should be found only in merging clusters. In fact, with a few exceptions, radio halos are found only in massive merging clusters; (2) a complex radio halo morphology; (3) a complex spatial distribution of the spectral index and a radial steepening due to different re-acceleration processes in different cluster regions, and (4) a steepening of the radio halo spectrum, i.e., cut off in the halo spectrum towards higher frequencies. Consequently, a large population of ultra-steep spectrum radio halos is expected to be detected at low frequencies (Brunetti et al., 2004).

Secondary electron (hadronic) model: The secondary electron model proposes that the cosmic ray electrons (CRe) are the secondary products of the hadronic collision between thermal ions (p_{t}) and relativistic protons (p) present in the ICM (Dennison, 1980; Blasi and Colafrancesco, 1999; Dolag and Enßlin, 2000):

$$p_{\mathrm{t}} + p \rightarrow \pi^0 + \pi^{\pm} + ... \tag{2.5}$$

According to Equation 2.5, the neutral pions (π^0) decay into gamma rays, whereas the charged pions ($\pi^{\pm}$) decay into positrons and relativistic electrons. The main predictions of this model are: (1) radio halos should be found in all galaxy clusters because the relativistic protons in galaxy clusters have a lifetime greater than that of the cluster itself, so there will always be a fraction of the relativistic electrons in the ICM produced by such a hydronic collision; (2) a smooth radio halo morphology; (3) a uniform spectral index distribution of halos, and (4) the existence of gamma rays in clusters.

The non-detection of gamma rays in clusters (Jeltema and Profumo, 2011; Brunetti et al., 2012; Ackermann et al., 2014; Ackermann et al., 2016) and the prediction that radio halos should be present in almost all clusters, appears to challenge the secondary electron model.

2.3   Radio mini-halos

Radio mini-halos are steep spectrum radio sources located at the center of cool-core clusters, surrounding a dominant cluster galaxy (Feretti et al., 2012; Brunetti and Jones, 2014). They are extended on a moderate scale (up to $\sim 500\,\mathrm{kpc}$) and appear roundish. Radio mini-halos are typically found in relaxed clusters (cool-core cluster) rather than in merging clusters, making them different from the so called radio halos. The X-ray observations of galaxy clusters hosting mini-halos revealed the presence of cold fronts in the center of the cluster (Mazzotta and Giacintucci, 2008), suggesting a

possible connection between the mini-halo and the cold front. The origin of mini-halos is still unclear but they are believed to be produced by sloshing motion induced by the minor mergers, which generate turbulence in the cores of clusters and reaccelerate the relativistic electrons.

In the pervious sections, we have explained the origin and properties of radio relics and radio halos. The diffuse radio emission in galaxy clusters has been known since the seventies and during the last decade considerable progress has been achieved in our understanding of these sources. But many aspects of their origin are still puzzling. We discuss some of them in the next section.

2.4   Open questions

There is enough evidence that both relics and halos are related to the cluster merger events. During cluster formation processes, some of the energy released is channeled into merger driven shocks and turbulences that result into particle acceleration. However, recent radio observations have challenged our understanding about the relics and halos. These observations have revealed details that cannot be explained by the previously thought mechanisms. There are several open questions that needs to be answered:

- What is the origin of the radiating electrons that form the radio relics and radio halos?

- What is the main particle acceleration mechanism that accelerate particles in galaxy clusters?

- Is there any connection between the different kind of diffuse emission sources observed in galaxy clusters?

- What are the properties of the magnetic fields in the peripheral regions of galaxy clusters?

The high resolution and more sensitive observations are essential to answer the main open questions about the origin of radio relics and halos. The radio interferometers LOFAR, GMRT, and VLA are able to trace the diffuse radio emission in clusters at $\sim 1''$ to $5''$ angular resolution and are essential for comparing observations and theoretical models to gain a deeper insight.

Chapter 3

VLA observations of the galaxy cluster 1RXS J0603.3+4214

The work presented in this thesis is primarily based on observational data obtained using different radio observatories, namely Karl G. Jansky Very Large Array (VLA), Westerbork Synthesis Radio Telescope (WSRT), Giant Metrewave Radio Telescope (GMRT), and Low Frequency Array (LOFAR). Observational data of the first two facilities are calibrated and reduced while the data from other two telescopes were re-imaged according to our needs. As discussed in the last chapter, radio relics are excellently suited to understand the physics of shocks, the particle acceleration mechanisms, and the magnetic fields in low density regions of galaxy clusters. In this chapter and in the following chapters, we report the new VLA observations of the merging galaxy cluster 1RXS J0603.3+4214. The cluster 1RXS J0603.3+4214 is an important target for a detailed study of the total intensity features and cluster magnetic fields. This cluster host a spectacular bright relic that has a very unusual morphology. With the new VLA observations, we can study the radio emission at higher resolution as well as with high sensitivity.

3.1   1RXS J0603.3+4214: previous work

The galaxy cluster 1RXS J0603.3+4214, located at $z = 0.225$, was discovered by van Weeren et al. (2012a) whose followup WSRT and GMRT radio observations enabled the identification of a large steep spectrum radio source. The main peculiarity of this cluster is the large and bright northern relic, labelled as B1, B2, and B3 in Figure 3.1. It has a peculiar morphology that led to its nickname 'Toothbrush' (hereafter called as the Toothbrush). After the discovery of the Toothbrush, several multifrequency observations of this cluster have been performed.

The X-ray luminosity of 1RXS J0603.3+4214 is $L_{\rm X, 0.1-2.4\,keV} \sim 1 \times 10^{45}\,{\rm erg\,s^{-1}}$ (van Weeren et al., 2012a). The X-ray emission is mainly elongated in north-south direction, indicating that cluster is undergoing a major merger event. The weak-lensing study by Jee et al. (2016) showed that the cluster is composed of complicated dark matter substructures closely tracing the galaxy distribution. They found that the cluster mass

is dominated by two massive clumps with a mass ratio of 3:1 ($M_{north} = 6.29^{+2.24}_{-1.62} \times 10^{14} M_{\odot}$ and $M_{south} = 1.98^{+1.24}_{-0.74} \times 10^{14} M_{\odot}$).

3.1.1   Analysis of radio data

The radio observations of the cluster 1RXS J0603.3+4214 revealed that the cluster also hosts two additional fainter relics (sources E and D) and a giant radio halo (C) (van Weeren et al., 2012a). The most prominent source of this cluster is the Toothbrush. It has an unusual linear morphology, extending to about 1.9 Mpc, with three distinct components resembling the brush (B1) and the handle (B2+B3) of a toothbrush. Brüggen et al. (2012) using a hydrodynamical N-body simulation aimed for reproducing the elongated linear morphology of the Toothbrush. They showed that a triple merger between two equal mass clusters merging along the north-south axis together with a third less massive cluster moving in from the southwest may cause the peculiar shape of the Toothbrush.

Like the Sausage-relic, a clear north-south spectral index gradient has been found for the Toothbrush (van Weeren et al., 2012a). From the spectral index map between 325 and 610 MHz, an injection spectral index of -0.6 to -0.7 was obtained at the northern edge of the Toothbrush. Here, the injection spectral index means the flattest spectral index measured at the location of the shock front.

Recently, the LOFAR observation of 1RXS J0603.3+4214 revealed that the spectral index across the Toothbrush varies between -0.80 to -2.5 van Weeren et al. (2016). The obtained values were consistent with the previous spectral index estimates by van Weeren et al. (2010). However, the LOFAR observations disfavored a spectral index as flat as -0.6. According to standard DSA, the spectral index obtained from the 150 and 610 MHz corresponds to $\alpha_{inj} = -0.80$, implying a Mach number of $\mathcal{M} = 2.8^{+0.5}_{-0.3}$.

The integrated spectrum of the Toothbrush has been studied by several authors. van Weeren et al., 2012b first reported that the total spectrum follows a power law between 70 MHz to 4.9 GHz. Later, Stroe et al. (2016) studied the integrated spectrum between 150 MHz and 30 GHz, and detected a spectral break at frequencies above about 2 GHz. However, a recent study by Kierdorf et al. (2016) indicates that the spectrum can be fitted well by a single power law below 8.35 GHz, suggesting that a break in the spectrum does not exist below 8.35 GHz. Basu et al. (2016) studied the impact of the SZ effect on the observed synchrotron flux and found that the radio spectrum is affected above 10 GHz.
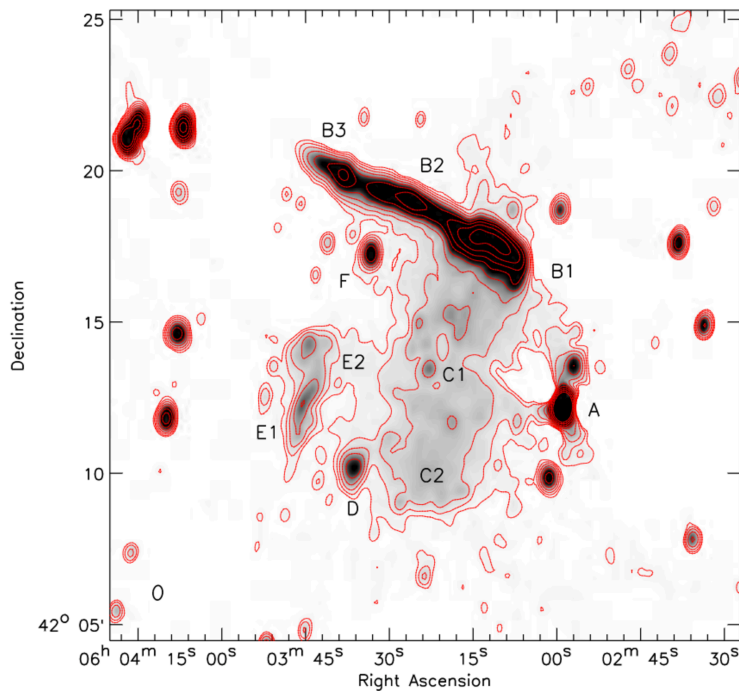
Figure 3.1: WSRT L-band image (1160-1780 MHz) of the galaxy cluster 1RXS J0603.3+4214. The cluster is known to host three relics and a giant elongated radio halo. (Figure is adopted from van Weeren et al. (2012a)).

The two smaller and fainter relics, labelled as E and D, in Figure 3.1 are located at the eastern side of the cluster and are not aligned along the merger axis. The number of relics in 1RXS J0603.3+4214, their asymmetric locations and the peculiar linear extent of the Toothbrush suggests a complex merger involving more than two sub-clusters.

3.1.2 Analysis of X-ray data

1RXS J0603.3+4214 has also been studied extensively in X-rays with the main focus on the northern part of the cluster where the Toothbrush is located. In the ROSAT All Sky Survey (Voges et al., 1999), the cluster was detected as an extended source which provided the first indication of a north-south elongation of the ICM (van Weeren et al., 2012a). After that, Ogrean et al. (2013) observed the cluster with XMM-Newton and found two distinct X-ray peaks as an evidence for a recent merger activity. They also found three density and temperature discontinuities, one to the north at the location the Toothbrush and one to the south-east, suggesting the presence of shocks in the ICM.

Recently, van Weeren et al. (2016) observed the cluster with the Chandra X-ray telescope to study the X-ray surface brightness and temperature distribution in detail. The Chandra image clearly indicates that the cluster is highly disturbed with a bimodal
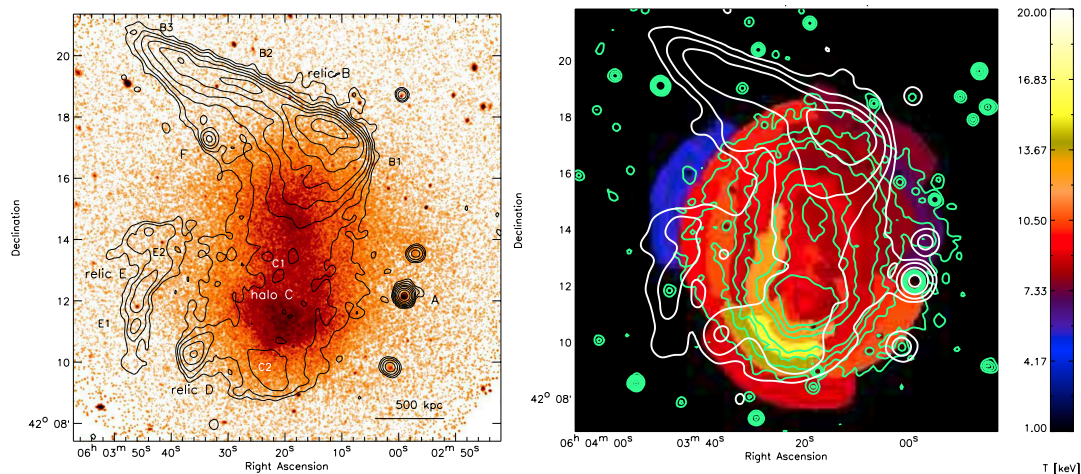
Figure 3.2: *Left*: Chandra image $(0.5 - 2.0\,\mathrm{keV}$ band) of the cluster 1RXS J0603.3+4214 overlaid with radio contours from the LOFAR image with a resolution of $17.7''$. The X-ray image is smoothed with a Gaussian of FWHM of $3''$. *Right*: X-ray temperature map in the $0.5 - 7.0\,\mathrm{keV}$ band. The X-ray contours are shown with green and the radio with white (Adopted from van Weeren et al. (2016)).

X-ray surface brightness distribution, see in Figure 3.2 top panel. These observations also unveil a third smaller, sub-cluster to the west.

The Chandra observations confirmed the presence of shock front at the location of the Toothbrush. The shock detected in Chandra via the surface brightness jump coincides with the northern edge of the Toothbrush, i.e., outer edge of the brush, see Figure 3.3 left panel. The temperature of the cluster is shown in the right panel of Figure 3.2. Surprisingly, at the location of the brush region of the Toothbrush, the temperature is not as high as expected. However, the jump in the surface brightness and temperature indicates a weak shock of Mach number of $\mathcal{M} \sim 1.2$.

Clearly, the X-ray derived Mach number of $\mathcal{M} \sim 1.2$ is much lower than the radio derived Mach number, namely $\mathcal{M} = 2.8^{+0.5}_{-0.3}$. For this particular relic, the difference in the radio and X-ray derived Mach number is significantly high. The absence of a stronger shock at the location of the Toothbrush seems a bit odd. It is puzzling how a weak shock can create a $2\,\mathrm{Mpc}$ sized large structure.

The Chandra observations also revealed another merger driven shock in the southern part of the cluster but in the radio map no relic have been found at this location. The shock is detected at the southern edge of the radio halo. The Mach number of the southern shock measured from the surface brightness and temperature jump are $\mathcal{M} = 1.39^{+0.06}_{-0.06}$ and $\mathcal{M} = 1.8^{+0.5}_{-0.3}$, respectively, see Figure 3.3 right panel.
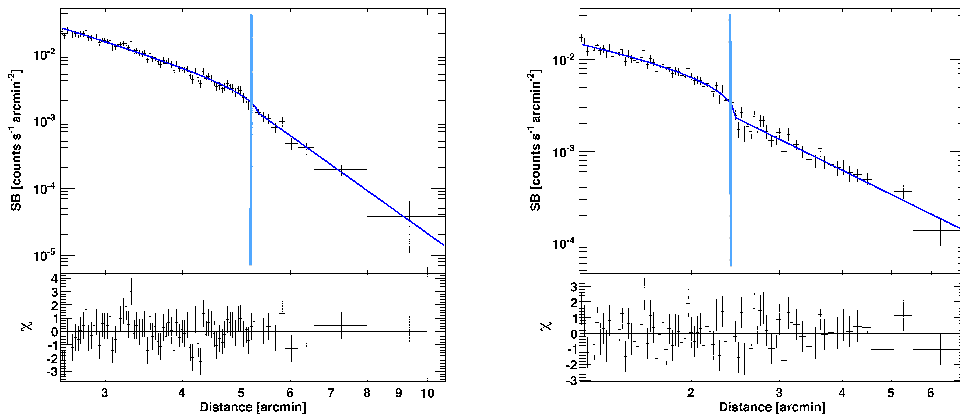
Figure 3.3: *Left*: X-ray surface brightness profile across northern edge of the Toothbrush. *Right*: X-ray surface brightness profile across the southern end of the radio halo. The blue lines show the best-fitting with a density jump as free parameter and the vertical line the outer boundary of the radio relic or halo emission. (Adopted from van Weeren et al. (2016))

Table 3.1: VLA L-band observations overview

configuration	A	B	C	D
Observation dates	Dec 8, 2012	Nov 30, 2013	June 17, 2013	Jan 28, 2013
Frequency range	$1-2\,\mathrm{GHz}$	$1-2\,\mathrm{GHz}$	$1-2\,\mathrm{GHz}$	$1-2\,\mathrm{GHz}$
Integration time	$1\,\mathrm{s}$	$3\,\mathrm{s}$	$5\,\mathrm{s}$	$5\,\mathrm{s}$
On source time	$4+4\,\mathrm{hr}$	$8\,\mathrm{hr}$	$6\,\mathrm{hr}$	$4\,\mathrm{hr}$
No. of IFs	16	16	16	16
No. of channels	64	64	64	64
channel width	$1\,\mathrm{MHz}$	$1\,\mathrm{MHz}$	$1\,\mathrm{MHz}$	$1\,\mathrm{MHz}$
polarization	all Stokes	all Stokes	all Stokes	all Stokes
Flux calibrator	3C147	3C147	3C147	3C147
Polarization calibrator	3C138	3C138	3C138	3C138

Notes. IFs stands for spectral windows.

3.2 New L-band VLA observations

Most of the results presented in this thesis are based on the VLA observations. In this section, we briefly introduce the VLA radio telescope. The VLA is an interferometer located on the Plains of San Agustin, New Mexico (USA). The instrument is capable of operating between frequency range 74 MHz to 50 GHz. It consists of 27 independent antennas, each with a diameter of 25 meters. These antennas are distributed along the three arms of a track, making a wye (Y) shape. The mobile antennas can be moved into four different configurations, namely A, B, C, and D. The A configuration is the most spread out (36.4 km) and has the longest baselines. The spacing of the antennas on average decrease from the A configuration to the D configuration. For B, C, and D configurations, the maximum antenna separations are 11.1 km, 3.4 km, and 1.0 km, respectively. The A configuration, therefore, has the highest overall resolution.

The new radio observations of the cluster 1RXS J0603.3+4214 were made with the VLA in L-band, covering the wide frequency range $1-2$ GHz (project code: SE0737, PI R. J. van Weeren). The data were taken in A, B, C, and D configurations. The VLA data correspond to a total integration time of around 26 hours on the target field and about 4 hours on the calibrators. The L-band data covers 16 spectral windows. Each of these 16 spectral windows were divided into 64 channels. Each of the VLA antennas has two feeds, namely one for righted-handed polarization (R) and one for left-handed (L) polarization. All four correlation products, namely RR, RL, LR, and LL, were recorded. The L-band observations are summarized in Table 3.1.

For all four configurations, the calibrator 3C147 was observed at the beginning of the target observations. This is used as a amplitude calibrator as well as for the bandpass and phase correction. 3C137 is also known to have a negligible polarization in this frequency regime and therefore, used to calibrate the polarization leakage from the instrument. At the end of the target observations, the calibrator 3C138 was observed. At 1.5 GHz, the 3C138 is polarized up to 10% and was used for the polarization angle calibration.

3.2.1   Data reduction: calibration

The $1-2$ GHz wideband VLA data were calibrated and reduced using the Common Astronomy Software Applications (`CASA`[1]) package (McMullin et al., 2007), version 4.6.0. The data obtained from four different configurations were calibrated separately but in a same manner.

The first step of data reduction consisted of the Hanning smoothing. After this, the data were corrected for elevation dependent gain and antenna-position offset. The data were then inspected for RFI removal. The `CASA` `tfcrop` mode was used for automatic flagging of strong narrow-band RFI. We then corrected for the initial bandpass using the calibrator 3C147. This prevents flagging of good data due to the bandpass roll-off at the edges of the spectral windows. The low amplitude RFI were flagged using `AOFlagger` (Offringa et al., 2010). The amount of data affected by RFI was a few percent in A and B configurations ($\sim 5\%$) but significant interference was encountered in C and D configurations ($\sim 30\%$).

We used the L-band 3C147 model provided by `CASA` software package and set the flux density scale according to Perley and Butler (2013). As a next step, we performed an initial phase calibration using both the calibrators for a few neighboring channels

---

[1] http://casa.nrao.edu/

(channel 25−35) per spectral window, where the phase variations per channel were small. We then corrected for the parallel-hands (RR and LL) antenna delays and determined the bandpass response using the calibrator 3C147. After applying the bandpass and delay solutions, we proceeded to the gain calibration. For polarization, the leakage between the right-handed circularly polarized (R) feed and the left -hand circularly polarized (L) is essential. The leakage response was determined using the unpolarized calibrator 3C147. As a next step, we determined the cross-hand delays (RL and LR) using 3C138. Finally, the absolute position angle on the sky (the R-L phase difference) was corrected using the polarized source 3C138. In the end, all relevant calibration solutions were transferred to the target data. The resulting calibrated data were averaged by a factor of 4 in frequency per spectral windows and in time intervals of $10\,s$, $10\,s$, $6\,s$, and $4\,s$ in time for D, C, B, and A configurations, respectively. The averaging was done to permit the RM-Synthesis analysis (discussed in Chapter 7). In order to cover the largest range of spatial scales and to maximize signal-to-noise, all four configurations datasets were combined for imaging in the end.

3.2.2   Self-calibration and imaging

After calibrating each configuration, we created a initial images of the target field. The imaging of the data was executed with the `CASA` task `CLEAN`. For wide-field imaging, we employed W-projection algorithm (Cornwell et al., 2008) which takes into consideration the effect of non-coplanarity. To take into account the spectral behavior of the bright sources in the field, we imaged each configuration using `nterms` $= 3$ (Rau and Cornwell, 2011). The deconvolution was always performed using a multi-scale multi frequency `CLEAN` algorithm (Rau and Cornwell, 2011) and with `CLEAN` masks generated by the `PyBDSF` (Mohan and Rafferty, 2015). The multi-scale setting assumes that the emission can be modeled as a collection of components at a variety of spatial scales, hence, this setting is necessary to account for the extended emission. We used the `Briggs` weighting scheme with a `robust` parameter of 0.

Following initial imaging, we performed self-calibration with a few rounds of phase-only calibration and checked that the model, to be included for self-calibration, does not have artifacts or negative components. We then ran a final round of amplitude-phase calibration. For A and B configurations, we performed an additional bandpass calibration on the target, using the target field model derived from the self-calibration. The A and B configurations imaging require a high dynamic range which in turn require a precise bandpass. We found that this additional step reduced artifacts around
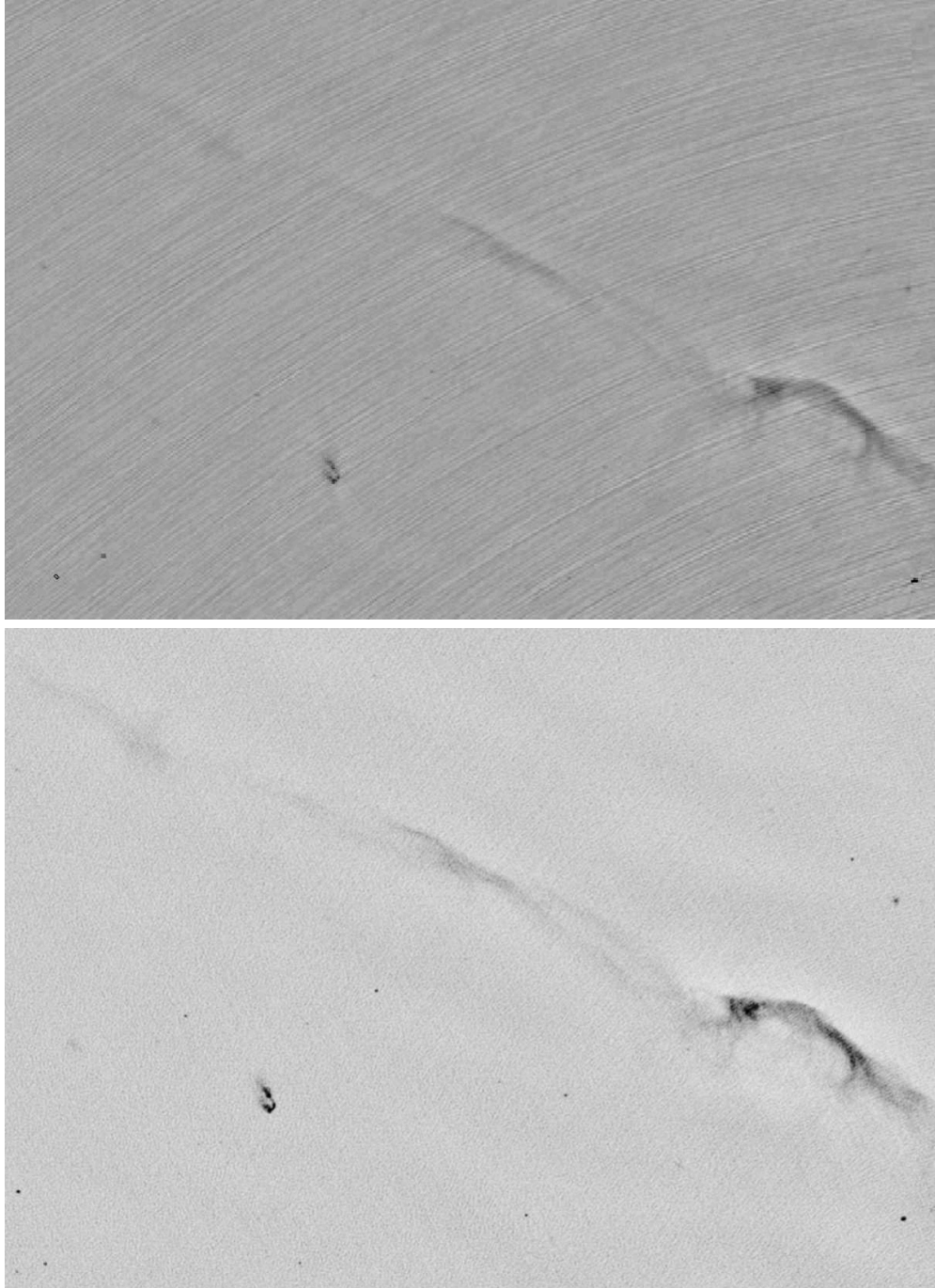
Figure 3.4: VLA $1-2$ GHz A configuration images of the Toothbrush showing artifacts. *Top*: Image after few rounds of self-calibration. The image clearly shows high dynamic range issues because of the bright source A, sitting close to the relic. *Bottom*: Image obtained after advanced calibration and the dynamic range is 330 000.

source A, located close to the Toothbrush and the halo, see Figure 3.4. For C and D configurations, we skipped this step because no artifacts were visible.

After selfcalibration and deconvolution of each configuration independently, we subtracted three bright sources from the uv-data, which reduced the high dynamic range. Next, for each configuration, we made a single deep Stokes I continuum image using the full bandwidth but with `nterms` = 2. In general, the noise level of the image increases with higher `nterms`. The imaging of each configuration with `nterms` = 2 reduced the noise level by about 30%-40%. The imaging of a large field is very time consuming, therefore, to speed up the process, we created a region to the center of the cluster and subtracted in the uv-plane all sources outside that region.

Finally, we combined the data from A, B, C, and D configurations to make a single deep full bandwidth Stokes I image, using multi-scale clean and `nterms` = 2. After combining the data set from all configuration, we did not perform any further selfcalibration. To correct for the attenuation of the primary beam pattern of each of the antennas of the VLA, it is necessary to apply a primary beam correction to the images. The `CASA` task `widebandpbcor` was used for this purpose. All the VLA radio images shown through-out this thesis have been corrected for the primary beam.

We would like to emphasize here that the final radio continuum images were made after combining the data from all four configurations, covering a wide frequency range of $1-2\,$GHz. The handling of wideband data is difficult. Moreover, the bright sources need a high dynamic range and, therefore, calibration is challenging and should be done carefully. The imaging of such a large field is very time consuming.

Chapter 4

A spectacular view of the Toothbrush

In this chapter, we present the resultant VLA L-band radio continuum images of the cluster 1RXS J0603.3+4214. To compare the VLA total intensity features with other frequencies, we also use the GMRT (610 MHz) and LOFAR (150 MHz) observations. The GMRT and LOFAR data were originally published by van Weeren et al. (2012a) and van Weeren et al. (2016), respectively. We re-image the LOFAR and the GMRT data. The data reduction steps of the GMRT and LOFAR observations are explained in van Weeren et al. (2012a); van Weeren et al. (2016).

4.1 VLA 1-2 GHz total intensity images

The VLA $1-2$ GHz radio continuum images of 1RXS J0603.3+4214 at different resolutions are shown in Figure 4.1. These images were created using uv-taper option within the `CLEAN` algorithm in which uv-data are multiplied with a Gaussian function, as a result lowering the image resolution. In Figure 4.1 panel (c), the sources are labeled following van Weeren et al. (2012a) and extending the list. The known diffuse emission sources, namely the bright Toothbrush, the two fainter relics (sources E and D), and the large elongated halo (C), are evidently recovered in our observation.

4.2 The Toothbrush relic

In this section, we discuss the total intensity features visible in our $1-2$ GHz VLA images. The VLA high-resolution image of the spectacular toothbrush-shaped relic, labeled as B1, B2, and B3 in Figure 4.1, is shown in Figure 4.2. The new image clearly shows the complex, often filamentary structures across the entire Toothbrush, in particular in B1 region. These filamentary structures were not obvious before.

The most prominent features are labelled in Figure 4.3. We briefly describe some of the structures. The bright part of the Toothbrush, i.e., the 'brush' B1, shows a distinct narrow ridge to the north with a clear sharp outer edge. The high resolution image shows how rich in structure the radio emission is. For instance, at a resolution of $5''$,
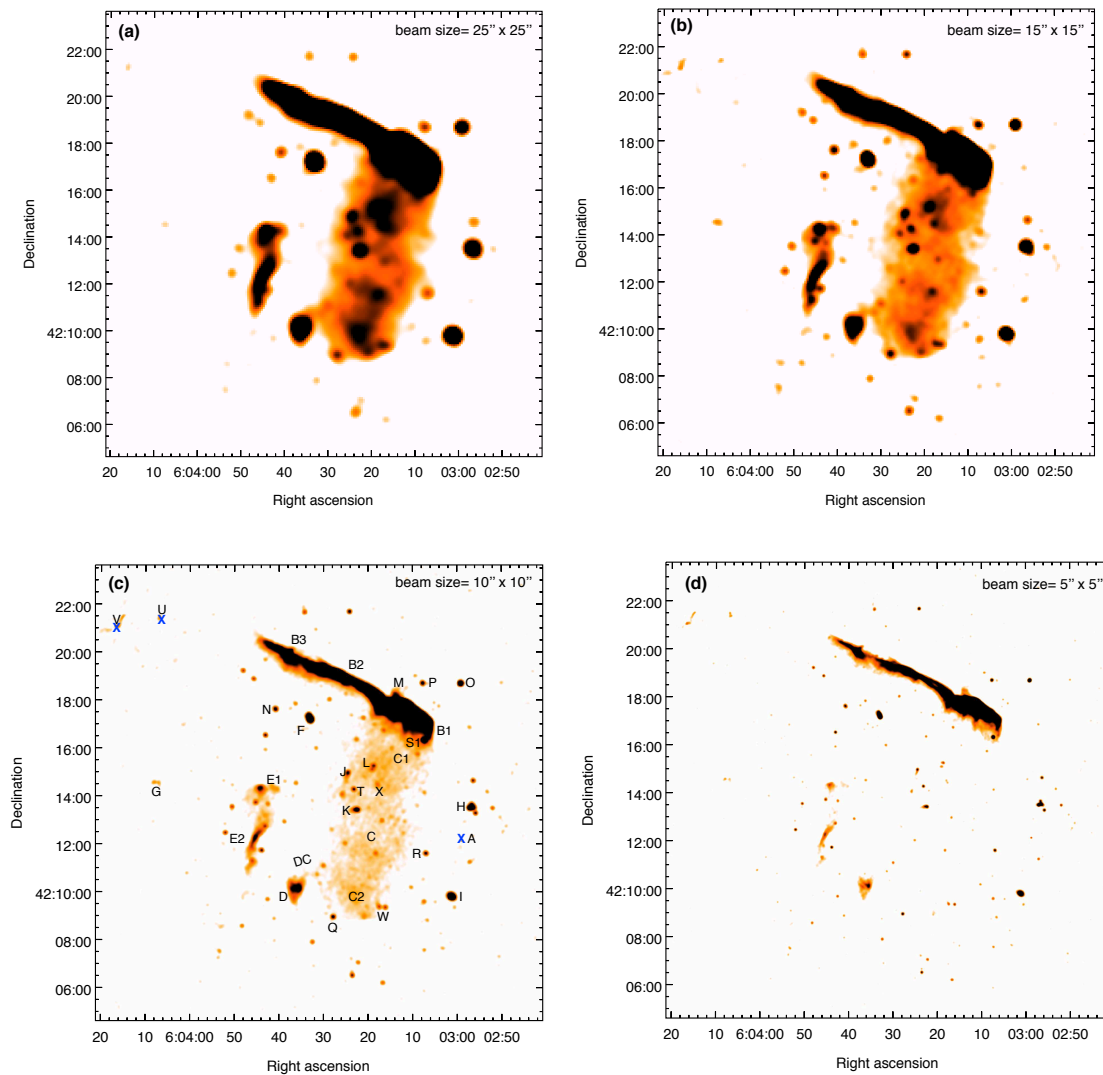
Figure 4.1: VLA $1-2$ GHz images of 1RXS J0603.3+4214 at different resolutions. These images were made by combining A, B, C, and D configurations data and using robust weighting. *Top*: panel (a) at a resolution of $25''$ and a noise level of $24\,\mu$Jy beam^{-1}, panel (b) at a resolution of $15''$ a noise level of $16\,\mu$Jy beam^{-1} *Bottom*: panel (c) at a resolution of $10''$ and a noise level of $11\,\mu$Jy beam^{-1}, panel (d) at a resolution of $5''$ and a noise level of $6\,\mu$Jy beam^{-1}. The blue cross marks the location of the sources which have been subtracted, namely A, U, and V.
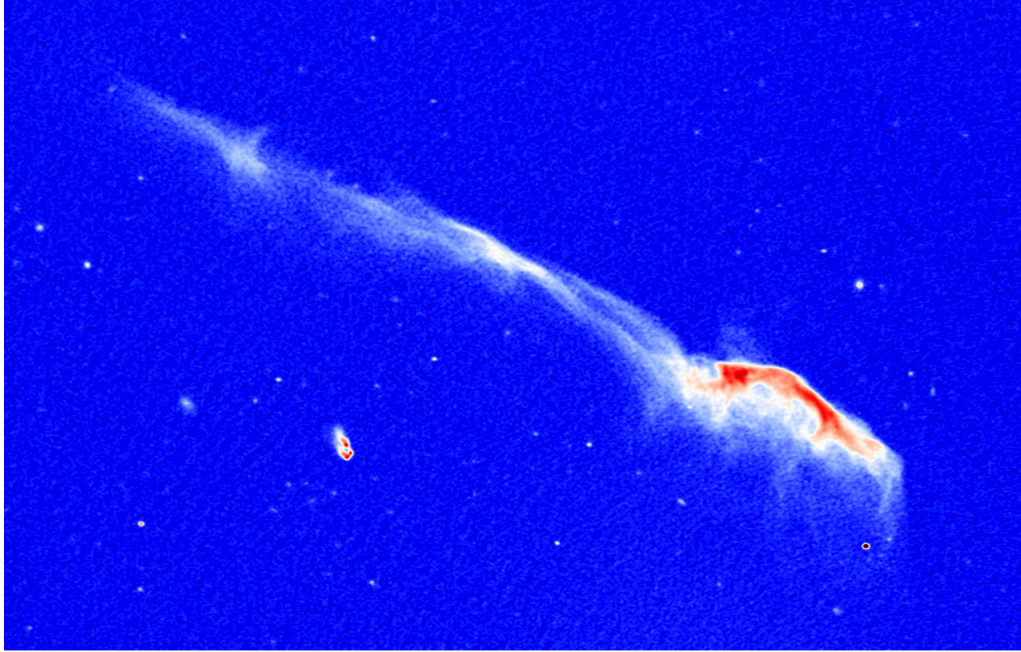
Figure 4.2: High resolution VLA $1-2$ GHz image of the Toothbrush showing the complex, often filamentary structures. The image has been made using all data (ABCD configurations) and with robust=0 weighting. The beam size is $1''.96 \times 1''.50$ and a noise level is 6μJy beam^{-1}.

the ridge appears smooth but at a high resolution many detailed structures can be identified. We find that at the narrowest region, the ridge has a width of about 25 kpc.
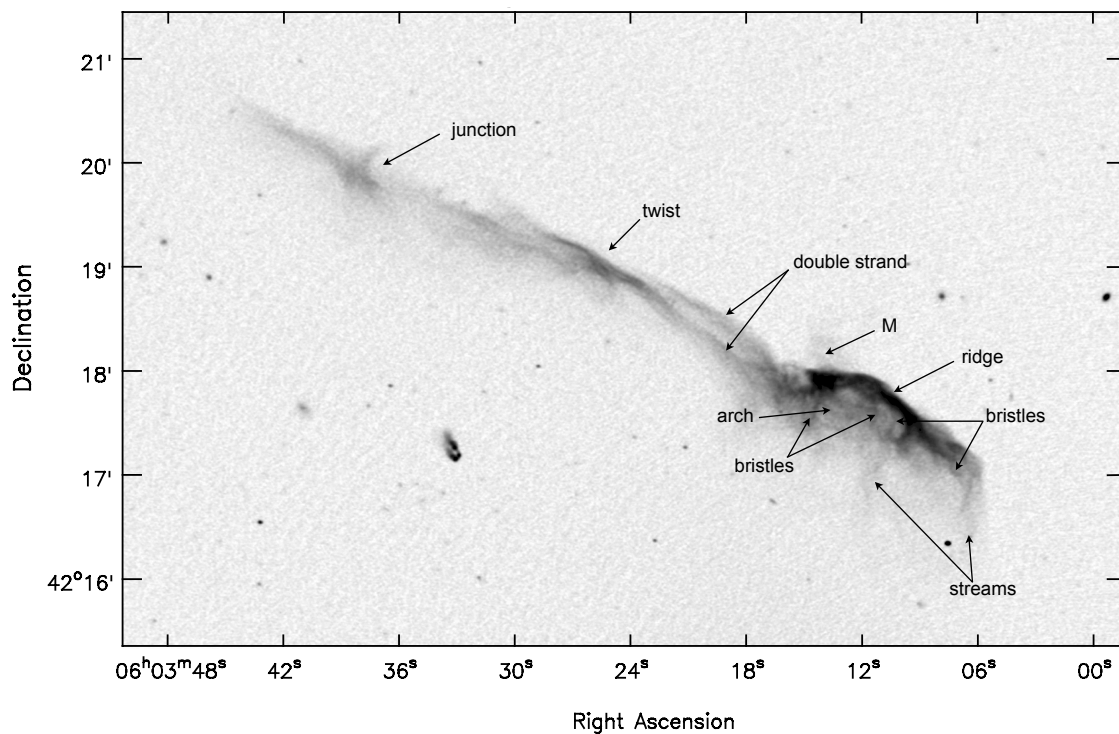
Figure 4.3: VLA $1-2$ GHz radio image of the Toothbrush with labeling of prominent features. The beam size and noise level are the same as in Figure 4.2.

To resolve and identify structures across the brush, in particular the ridge, we created another image using only the A and B configurations data. The resultant image has a restoring beam of $1''.07 \times 0''.97$. This high resolution image reveals that the ridge consist of two parts which branch to the west, labeled as ridge branches, see Figure 4.4. The ridge branching clearly indicates that the shock surface is not uniform.
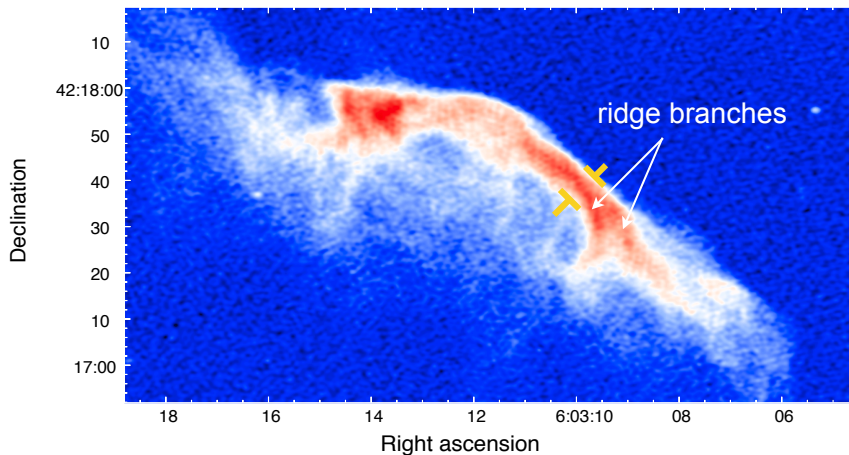
Figure 4.4: High resolution VLA $1-2$ GHz images of brush region, showing that the ridge consists of two parts which branch to the west. The image has been made using A and B configuration data. The beam size is $1''.07 \times 0''.97$ and a noise level is $6 \, \mu$Jy beam^{-1}. The ridge has a width of about 25 kpc, measured across the region marked with yellow.

The brush shows small arc-shaped filaments, 'bristles', that are more or less perpendicular to the ridge, as shown in Figure 4.3. The width of the bristles is about 3 to 5 kpc. Moreover, at the eastern side of the brush and downstream of the ridge, three arch-shaped filaments are visible, labelled as 'arch'. However, the shape and the width of these arch-shaped filaments are different than that of the bristles. To the northeast of the ridge (i.e., in upstream of the ridge), we confirm the low surface brightness emission, labelled as source M, reported by van Weeren et al. (2012a).

The origin of the filamentary structures, the ridge, the bristles, and the arches is not known. For the relic in Abell 2256, very long, distinct filaments stretching across the entire relic have been found (Owen et al., 2014). The origin of the filaments in Abell 2256 is also not known. They could for instance reflect magnetic field tubes, intersections of magnetic field sheets (like a 'puffy pastry') with the shock front, or variations in the electron acceleration efficiency. Owen et al. (2014) speculated that the radio emission in Abell 2256 originates from a current sheet located at the boundary of two magnetic domains. It is important to mention here that the relic in Abell 2256 is seen face-on while the Toothbrush is rather seen edge-on. Possibly the brush has similar filaments as the relic in Abell 2256 but due to the edge-on view we only see the ends of the filaments, the 'bristles'.

The surface brightness downstream of the ridge drops very quickly (i.e., by about 50%) at $1-2$ GHz while at low frequencies, namely at 150 MHz and 610 MHz, it decreases rather gradually, see Figure 4.5.
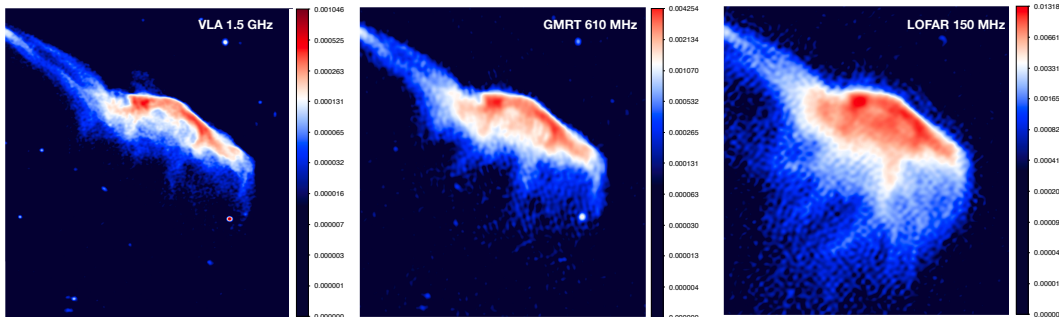
Figure 4.5: Brush region of the Toothbrush at three different frequencies, namely at 150 MHz, 610 MHz and 1.5 GHz. The image clearly shows that the surface brightness downstream to the ridge decreases quickly at 1.5 GHz and the brush region appears wider at low frequencies. Color bar indicates the surface brightness in units of Jy beam^{-1}.

At 610 MHz and 150 MHz, van Weeren et al. (2012a); van Weeren et al. (2016) found several 'streams' of emission, extending from the northern part of the brush to the south. These streams are also visible in the VLA $1-2$ GHz image, see Figure 4.3 and Figure 4.5. The width of these streams changes when moving from north to south from 60 kpc to 30 kpc, respectively. However, these streams are wider than the bristles which suggest that bristles are possibly magnetic filaments while the streams are possibly the variation in the shock front.
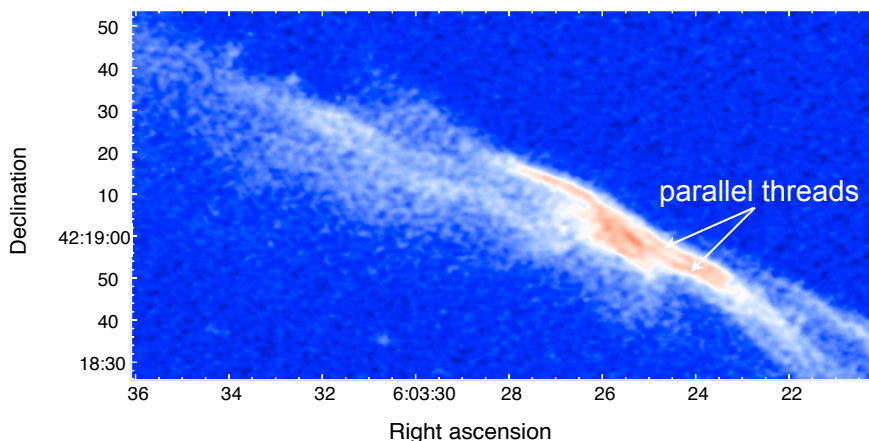
Figure 4.6: Cut-out around the center of the B2 region (twist), revealing two very thin parallel filaments that are separated by 5 kpc. The image has been made using all data (ABCD configuration) and with robust=0 weighting. The beam size is $1''96 \times 1''50$ and the noise level is 6 μJy beam^{-1}.

Another distinctive morphological feature visible in our VLA image is the double strand. The double strand emerges from the brush region and linearly extends to the east, forming the handle of the Toothbrush, see Figure 4.3. The intrinsic width

of these strands varies from 30 kpc to 17 kpc when looking from west to east. The separation of the two strands is about 7″ corresponding to a physical size of 25 kpc. It seems that the strands overlap at $06^h03^m25^s$ $+42°18″59$. It could be also a projection effect. To the east of the double strand there seems to be several strands again and they appears twisted (Figure 4.3).

The highest resolution VLA image also reveals that in the twist region, one of the strands actually consists of two thin parallel "threads" with a separation of about 1″3 corresponding to 5 kpc, as shown in Figure 4.6.
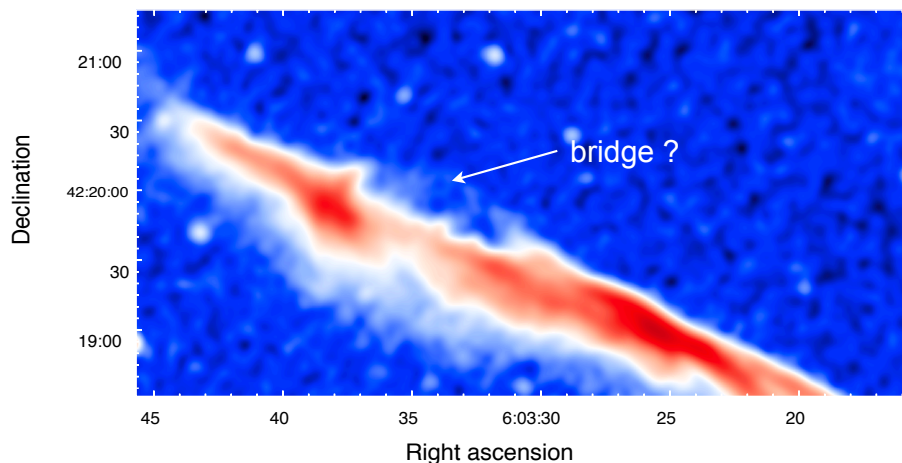
Figure 4.7: Bridge connecting the B3 region of relic to B2. The image has been made using all data (ABCD configuration) and with robust=0 weighting. The beam size is $5″00 \times 5″00$ and a noise level is $8\,\mu$Jy beam^{-1}.

The B3 part of the Toothbrush consist of an arc-shaped filament extending from north to south. The highest surface brightness within the B3 region is found at this arc-shaped filament. We denote this region as the 'junction' (Figure 4.3). In our VLA $1-2$ GHz images, we find low surface brightness emission which connects the northern tip of the junction to the one end of the strands of the B2 region, labelled as 'bridge', see Figure 4.7. The handle of the Toothbrush, i.e., components B2 and B3, is enigmatic because of its large and straight extent, and its asymmetric position with respect to the cluster merger axis.

The complexity of all the identified structures in the Toothbrush at least rule out that radio relics are made of a smooth shock surface. The filamentary structures imply that the shock morphology and magnetic fields are likely the main ingredients to form such structures.

4.3 Fainter relics E and D

The cluster 1RXS J0603.3+4214 is also known to hosts two smaller and fainter relics. The radio relic E is located on the eastern side of the cluster center as shown in Figure 4.1 panel (c). It shows two bright regions, i.e., E1 and E2. The total extent of E, from north to south, is about 5$.'$2 corresponding to a physical size of 1.1 Mpc.
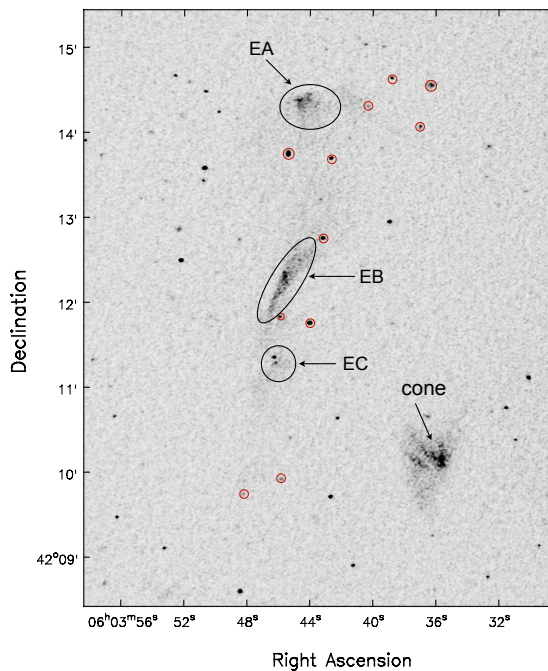
Figure 4.8: High resolution VLA 1−2 GHz image of relics E and D ("cone"). The image has been made using all data (ABCD configuration) and with robust=0 weighting. The beam size is 1$''$96 × 1$''$50 and a noise level is 6 μJy beam^{-1}. The three bright compact regions EA, EB and EC are surrounded by diffuse low surface brightness emission. The compact sources embedded within relic E, that are clearly identified at 1.5 GHz with optical counterparts visible in the Subaru image, are marked with red circles.

The high resolution VLA image of relic E is shown in Figure 4.8. We find that three bright regions of relic E, labeled as EA, EB, and EC, are surrounded by low surface brightness emission. For none of these three regions, we identifed a related radio galaxy. However, there are several radio galaxies embedded within relic E, marked with the red circles in Figure 4.8, with optical counterparts but they don't appear to be associated with these three regions. This underlines that all three regions are diffuse emission.

Relic D is located at the south-west of relic E. The morphology of relic D (Figure 4.8) is similar as found by van Weeren et al. (2012a) using the GMRT 610 MHz data. Part of the emission resembles a Mach cone of a bullet, see Figure 4.8. Like for relic E, we do not found a related radio galaxy for relic D.

Relics E and D show a quite unusual morphology; however, we do not find any connection to a nearby radio galaxy. Given the relatively small size and peculiar morphology of relic D, we speculate it could trace revised fossil radio plasma, possibly re- accelerated by a merger induced shock. A similar scenario could also hold for relic E.

4.4   Optical, X-ray and radio continuum overlay

The cluster 1RXS J0603.3+4214 was observed with the 8.2 m Subaru telescope on 25 February 2013 in r, g, and i colors for 2880 s, 720 s, and 720 s, respectively (Jee et al., 2016). The spectroscopic redshifts were derived from Subaru optical observations (Dawson et al. in preparation). In X-ray, the cluster was observed in 2013 with the Chandra X-ray telescope for 273 ks using the ACIS-I camera (van Weeren et al., 2016).

We created an overlay of the optical, X-ray, and radio emission of the cluster region, see Figure 4.9. The brush part of the Toothbrush is located in the ICM while the handle extends in a region where the ICM is not so dense.

For relic E, point sources for which we found an optical counterpart are denoted with red circles in Figure 4.8. As evident the brightest regions of relic E, i.e., EA, EB, and EC do not show any optical counterparts. For relic D also, we do not find any optical counterparts, which could be assumed to be the source of the radio emission.

4.5   Radio galaxies in the field

In our new VLA images, we detect several head-tail radio galaxies located in the cluster or its vicinity. The redshift of these sources were provided by William Dawson. The properties of radio galaxies in the cluster are summarized in Tables 4.1. Head-tail radio galaxies are expected for a cluster undergoing a merger, traveling with high velocities through the ICM. Some of the interesting radio sources are shown in Figure 4.10 (radio-optical overlays).

Source F is a double-lobe radio source with bent lobes and belongs to the cluster. It has a total extent of 76 kpc and consists of a central core and two extended radio lobes. Both lobes extend towards the northwest direction.

Sources I and N are foreground spiral galaxies. Sources J and K are evidently head-tail radio sources and are cluster members. The total extents of J and K are around 70 kpc. Sources L, W, and X have been resolved in higher resolution images and actually consist of two different sources.
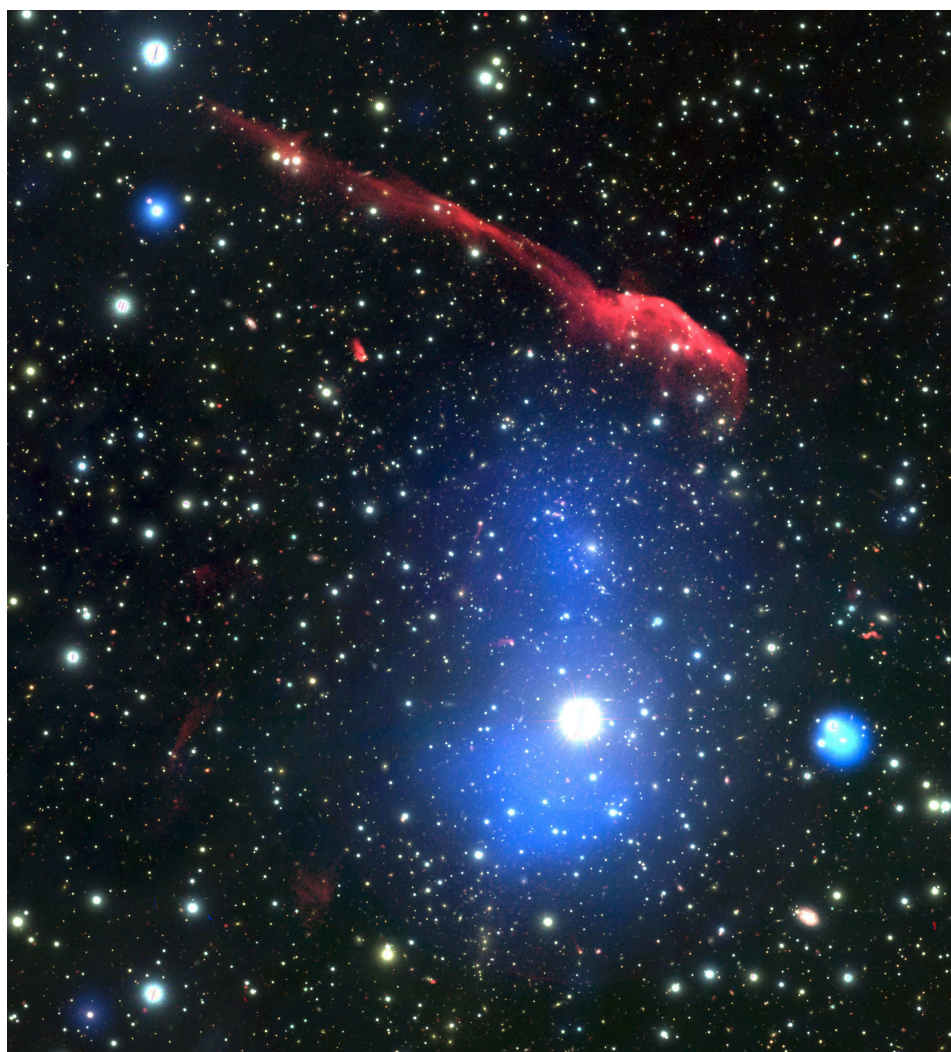
Figure 4.9: Radio, X-ray and optical overlay of cluster 1RXS J0603.3+4214. Red shows the radio emission observed with VLA at a central frequency of 1.5 GHz. The VLA image has a resolution of 3″. Blue shows the Chandra X -ray emission in the 0.5 - 2.0 keV band and in the background is the color composite optical image created using Subaru data with g, r, and i intensities represented in blue, green, and red, respectively.
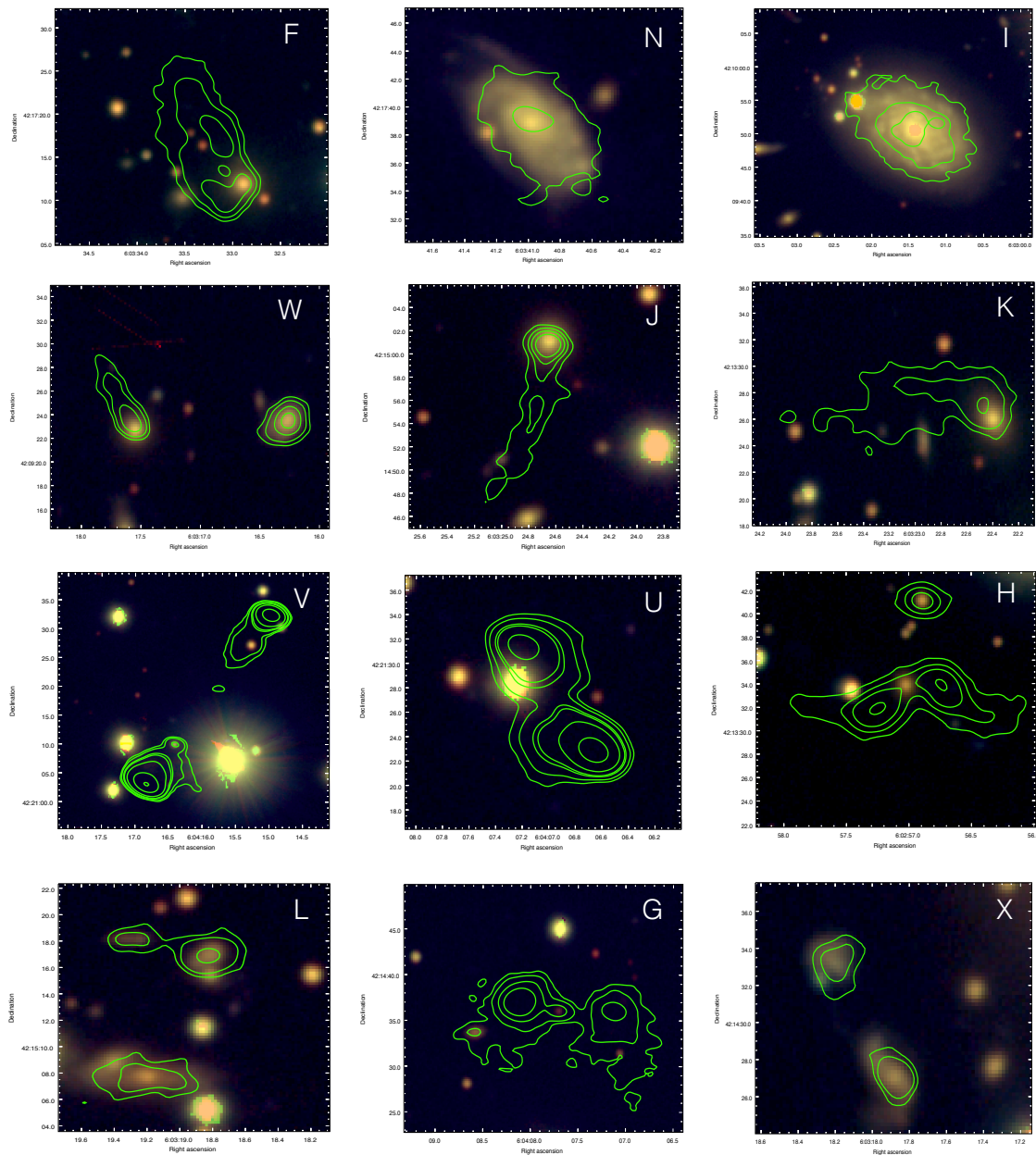
Figure 4.10: Radio-optical overlay of some of the radio sources located in the cluster. The image has been made using all data (ABCD configuration). The beam size is $1''.96 \times 1''.50$ and the noise level is $6\,\mu\mathrm{Jy\ beam}^{-1}$. The green contours are from the VLA image and are drawn at levels of $[1, 2, 4, \ldots] \times 4.5\,\sigma_{\mathrm{rms}}$. The optical image is the same as in Figure 4.9.

Table 4.1: Flux density of compact sources in the cluster region

Source	$S_{1.5\,\mathrm{GHz}}$ mJy	type
A	286.0 ± 28.0	quasar
F	5.78 ± 0.27	double-lobed
G	4.44 ± 0.32	double lobed
H	2.52 ± 0.23	double-lobed
I	4.27 ± 0.53	spiral-galaxy
J	0.58 ± 0.17	head-tail
K	0.95 ± 0.21	head-tail
L	0.62 ± 0.22	
N	0.65 ± 0.12	spiral-galaxy
O	1.72 ± 0.20	spiral-galaxy
P	0.58 ± 0.13	
Q	0.43 ± 0.09	
R	0.38 ± 0.08	
S1	1.46 ± 0.09	
T	0.33 ± 0.07	
U	24.80 ± 2.10	double-lobed
V	65.60 ± 6.01	double-lobed
W	0.30 ± 0.07	head-tail
X	0.25 ± 0.06	

Sources H, G , V, and U are double-lobed radio galaxies, see Figure 4.10. Source H displays symmetric radio lobes whose radio emission extends further at both of the lobes. The radio source V is asymmetric with sharp-edged lobes and bright hot spots. At $1''$ resolution, the northwest lobe appears to be larger and brighter than the southeast one. In the optical image, two compact sources are visible, and the compact core might overlaps with the southern lobe due to projection. Given the asymmetry of the two lobes, this source could indeed be the core. The radio lobes of source G are extended and the core is visible at high resolution. The radio emission at the east and the west lobe is diffuse and further extends to the south. The extent of the lobes to the south may indicate that the source moves relative to some low-density intracluster or intergalactic medium. The source U has symmetric lobes but without any core.

The deep VLA image has allowed us to identify many compact sources in the field of view, many of them are radio galaxies that belongs to the cluster.

4.6   Flux measurements

Accurately measuring the flux density of extended low surface brightness sources in sky brightness distributions obtained with interferometers is challenging for several

reasons: (1) missing short uv-distances, i.e., inner uv-cut (where u and v are coordinate system for the baselines of an interferometer). The small uv-distance (short baselines) measures the extended emission while long uv-distance (long baselines) measures the small scale emission, i.e., compact source. Therefore, if short baselines are missing the flux of the extended structures gets 'resolved out'; (2) uv-coverage or the distribution of antennas. The dense inner uv-coverage is important to recover the extended emission; (3) the deconvolution of faint emission. The structures with a surface brightness close to the noise level are difficult to deconvolve and the resulting flux measurements are very uncertain, for instance in the high resolution image the radio halo is not visible (Figure 4.1 panel d). The deconvolution of such a low brightness emission is challenging, in particular at high resolution.

In this section, we investigate how the measured flux density varies when using different imaging parameters, namely inner uv-cut and the resolution. The flux densities reported in this section, unless stated otherwise, are measured from radio maps imaged with uniform weighting.
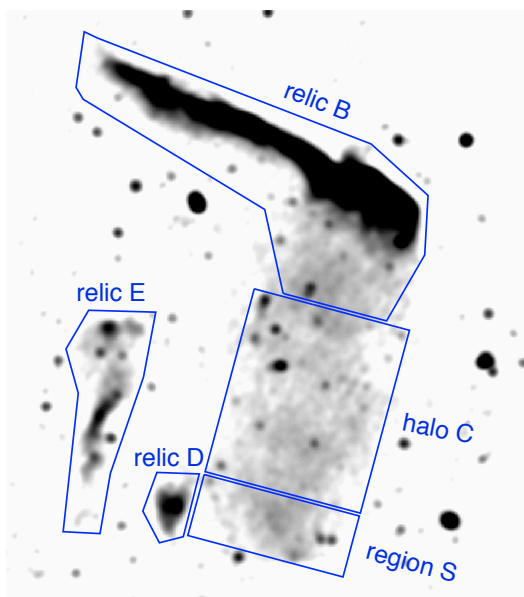
Figure 4.11: VLA 11″ resolution image depicting the regions where the integrated flux densities were measured.

Different resolution: In order to find how much flux is lost when changing the resolution, we create radio maps at different resolutions. The flux density of a radio source depends on the ratio between the largest angular scale sampled by the interferometer and the angular size of the source. In Table 4.2, we report the flux values of several regions. The regions where the flux densities were extracted are shown in Figure 4.11. As expected, the VLA low resolution image made with all configurations and without any uv-cut gives the maximum flux. For instance, the flux density of the Toothbrush measured from the 25″ resolution map is $310 \pm 21 \, \text{mJy}$. The flux density of the same

region when measured from the 25″ LOFAR and GMRT images is 4428 ± 410 mJy and 767 ± 82 mJy, respectively. We then created images at higher resolution, namely 5″.5. The measured flux densities from the 5″.5 radio maps at 1.5 GHz, 610 MHz, and 150 MHz are 296 ± 17 mJy, 751 ± 78 mJy and 3669 ± 378 mJy, respectively. This implies that the increase in the image resolution results in a 5 % flux loss at all three frequencies. This imply that in high resolution images low surface brightness emission is 'hidden' in the noise and not deconvolved.

With or without an uv-cut: The VLA, LOFAR, and GMRT images without any uv-cut give the maximum flux values. For instance, the flux density measured from the VLA 5″.5 map is 296 ± 17 mJy. However, images made at the same resolution but using a common inner uv-cut of 0.9 kλ (here, kλ is the unit of uv-distance where k stands for kilo and λ is the wavelength) give a flux density of 258 ± 14 mJy. We notice the same flux density reduction for the LOFAR and GMRT data, e.g., without any uv-cut the flux density of the Toothbrush at 150 MHz is 4428 ± 410 mJy and with a uv-cut it is 3669 ± 378 mJy. Hence the uv-cut causes a flux loss of about 15 %.
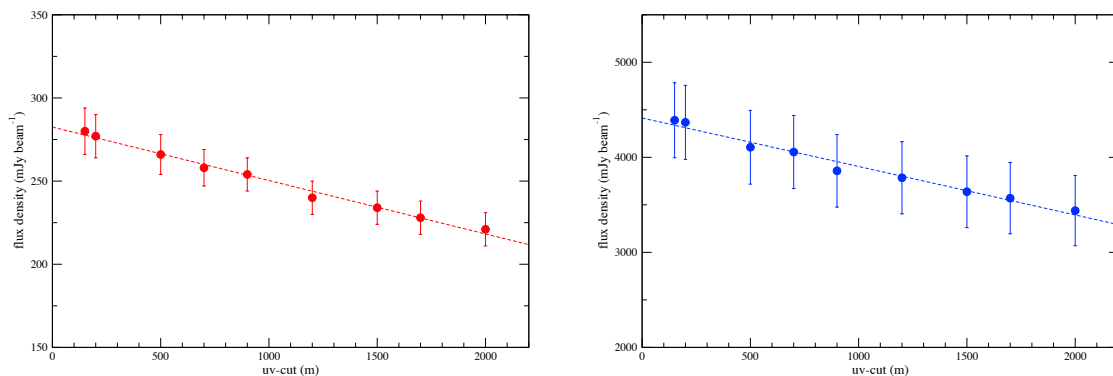
Figure 4.12: *Left*: Dependence of the 1.4 GHz integrated flux density of the Toothbrush on the uv-cut employed. *Right*: Same as the left panel but for the 150 MHz integrated flux density. The dashed line is a linear fit.

Different uv-cuts: A simple plot between the measured flux density and the minimum uv-distance will give us the rough estimate how much flux is lost when we use different inner uv-cut. For the Sausage relic, Stroe et al. (2013) used the 150 MHz GMRT data to find the dependence of the flux density on the inner uv-cut employed. They obtained the total power from 150 MHz to 8.3 GHz by fitting the points with a uv-cut smaller than 300λ (see Figure 5 of Stroe et al., 2013). They also produced a mock radio observation of the Sausage-relic and found that the resultant simulated radio flux agrees to the one obtained from interferometric data. We performed a similar exercise with the VLA 1−2 GHz and LOFAR 150 MHz data. We would like to emphasize that both the VLA (A, B, C, and D configurations) and the LOFAR observations have a dense inner uv-coverage. Figure 4.12 shows the resultant plot of the integrated flux

Table 4.2: Flux densities and integrated spectra of the diffuse radio sources in the cluster 1RXS J0603.3+4214

Source	VLA			GMRT	LOFAR		LLS	α_{150}^{1500}	$\mathcal{M}$
	25″	5.″5 and 11″	5.″5 and 11″ with uv-cut	5.″5 with uv-cut	25″	5.″5 and 11″ with uv-cut			
	$S_{1.5\,\mathrm{GHz}}$ mJy	$S_{1.5\,\mathrm{GHz}}$ mJy	$S_{1.5\,\mathrm{GHz}}$ mJy	$S_{610\,\mathrm{MHz}}$ mJy	$S_{150\,\mathrm{MHz}}$ mJy	$S_{150\,\mathrm{MHz}}$ mJy	Mpc		
(1)	(2)	(3)	(4)	(5)	(6)	(7)	(8)	(9)	(10)
relic B	310.0 ± 21	296.0 ± 17.0	258.0 ± 14.0	751.0 ± 78.0	4428.0 ± 410.0	3669.0 ± 378.0	1.9	-1.15 ± 0.02	$3.78^{+0.3}_{-0.2}$
halo C	33.4 ± 2.7	31.6 ± 2.6	30.0 ± 1.2	—	490.0 ± 56.0	441.0 ± 44.0	1.7[†]	-1.17 ± 0.04	—
relic D	5.2 ± 0.8	4.9 ± 0.7	4.6 ± 0.2	13.0 ± 1.7	98.1 ± 11.8	87.1 ± 9.1	0.3	-1.28 ± 0.05	—
relic E	11.6 ± 1.3	10.1 ± 1.2	9.0 ± 0.3	18.7 ± 2.2	153.1 ± 13.0	115.2 ± 11.8	1.1	-1.11 ± 0.05	$4.3^{+1.4}_{-0.7}$
region S	9.1 ± 1.1	8.4 ± 1.0	7.7 ± 0.3	—	172.0 ± 18.8	148.0 ± 15.0	0.7	-1.28 ± 0.05	—

Notes. The regions where the fluxes were extracted are indicated in Figure 4.11; [†] size of the entire halo, i.e., C=C1+C2.

densities of the Toothbrush, measured from the VLA and the LOFAR image, versus the minimum inner uv-cut. We note that the flux density drops by a factor of 27 % at 1.5 GHz when using baselines beyond 2000 meters. The same drop in the flux is also found for the 150 MHz LOFAR data. Moreover, for both data sets the measured flux density decreases linearly with the uv-cut. It is evident from Figure 4.12 that the uv-cut causes a 15 % flux loss. Our flux density measurements of the Toothbrush are thus, different than the one predicted by Stroe et al. (2013).

The image resolution and the uv-cut, thus, lower the true flux density to at least 20 %. Therefore, to ensure that we recover flux on the same spatial scales, we always create images with a common inner uv-cut of $0.9 \, k\lambda$. The $0.9 \, k\lambda$ is used to match the scale of the GMRT with the VLA and LOFAR. Here, $0.9 \, k\lambda$ is the minimum well sampled uv-distance in the GMRT data. We prefer to measure the flux density from the higher resolution images where it is easier to separate the real source emission from other complex sources. Although we lose some flux (less than 5 %) when measuring the flux density from higher resolution images but this effect remains the same for all data sets. However, this does not affect the integrated spectral index calculations significantly.

4.6.1   Integrated radio spectra

To obtain the integrated spectra of relics, we convolved the LOFAR, GMRT, and VLA images to the same beam size, namely $5''\!.5 \times 5''\!.5$. The flux scale issue could result in an over or under estimation of the flux density, at a particular frequency. Therefore, we first checked the integrated spectrum for compact sources visible in the field to ensure that the VLA, GMRT, and LOFAR observations are on the same flux scale. The integrated spectra for some of bright sources that are clearly detected at three frequencies is shown in Figure 4.13 left panel. As visible from the spectrum almost all sources can be more or less fitted by a single power law. We do not find any systematic break in the spectrum between 150 MHz to 1.5 GHz.

The integrated synchrotron spectra for relics B, D, and E obtained by combining our measured flux densities at frequencies 150 MHz, 610 MHz, and 1.5 GHz, are shown in Figure 4.13 right panel. The radio spectrum of the Toothbrush has been studied extensively. van Weeren et al. (2012a) reported that the integrated spectrum from 74 MHz to 4.9 GHz has a power-law shape with $\alpha_{\text{int}} = -1.10 \pm 0.02$. Later on Stroe et al. (2016) studied the integrated spectrum of the Toothbrush from 150 MHz to 30 GHz and detected a spectral break above about 2 GHz. They reported that the spectral index steepens above 2 GHz from $\alpha = -1.00$ to $\alpha = -1.45$. Recent high frequency observations at 4.85 GHz and 8.35 GHz with the 100m-Effelsberg telescope indicates
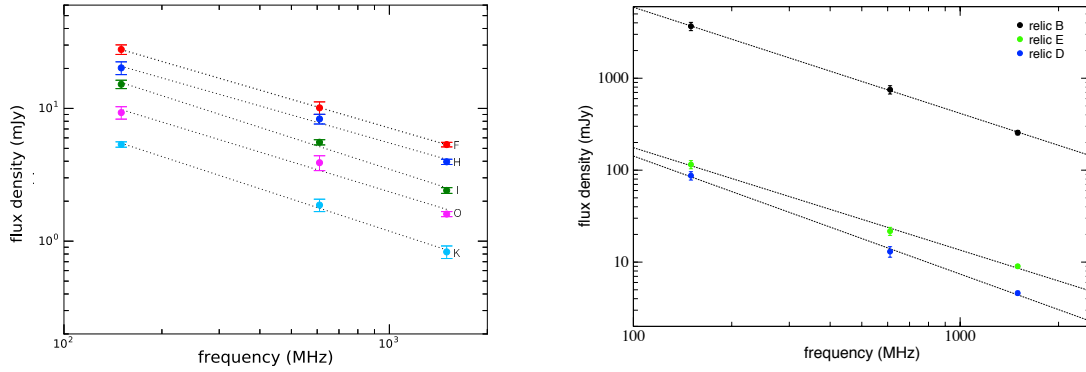
Figure 4.13: *Left*: Integrated radio spectra of the radio galaxies with clear detections at all frequencies, for labelling see Figure 4.1 panel (c). *Right*: Integrated spectra relics B, D and E for 150 MHz, 610 MHz and 1.5 GHz. Dashed lines are fitted power-laws with indices given in Table 4.2.

that the integrated spectrum of the Toothbrush has a power-law shape with index $\alpha = -1.0 \pm 0.04$ up to 8.35 GHz (Kierdorf et al., 2016). Hence it remains unclear if the integrated spectrum of the Toothbrush is curved at high frequencies or not.

For the Toothbrush, we obtain a spectral index of -1.15 ± 0.02 which is consistent with the previous values of -1.10 ± 0.02 (van Weeren et al., 2012a) and -1.09 ± 0.05 (van Weeren et al., 2016). The spectrum is fitted well by a single power law. We do not find any evidence for a spectral steepening in the frequency range 150-1500 MHz. From the integrated spectrum, we derive a Mach number of $\mathcal{M} = 3.78^{+0.3}_{-0.2}$ for the Toothbrush.

For the fainter relic E, we measure an integrated spectral index of -1.11 ± 0.05, suggesting a Mach number of $4.3^{+1.4}_{-0.7}$. The integrated spectral index of relic D is -1.28 ± 0.05.

4.7   Bright compact source

For the brightest compact source in the field, source A (B3 0559+422A), we measure a flux density of 286 ± 28 mJy at 1.5 GHz. The radio source has been catalogued as a quasar by Andrei et al. (2009) and its redshift information is not available in the literature.

In Figure 4.14, we show the radio spectrum of the source A between 75 MHz to 8 GHz. The radio spectrum of source A appears to have a spectral break towards low frequencies. The turnover is visible at around ~ 1.5 GHz. The physical processes that could be responsible for the low-frequency cutoff in the radio spectrum are synchrotron self-absorption or free-free absorption (O'Dea, 1998; de Kool and Begelman, 1989). The spectral shape, source variability and source size are important properties that are used to identify which processes play a role (Kellermann and Pauliny-Toth, 1968; Kellermann, 1966).
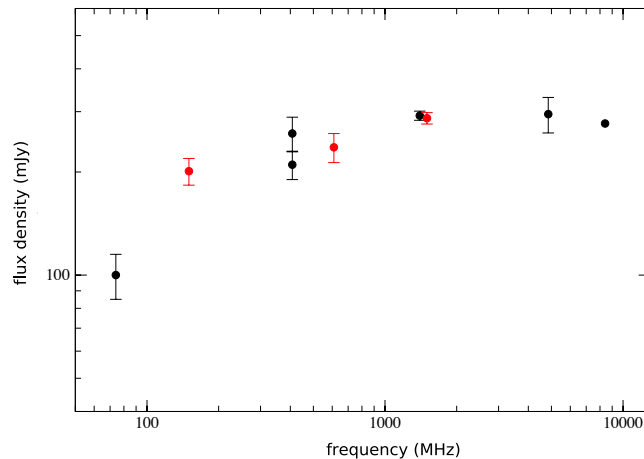
Figure 4.14: Integrated radio spectrum of source A. The flux density measured from our radio maps using the VLA, GMRT, and LOFAR are shown in red. The flux density at 75 MHz is taken from VLSS Lane et al. (2012) and the rest of the flux density measurements were taken from other sources (Ficarra et al., 1985; Gregory and Condon, 1991; Becker et al., 1991; Patnaik et al., 1992; Condon et al., 1998; Marecki et al., 1999).

A potentially variable source is clearly not a good flux calibrator, e.g., source A. Moreover, fluxes are not well measured in literature so one should be careful while using such sources as a good flux calibrator. This bright source A had to be modeled with more `nterms` to approximate the spectral shape.

4.8   Summary

We presented the $1-2$ GHz radio-continuum image of the cluster 1RXS J0603.3+4214. The new VLA observations allowed us to study the total intensity features down to one arcsec resolution with very high sensitivity. The main results are:

1. The Toothbrush is made of complex filamentary structures. The complexity of the filamentary structures identified in the Toothbrush relic rule out the fact that radio relics are caused of a smooth shock surface.

2. The bright brush has a striking narrow ridge to its north with a quite sharp outer edge. At the narrowest region, the ridge has a width of about 25 kpc. We find that the ridge branch to the west implying a complex shock structure.

3. The brush region is remarkably filamentary. In the brush region, we find several 3 to 5 kpc arc-shaped filaments, 'bristles', that are more or less perpendicular to the ridge. In addition to the downstream of the ridge, we find three curved shaped filaments, the 'arches'.

4. The region B2 consists of two distinct linear filaments, the 'double strand', which connects the bright brush to B2. The B2 region also shows two thin parallel filaments, 'threads', that are separated by 5 kpc. At the intersection of the region B2 and B3, we find an arc-shaped filament, extending from north to south. The tip of this filament in B3 region seem to be connected to region B2 via a low surface brightness emission, the 'bridge'.

5. The fainter relic E consists of three bright compact regions. There are no optical counterparts at location of these compact region in emission. We do not find any nearby radio galaxies, which could be the source of radio emission.

6. The radio spectrum of relics B, D, and E follows power law spectrum between 150 MHz and 1.5 GHz. The integrated spectral index of the Toothbrush is -1.15 ± 0.02, yielding a Mach number of $\mathcal{M} = 3.78^{+0.3}_{-0.2}$.

7. We find that the uv-cut has a similar effect on the VLA, GMRT, and LOFAR data and does not affect the integrated spectral index significantly.

Chapter 5

Spectral and curvature analysis of the Toothbrush

The spectral properties of relics provide useful information about the energy spectrum of the relativistic particles and the magnetic field distribution in galaxy clusters. In this chapter, we present a multi-frequency study of the Toothbrush and the other two fainter relics. With the new VLA data, we can study the spectral index and curvature distribution of the Toothbrush down to $4.5''$ resolution.

5.1 Spectral analysis of the Toothbrush

The Toothbrush is known to show a clear spectral index gradient towards the cluster center (van Weeren et al., 2012a). The spectral steepening is considered to reflect the aging of the relativistic electron population in the post-shock areas of an outward moving shock. The new VLA observations allows us to create a high frequency high resolution spectral index map of the Toothbrush.

5.1.1 Spectral index map

To construct the spectral index maps, we first created images using both the LOFAR and the VLA data with a common inner uv-cut of $0.2\,\mathrm{k}\lambda$. This ensures that 'resolving out' a possible large-scale flux distribution has a similar effect on both data sets. Here, the $0.2\,\mathrm{k}\lambda$ uv-cut correspond to the minimum baseline sampled by the VLA data. For imaging, we use multiscale clean and $\mathtt{nterms} = 2$. The imaging uses uniform weighting for both data sets. The resultant images have slightly different resolutions due to different uv-coverages of the LOFAR and VLA data. Therefore, we convolved the VLA image and the LOFAR images to a common resolution i.e., $5''.5$. We then checked the astrometry and alignment of both the images. To have the same pixel position in both the images, we used the CASA task `imregrid`. Pixels with a flux density below $5\,\sigma_{\mathrm{rms}}$ in each of the individual images were blanked. Finally, we computed pixel-wise the spectral index maps, using the CASA task `immath`, by combining the final images

according to:

$$\alpha = \frac{\ln \frac{S_1}{S_2}}{\ln \frac{\nu_1}{\nu_2}} \tag{5.1}$$

where S_1 and S_2 are the flux density values at each pixel in the VLA and LOFAR maps at the frequencies $\nu_1 = 1500\,\mathrm{MHz}$ and $\nu_2 = 150\,\mathrm{MHz}$.

In order to derive the spectral index uncertainty map, we take into account the image noise and the absolute flux calibration uncertainty. The flux scale uncertainty f_{err} of VLA L-band is about $4\,\%$ (Perley and Butler, 2013) and for LOFAR we assume it to be $10\,\%$. We estimate the spectral index error via:

$$\Delta\alpha = \frac{1}{\ln\left(\frac{\nu_1}{\nu_2}\right)} \sqrt{\left(\frac{\Delta S_1}{S_1}\right)^2 + \left(\frac{\Delta S_2}{S_2}\right)^2} \tag{5.2}$$

where ΔS_1 and ΔS_2 were calculated as:

$$\Delta S_j = \sqrt{(f_{\mathrm{err}} \times S_j)^2 + (\sigma_{\mathrm{rms}}^j)^2} \tag{5.3}$$

where $j \in 1, 2$ and σ_{rms}^j is the corresponding RMS noise in the image.

The $5\farcs5$ resolution spectral index map of the Toothbrush between 150 MHz LOFAR and 1.5 GHz VLA data is shown in Figure 5.1. The map evidently confirms the remarkably uniform spectral steepening towards the cluster center, varying roughly from -0.68 to -2.0. These values are in agreement with van Weeren et al. (2016). The B2 region, where the double strand appears twisted, shows the flattest spectral index, namely $\alpha = -0.68 \pm 0.06$. The B3 region also shows a few patches with a flat spectral index.

From our high resolution spectral index map, interesting details become visible: at the ridge, the spectral index is slightly flatter than reported earlier (van Weeren et al., 2016), namely $\alpha = -0.75 \pm 0.05$. In the double strand, it becomes evident that at the northern strand the spectral index is flatter and downstream of it, the spectrum is steeper. Surprisingly, at the southern strand the spectrum again becomes flatter. The change in the spectral index across the double strand might be due to a new injection. Another possible explanation for the change in the spectral index across the double strand could be an increase in the strength of the local magnetic field which brightens up the emission and flattens the spectrum.

To investigate the spectral index distribution along the northern edge of the Toothbrush, with distance increasing from east to west, we determine the spectral indices in small square regions, see Figure 5.2 top panel. The size of these boxes are approximately equal to the restoring beam size of the map, i.e., $5\farcs5$. The extracted spectral
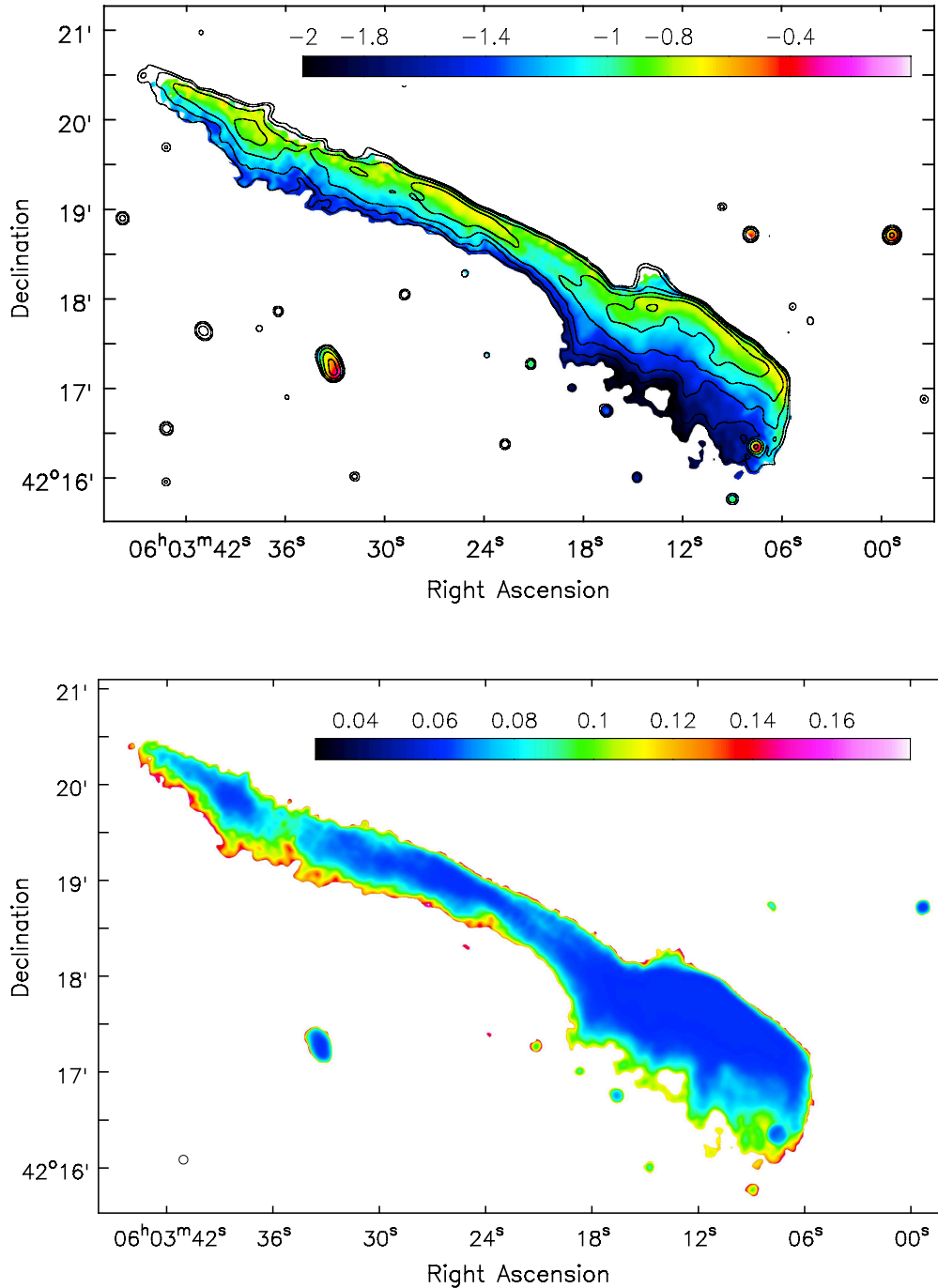
Figure 5.1: *Top:* Spectral index map of the Toothbrush between $150\,\text{MHz}$ and $1.5\,\text{GHz}$ at $5''5$ resolution, overlaid with the VLA contours. The contour levels are drawn at $[1, 2, 4, 8, \dots] \times 4.5\,\sigma_{\text{rms}}$ and are from the VLA image. The color bar shows spectral index α from -2 to -0.4. *Bottom:* Corresponding spectral index uncertainty map. (Figure adopted from Rajpurohit et al., 2017).
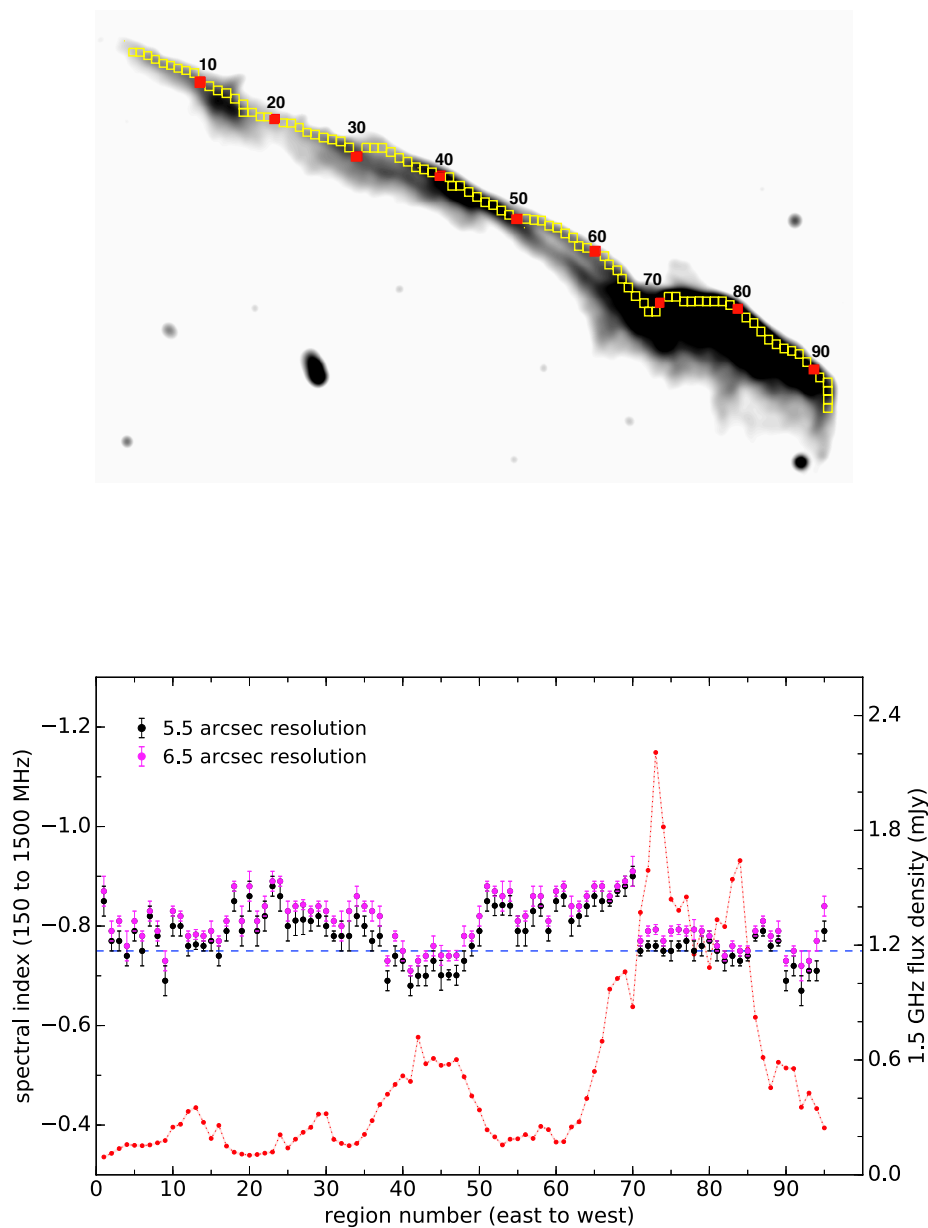
Figure 5.2: *Top:* Box distribution across the Toothbrush overlaid on the VLA total intensity map at 5″.5 resolution. The width of the boxes used to extract the indices is 5″.5. *Bottom:* Extracted spectral index between 150 and 1500 MHz across the Toothbrush, from north to south, with the distance increasing from east to west. The dashed blue horizontal line indicates the average spectral index of $\alpha = -0.75 \pm 0.05$ at the ridge. A shift in the spectral indices is clearly visible across the entire relic caused by lowering the resolution. The red dots trace the VLA 1.5 GHz flux density along the relic, corresponding to the spectral indices shown with the magenta color, revealing a correlation between the brightness and the spectral index. Systematic uncertainties in the flux-scale were included in the error bars.

index profile is shown in the Figure 5.2 bottom panel with black dots. At the north-
ern edge of the Toothbrush, the spectral index varies mainly between -0.70 to -0.90.
However, at the shock front the spectral index is roughly about -0.75, which is con-
sistent with what we obtained from the spectral index maps. The obtained values are
slightly flatter than reported by van Weeren et al. (2016). To compare our spectral
index map with that of van Weeren et al. (2016), we also create a spectral index map at
a $6\rlap{.}''5$ resolution. The extracted spectral indices from the $6\rlap{.}''5$ resolution map is shown
in Figure 5.2 bottom panel with the magenta dots. The spectral index at the shock
front is about -0.80 and is consistent with van Weeren et al. (2016). Evidently, there
is a shift in the spectral indices across the entire radio relic caused by lowering the
resolution. This raises the question how we can identify the actual injection spectrum
at the shock front. Our investigation indicates that the spectral index flattens with
increasing resolution, hence with an even better resolution, we may even find flatter
spectral indices.
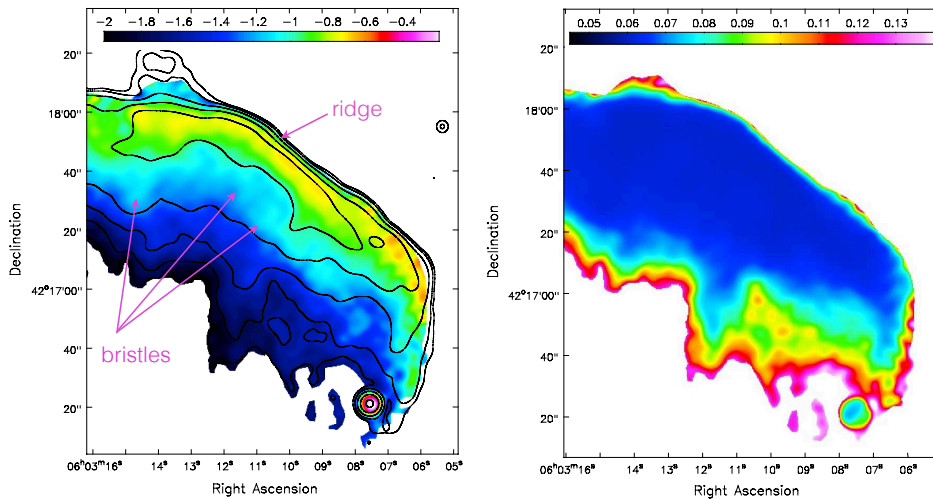
Figure 5.3: High resolution ($4\rlap{.}''5$) spectral index map of the brush region, between $150\,\mathrm{MHz}$ to
$1.5\,\mathrm{GHz}$, demonstrating at the ridge spectral index is in the range $-0.70 \le \alpha \le -0.80$. Contours
show the VLA flux density distribution. Contour levels are drawn at $[1, 2, 4, 8, \dots] \times 4.5\,\sigma_{\mathrm{rms}}$, where
$\sigma_{\mathrm{rms}} = 7\,\mathrm{\mu Jy\ beam^{-1}}$. The color bar shows spectral index α from -2.2 to -0.6. *Right*: Corresponding
spectral index uncertainty map.

As mentioned above, the spectral index flattens with increasing resolution, therefore,
to obtain the flattest spectral index across the Toothbrush, we produce the VLA and
LOFAR image at $4\rlap{.}''5$ resolution, i.e., the maximum resolution achieved with the LOFAR
data. We blanked pixels with values less than $5\,\sigma_{\mathrm{rms}}$. The resultant spectral index map
is shown in Figure 5.3. Due to limiting signal-to-noise ratio of the LOFAR data at the
B2 and B3 regions, the spectral index map of the entire relic cannot be shown and
analyzed at $4\rlap{.}''5$ resolution. From Figure 5.3, it is evident that at the location of the
shock , the spectral index is apparently flatter than the one obtained from the $5\rlap{.}''5$

spectral index map, namely $-0.70 \leq \alpha \leq -0.80$, confirming that the flattest spectral index obtained is resolution dependent.

Viewed at such a high-resolution (Figure 5.3), the spectral index map of the brush region shows small-scale features that were detected in the total intensity maps, for instance, we can now see that the bristles tend to have a slightly flatter spectrum. At the location of the shock, the spectral index is apparently flatter, namely $-0.70 \leq \alpha \leq -0.80$. Interestingly, the spectrum already steepens across the ridge from $\alpha = -0.70$ to -0.96. Moreover, the spectral index at the shock front shows some variations as already noticeable in Figure 5.3.

The spectral index steepening along the 'streams' of emission that emerges from the brush is also visible as reported by van Weeren et al. (2016). In fact, a clear north-south gradient is also seen across the streams, with a steepening up to -2.0 ± 0.10 at the southern ends. However, we do not find any evidence of the spectral index flattening at the southern end of the streams as found by van Weeren et al. (2016).

We also investigate the radio brightness distribution across the northern edge of the Toothbrush, with distance increasing from east to west. The resultant plot is displayed in Figure 5.2. It is evident that the relic brightness is not uniform across its extension. Interestingly, the ridge also shows brightness variations.

The comparison of the spectral index with brightness distribution along the northern edge of the Toothbrush, from east to west (same region where we extracted spectral indices) reveals that there is a correlation between these two, i.e., brighter regions tends to be flatter. Variations on the order of 0.2 in the spectral index are seen in the brightest regions, like in the brush. For a curved electron energy distribution, an increase in the magnetic field strength will increase the emissivity which brightens the emission and flattens the spectrum (Ellison and Reynolds, 1991). Thus brighter regions should have flatter spectra and the presence of correlation between spectral index and brightness favors this interpretation. To check a possible correlation between the spectral index and the brightness, we perform a Spearman's rank correlation test. We find that the p-value is less than 0.05, which indicates that the correlation is statistically significant.

5.1.2   Spectral curvature maps

All of the known models for the formation of relics predict a spectral curvature gradient towards the cluster center. This is believed to reflect the active acceleration at the location of shock front and radiation losses in the downstream region. The Sausage relic is the only known relic with a clear detection of the curvature gradient (Stroe et al.,
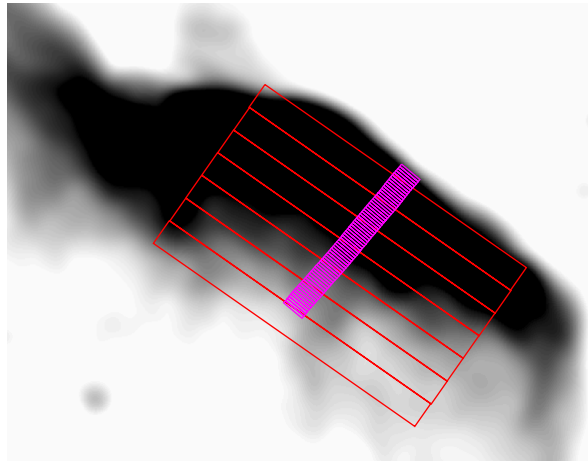
Figure 5.4: Regions used for studying the brush region.The width of each magenta colored rectangular box is $0\rlap{.}''7$ corresponding to 2.5 kpc. The full length of the magenta region is about 164 kpc.

2013). We used the LOFAR , GMRT, and VLA observations to derive the curvature map for the Toothbrush. We convolved all maps to 5.5 ″resolution and re-grided them with respect to the 1.5 GHz VLA image. The spectral curvature map (SC) at three frequencies were derived as

$$SC = -\alpha_{\nu_2}^{\nu_1} + \alpha_{\nu_3}^{\nu_2} \tag{5.4}$$

where ν_1 is the lowest frequency (150 MHz), ν_2 is the central frequency (610 MHz) and ν_3 is the highest one (1500 MHz).

The resulting map is shown in left panel of Figure 5.5 left panel. We blanked all pixels below $5\sigma_{\rm rms}$. A curvature gradient from north to south across the Toothbrush is clearly visible. The spectral curvature mainly varies between 0 to -1.2. The accepted models for acceleration of particles predict zero curvature at the shock front and increase in the spectral curvature into the downstream areas.

From our curvature map, it is evident that at the shock front, the SC ~ 0, indicating that all electrons emitted between 150 to 1500 MHz were recently accelerated. However, due to some faint upstream emission in the LOFAR 150 MHz image (very likely related to the imaging artifacts in the LOFAR image), the curvature at the upstream edge of the shock is not exactly zero. In the downstream area, the curvature increases to -1.2 because of the energy loses, mainly through synchrotron radiation and IC scattering. We also observe small scale sub-structure, possibly bristles, in the brush region where the SC varies. This suggests that these sub-structures may have a spectral break at different frequencies.
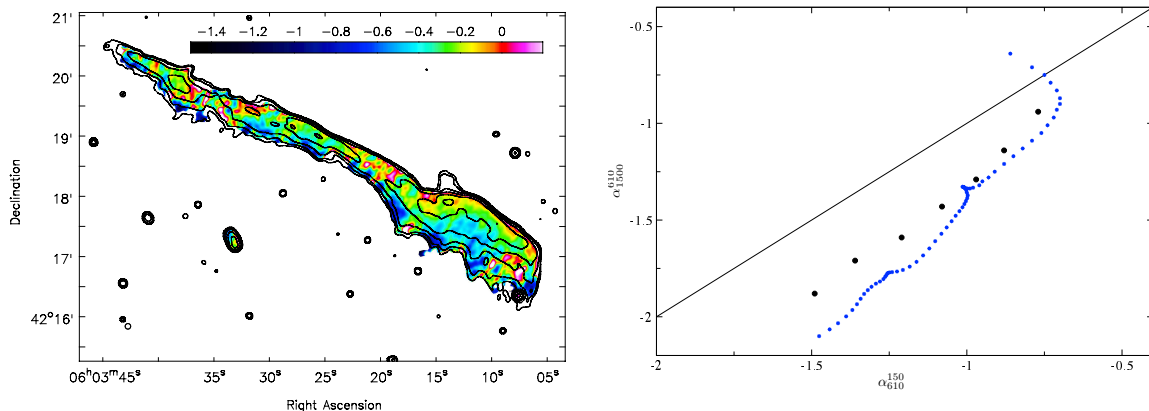
Figure 5.5: Curvature map of the Toothbrush relic between 150 to 1500 MHz at 5.5″ resolution. *Right*: Radio color-color plot of the brush region. Black data point shows the extracted spectra from red boxes. Blue data points are extracted from magenta colored boxes. In both plots, the contour levels are drawn at $[1, 2, 4, 8, \ldots] \times 4\sigma_{\mathrm{rms}}$, $\sigma_{\mathrm{rms}} = 8\ \mu\mathrm{Jy\ beam}^{-1}$ and are from VLA image.

5.1.3 Radio color-color diagrams

To gain more insight into the spectral shape across the relic emission, we employed the color-color plots described by Katz-Stone et al., 1993. The color-color plots are useful for determining injection spectral index and for distinguishing source regions with different properties which in turn can give additional insight into the physical process taking place at these emitting regions, for instance spectra at different location indicates the energy losses of the radiating particles. To created the color-color plot, first we constructed high and low frequency spectral index maps. The low frequency spectral index was created using 150 and 610 MHz observations and the high frequency spectral index was obtained using 610 and 1500 MHz observations.

We performed the spectral analysis for B1 region only. The color-color plot for the B1 region is plotted in Figure 5.5 right panel. We first consider regions averaged over larger volumes. The black points show the spectra extracted from the red regions (Figure 5.4), when averaged over the large area. The resulting profile for B1 is somewhat similar to what has been reported by van Weeren et al. (2012a). The intersection point at $\alpha_{610}^{150} = \alpha_{1500}^{610}$ gives an injection spectral index. However, there is no obvious intersection point in the measured data, since the measured curve is slightly bent.

After this, we make a color-color plot for the region with green boxes (Figure 5.4). We considered small regions to include and investigate the small-scale features. The resultant plot is shown with blue points. The color-color plot shows a strange 'arc' towards the upstream. A shift in the source position or a different effective resolution of the images could originate such an arc-shaped spectrum. Therefore, we checked point sources in the field to verify that there is no offset between the LOFAR, GMRT,

and VLA images but we do not find any systematic effect. However, such a curve is hard to explain by any aging models.

5.2 Spectral index map of relics E and D

The spectral index map for fainter relics is shown in Figure 5.6. To create the spectral index map for relics E and D, we convolved the VLA and LOFAR image to a common resolution of $11'' \times 11''$.
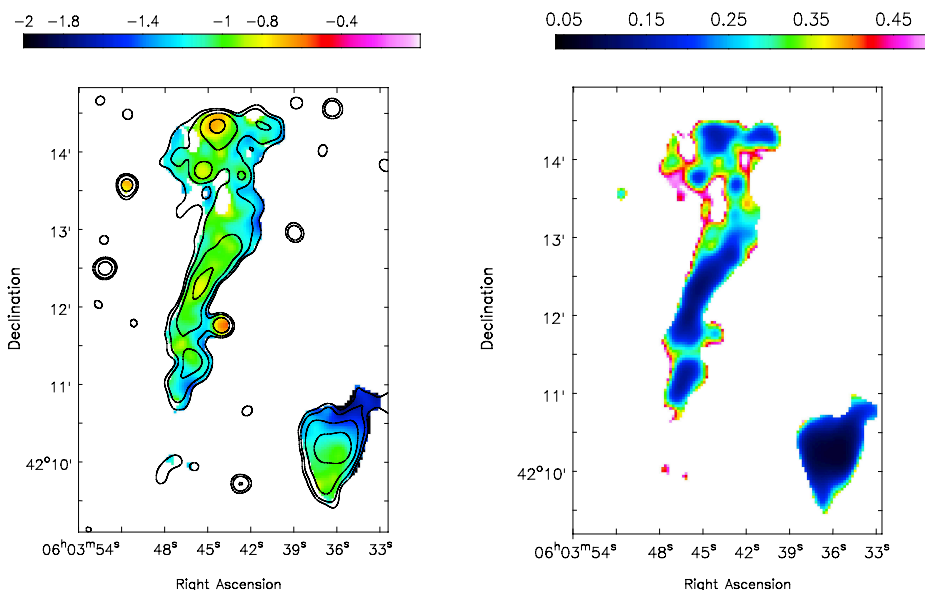
Figure 5.6: *Left:* Spectral index map for the relics E and D between 150 and 1500 MHz at $11.0''$ resolution. Contour levels are from the VLA and drawn at $[1, 2, 4, 8, \ldots] \times 4.5\,\sigma_{\mathrm{rms}}$, where $\sigma_{\mathrm{rms}} = 12\,\mu\mathrm{Jy\,beam^{-1}}$. *Right:* Corresponding spectral index uncertainty map.

The spectral indices in relic E range from -0.70 to -1.50. For some regions of relic E, our high resolution spectral index map reveals a relatively flat spectral index of about -0.70 ± 0.10, see Figure 5.6. We investigate regions showing a flatter spectral index and searched for compact radio sources with optical counterparts. From the radio-optical overlay (Figure 4.8) it is clear that the brightest regions (EA, EB, and EC), showing a flat spectral index, namely $\alpha = -0.70$, do not show any optical counterparts. The spectral index and brightness distribution across the relic, with distance increasing from north to south, is shown in Figure 5.7. For relic E, there seems to be no correlation between the spectral index and brightness.

Relics are expected to show a spectral index gradient, as the Toothbrush or Sausage-relic (van Weeren et al., 2010; van Weeren et al., 2012a; van Weeren et al., 2016; Hoang et al., 2017). We do not find a significant spectral index gradient towards the cluster center, i.e., from east to west, for relic E.
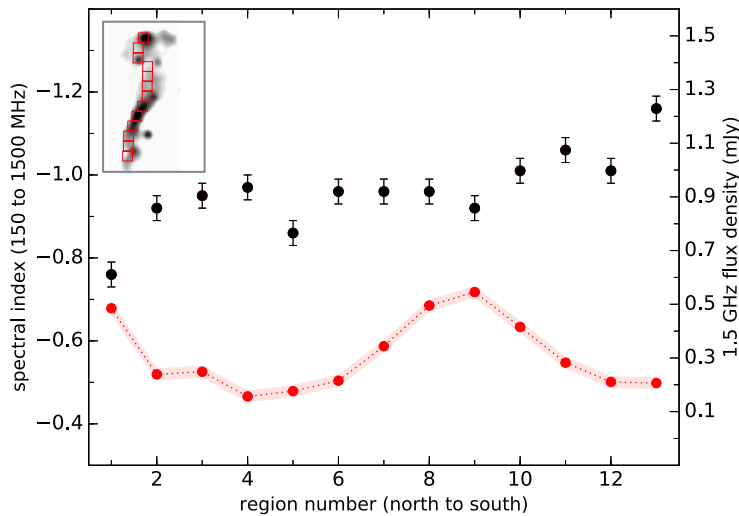
Figure 5.7: Extracted spectral index between 150 MHz and 1.5 GHz across relic E, from north to south, is shown with black dots. The red dots trace the VLA 1.5 GHz flux density across the relic, corresponding to the spectral indices shown with the black color. The red boxes have a width of 11″. Systematic uncertainties in the flux-scale were included in the error bars.

For relic D we confirm the southwest spectral index steepening, varying from -0.85 to -1.70, as reported by van Weeren et al. (2016). They found the spectral index for relic D is in the range of -0.90 to -1.40. It is interesting to see that the spectrum flattens from south to west while the bright region of relic D (cone) is to the west which shows a relatively steeper spectrum.

5.3   Derived Mach numbers

We obtained an integrated spectral index of $\alpha = -1.15 \pm 0.02$ for the Toothbrush, yielding a Mach number of $\mathcal{M} = 3.78^{+0.3}_{-0.2}$, see Table 4.2.

Another way to obtain a Mach number using radio observations is to measure the injection spectral index directly from the high resolution spectral index maps. From the spectral index map, shown in Figure 5.3, we find that the flattest spectral index at the northern shock front is about -0.70. This injection corresponds to a Mach number of $\mathcal{M} = 3.3^{+0.4}_{-0.3}$. We do not find a significant discrepancy between the Mach numbers obtained from the injection spectral index and the integrated spectrum. The Mach number measured from the injection index is more or less consistent with the one obtained from the integrated spectral index. However, we would like to emphasize that the injection index measured from spectral index maps does not necessarily indicate the actual injection spectrum, as seen in Section 5.1.1. Hence, the Mach number obtained from the radio spectral index map is a lower limit.

The Chandra observations of 1RXS J0603.3+4214 revealed a weak shock of Mach number $\mathcal{M}_{X-ray} \approx 1.2$ at the northern edge of the Toothbrush (van Weeren et al., 2016). Thus, the observationally derived radio and X-ray shock Mach numbers differ significantly for this radio relic. The recent polarization study of the Toothbrush by Kierdorf et al., 2016 suggests that the relic lies behind the cluster. We argue that the X-ray observation underestimates the strength of the shock since un-shocked ICM along the line of sight lowers the measured surface brightness and temperature jumps. We suggest that the shock in the densest region is rather weak. Finally, the ridge branching indicates that the geometry of the shock front is complex and hence the transition might be significantly smeared out (Rajpurohit et al., 2017).

5.4   Summary

We presented the high frequency (150-1500 MHz) high resolution spectral index map of the Toothbrush and two fainter relics. The VLA observations in combination with published GMRT and LOFAR data allowed us to study the spectral distribution in detail. The main results are:

1. The spectral index map of the Toothbrush between 150 MHz and 1.5 GHz shows that the spectral index is in the range $-0.70 \leq \alpha \leq -0.80$ at the ridge, i.e., X-ray shock front. The spectral index changes within the ridge.

2. The spectral index changes across the double strand, suggesting either a new injection or a change in the magnetic field. From the spectral index map, we obtained a Mach number of $\mathcal{M} = 3.3^{+0.4}_{-0.3}$ for the Toothbrush.

3. The Mach number obtained from the injection index is more or less consistent with the one obtained from the integrated spectrum. However, we find that the spectral index maps can only provide a lower limit for the actual injection spectral index. The discrepancy between the X-ray and radio-derived Mach numbers may originate from the fact that the X-ray surface brightness is dominated by the densest region in the ICM along the line of sight, where the shock is rather weak

4. For the fainter relic E, we do not find a significant spectral steepening which would be typical for relics. We also report the occurrence of the flat spectral indices across the relic E, namely $\alpha = -0.70$ to -0.80.

Chapter 6

A giant extended radio halo in 1RXS J0603.3+4214

The massive galaxy cluster 1RXS J0603.3+4214 is known to hosts a Mpc-sized extended radio halo. In this chapter, we present the $1-2$ GHz detailed images of the radio halo present in this cluster, obtained from the VLA observations.

The halo was detected by van Weeren et al. (2012a) with the GMRT telescope. A more recent study performed with the LOFAR at 150 MHz shows that size of the halo is about 2 Mpc, and it appear to be connected to the brush region of the Toothbrush relic. These observations also revealed a remarkably uniform spectral index distribution across the halo, namely $\alpha = -1.16$ (van Weeren et al., 2016). It has been found that the radio halo and the brush region of the Toothbrush are connected by a region with a spectral index of $\alpha = -2.0$ after which the spectrum flattens gradually to $\alpha = -1.0$ and returns to being uniform in the central part of the halo. van Weeren et al. (2016) suggested that the flattening of the spectral index is due to the re-acceleration of perviously shock accelerated electrons by merger-induced turbulence, indicating a connection between the shock and turbulence. They also reported that the southern end of the radio halo is edge sharpened and is characterized by high temperature map, namely $11 - 15$ keV. Recently, a merger driven shock front and a cold front is also detected in the southern part of the halo (van Weeren et al., 2016).

6.1 VLA 1-2 GHz total intensity images

The 1-2 GHz VLA radio continuum images of the radio halo in 1RXS J0603.3+4214 at different resolutions are shown in Figure 4.1. Our VLA images confirms the extended radio halo emission. The halo emission is not detected at very high resolution due to its low surface brightness, for example at $5''$ (Figure 4.1 panel (d)). At 1-2 GHz, the radio halo has a largest angular size of about $8.'7$ corresponding to a physical extent of 1.7 Mpc.

The shape of the halo in the VLA images is similar to that of the low frequency LOFAR and the GMRT images, i.e., mainly elongated along the merger direction.
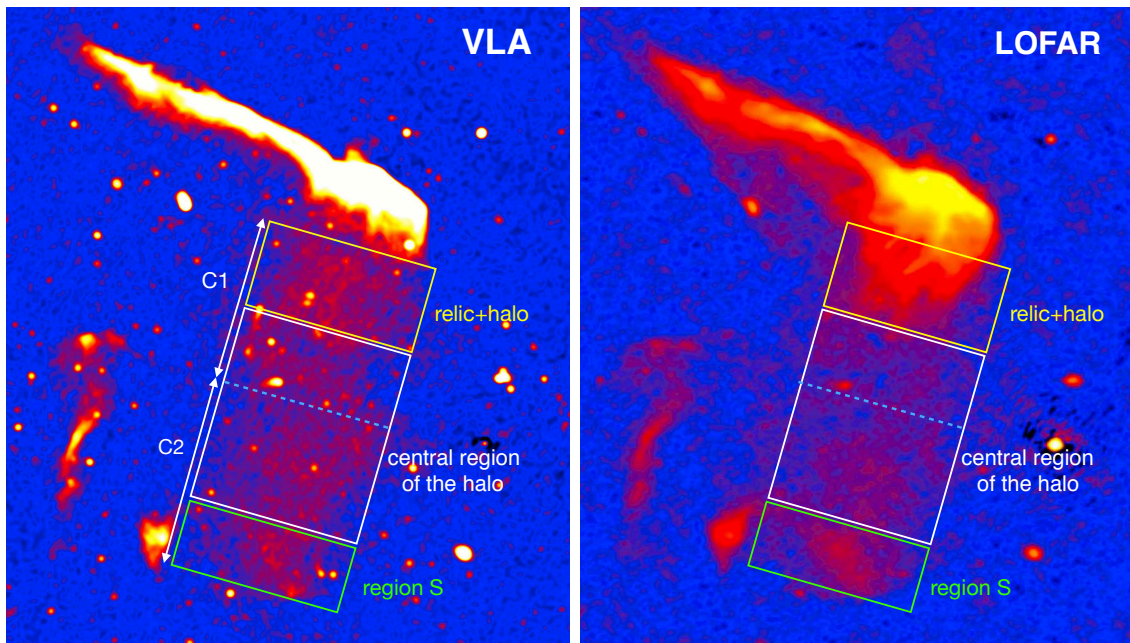
Figure 6.1: A comparison of the radio halo at VLA 1-2 GHz and the LOFAR 120-181 MHz (van Weeren et al., 2016). Both images have similar resolution of 7″. To compare radio morphologies at these two frequencies, colors in both images were scaled manually. In both images the yellow rectangular box indicates the 'relic+halo' region. The dashed line denotes a boundary between the C1 and C2 region of the radio halo. The C1 and C2 regions are divided on the basis of the X-ray subclusters boundary. The southernmost part of the halo is denoted as region S. We define that region of the halo which excludes both the relic+halo region and region S as 'central region'.

Radio halos usually have smooth morphologies, however, in the present halo emission appears patchy. van Weeren et al. (2012a) subdivided the halo into two distinct regions, namely C1 and C2, see Figure 4.1 panel (d). Unlike LOFAR 150 MHz image, the VLA image clearly show a slight decrease in the surface brightness which apparently separates the relic (Toothbrush) and the halo i.e., where the relic B emission ends and the halo C emission starts, see Figure 6.1. It is worth noting that the transition from the halo to relic, i.e., from regions where different types of diffuse emission dominate the surface brightness, appears at a different location in the VLA image than the LOFAR image.

In our VLA high resolution radio maps, we detected 32 discrete sources ($>5\,\sigma_{\mathrm{rms}}$) within the halo region, including several head-tail radio galaxies. These radio sources were not detected in the perviously published data. The measured flux density of the entire radio halo at 10″ resolution, without subtracting these 32 sources, is $53.0 \pm 4.0\,\mathrm{mJy}$. We use our sensitive high resolution image to measure the flux densities of the compact sources in the halo region which may contribute to the total flux density at the lower resolution. The combined total flux density of the 32 discrete sources is $\sim 13\,\mathrm{mJy}$, which means $\sim 25\%$ of total flux resides in these sources. The flux density of the halo hence amounts to $S^{\mathrm{halo}}_{1.5\,\mathrm{GHz}} \sim 40.0\,\mathrm{mJy}$.

In the VLA high resolution maps, we find that there are several radio galaxies embedded within the C1 region, for example sources labeled as J, K, L ,T, and S, see Figure 4.1 panel (d) for labeling. The measured flux densities of the C1 and C2 regions are about 24 mJy and 29 mJy, respectively. We confirm that the southern part of the radio halo shows a sharp outer edge.

6.2   Analysis of the halo

To study the spectral characteristics of the radio halo, we use the VLA 1-2 GHz, GMRT 610 MHz and the LOFAR 120-181 MHz observations. We also use the Chandra observations to study the X-ray emission.

6.2.1   Integrated spectrum

As mentioned in Chapter 4, the radio observations reported here were performed using three different interferometers each of which has different uv-coverages. This results in a bias in the total flux density measurements, the integrated spectra, and the spectra index maps. To overcome these biases, we create images at 150 MHz and 1.5 GHz with a common minimum inner uv-cut of $0.2 \, k\lambda$. Here, $0.2 \, k\lambda$ is the minimum uv-distance of the LOFAR data. These images were created using uniform weighting as it compensates best for differences in the sampling density in the uv-plane when combining different interferometric data with non-identical uv-coverages (Stroe et al., 2016). We do not include the GMRT 610 MHz observations for the halo spectral studies because the GMRT 610 MHz data suffers from missing short baselines, which is crucial for faint extended emission.

To obtain the integrated spectral index of the radio halo, we convolve the LOFAR and VLA images to the same beam size of $11'' \times 11''$. We divide the halo into three regions, namely 'relic+halo', central region and region S (Figure 6.1). We note that 'relic+halo' region belongs to the relic (Toothbrush) according to the surface brightness at 150 MHz but at 1.5 GHz to the halo. Therefore, when determining the integrated spectrum of the halo, this region is excluded. We also exclude the region S for computing the integrated spectral index of the halo as this region may have a different origin (Section 6.2.2). The region S is not visible in the 610 MHz high resolution images. Therefore, to obtain the integrated spectral index of region S, we convolve the LOFAR, GMRT and VLA images to the same beam size of $20'' \times 20''$.
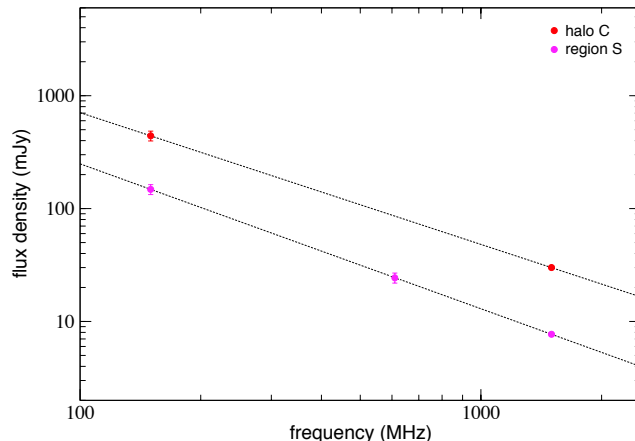
Figure 6.2: Integrated spectra of the radio halo and region S. Dashed lines are fitted straight power-laws. The regions where the integrated flux densities were measured are shown in Figure 4.11. The radio spectrum of region S is steeper than the halo spectrum.

The resultant integrated spectra of the halo and the southern part of the radio is shown in Figure 6.2. For the radio halo, we find an integrated spectral index of -1.17 ± 0.04. The integrated spectral index of region S is -1.28 ± 0.05, which is steeper than the spectral index of the halo, and is well described by a single power law spectrum.

Feretti et al. (2004a) and Giovannini et al. (2009) claimed a correlation between the radio halo integrated spectral index and the average X-ray gas temperature. According to this correlation, clusters with higher temperature ($T \geq 10$ keV) tend to host halos with a flatter spectrum (an average spectral index about -1.2), while cooler clusters ($T \leq 8$ keV) host steep spectrum halos (an average spectral index of about -1.7). 1RXS J0603.3+4214 is a moderately hot cluster with a rather shallow integrated spectrum. This may favor the re-acceleration models since, clusters with high temperatures are more massive and undergo a violent merger, resulting in supplying more energy to the radio-emitting particles.

6.2.2 Radio and X-ray comparison

In many cases, the morphological features of radio halos show a close similarity to the X-ray features, indicating a connection between the hot and relativistic plasmas (Govoni et al., 2001a). However, there are also some systems in which the radio halo emission does not appear to follow the X-ray emission very well, for example in the Coma cluster (Brown and Rudnick, 2011), Abell 3562 (Giacintucci et al., 2005), and MACS J0717.5+3745 (Bonafede et al., 2012; van Weeren et al., 2017a).

The X-ray observations of the cluster 1RXS J0603.3+4214 showed that the ICM is dominated by two main components (Ogrean et al., 2013; van Weeren et al., 2016).

The southern component is brighter than the northern one. The X-ray observations also revealed the presence of a cold front at the southern edge of a triangular 'bullet-like' structure. In Figure 6.3 left panel, we compare the X-ray and radio morphology of the halo emission. Evidently, the X-ray and radio morphology are strikingly similar, indicating a connection between the thermal gas and relativistic plasma.
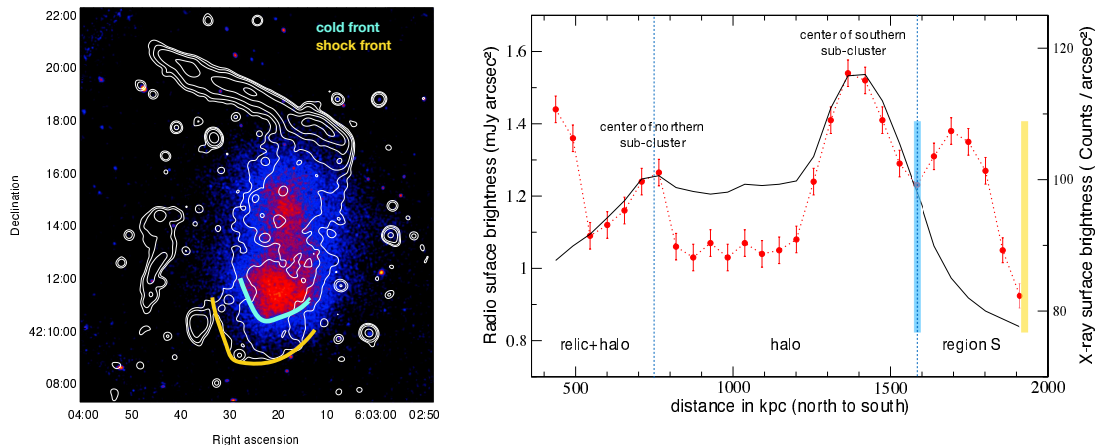
Figure 6.3: *Left*: VLA 1-2 GHz radio contours superposed on the smoothened Chandra X-ray image (0.5 to 2 keV band). The resolution of the VLA image is $15''$. Contour levels are drawn at $[1, 2, 4, 8, \dots] \times 4.5\,\sigma_{\mathrm{rms}}$, where $\sigma_{\mathrm{rms}} = 16\,\mu\mathrm{Jy\,beam}^{-1}$. The yellow line shows the location of the southern shock front detected in Chandra observations. *Right*: Xray-radio surface brightness profiles along the major axis of the radio halo. The 1.5 GHz VLA brightness profile at a resolution of $16''$ is shown with red dots while the Chandra X-ray profile with a black solid line. The vertical yellow and blue dashed line indicate the location of the shock front and the cold shock front. (Adopted from Rajpurohit et al., 2017).

The emission from the radio halo extends all over the detected X-ray emission. The X-ray surface brightness enhancement between the two sub-clusters component and the radio surface brightness in the same region trace each other. However, the radio emission extends further to the south where the X-ray emission is fainter, namely region S. van Weeren et al. (2016) recently dectected a shock front at the southern edge of region S, shown with a yellow line in Figure 6.3. The southern boundary of region S aligns nicely with the southern shock. A similar positioning is observed in some other systems as well, for example in the Bullet cluster (Shimwell et al., 2014), A754 (Macario et al., 2011), A2744 (Owers et al., 2011; Pearce et al., 2017), A520 (Vacca et al., 2014) and the Coma cluster (Uchida et al., 2016).

In order to examine and compare the X-ray and radio emission along the line from C1 to C2 region with distance increasing from north to south, we extract the average brightness pixelwise. We first subtract discrete unrelated sources embedded in the halo and then measure the surface brightness in regions indicated with green in Figure 6.6. The resultant profile is shown in Figure 6.3 right panel. The X-ray and radio profile clearly show two sub-cluster components. The center of the northern and the southern

sub-cluster of the radio emission coincides with the X-ray morphology and there is no offset. Moreover, the radio profile reveals a region of prominent enhanced emission which does not correlate with the X-ray structure, i.e., the region between the cold front and the southern shock front.

The X-ray and radio brightness profile suggests that the emission in region S may have a different origin than that of the halo, see Figure 6.3 right panel. A cluster undergoing a merger drives shocks and generates turbulence throughout the ICM, providing potential acceleration sites for relativistic particles responsible for radio halos (Feretti et al., 2012; Brunetti and Jones, 2014). As there is a shock detected at the southern edge of region S, therefore, this region could be related to that shock front.
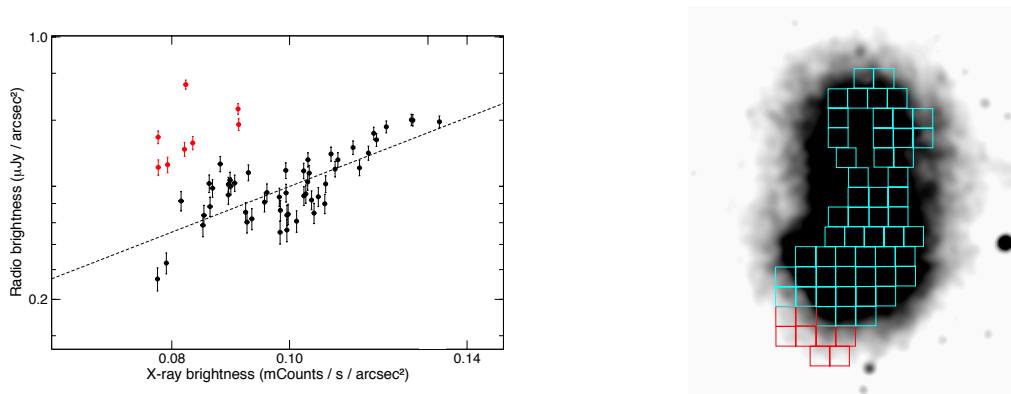
Figure 6.4: *Left*: $I_{\mathrm{radio}} - I_{\mathrm{X-ray}}$ relation of the radio halo in 1RXS J0603.3+4214. The error-bars represent the RMS of the brightness distribution within each cell. The black dashed line indicate a power-law fit. *Right:* The Chandra X-ray image in the 0.5 to 2 keV band is shown in grey scale. Red and cyan boxes show the regions used for extracting the fluxes. Both cyan and red cell have a width of 30″. The surface brightness extracted in cyan cell are indicated by black dots. The red dots are extracted across the southernmost part of the radio halo, i.e., region S. (Figure adopted from Rajpurohit et al., 2017).

In several clusters hosting a giant radio halo, a radio to X-ray spatial correlation has been observed, e.g., in Abell 2319, Abell 2163, Abell 2744, Abell 520, Abell 2255 and the Coma cluster (Govoni et al., 2001a; Govoni et al., 2001b; Feretti et al., 2001; Venturi et al., 2013; Vacca et al., 2014). To investigate such a correlation in the present radio halo, we perform a quantitative point-to-point comparison of the radio and X-ray brightness. We exclude regions where there is a point source. The plot of the radio versus X-ray brightness excluding region S is shown in in Figure 6.4. We find that the radio brightness correlates well with the X-ray brightness: a higher X-ray brightness is associated with a higher radio brightness. The data is fitted with a power law of the type:

$$I_{\mathrm{radio}} \propto I_{\mathrm{X-ray}}^{b}, \tag{6.1}$$

where the radio brightness I_{radio} and X-ray brightness $I_{\text{X-ray}}$ are expresses in expressed in $\mu\,\text{Jy\,beam}^{-1}$ and mCounts $s^{-1}\text{arcsec}^{-2}$, respectively. We obtain a slope of $b = 1.25 \pm 0.16$. This is more or less consistent (within $2\,\sigma$) with the radio surface brightness proportional to the X-ray surface brightness, as found for other giant radio halos (Govoni et al., 2001a; Govoni et al., 2001b).

The radio and the X-ray brightness distribution across region S, i.e., the region between the cold front and the southern shock front, is indicated by red dots in Figure 6.4. The region S is evidently distinct and does not appear to be connected with the rest of the halo.

6.2.3   Spectral index maps

The radio halo spectral index maps provide useful information on their origin and connection with the merger processes. The spectral index distribution is also important to test predictions of different models for the electron energy distribution. For example, a systematic variation of the radio halo spectral index with distance from the cluster center is predicted by re-acceleration models (Brunetti et al., 2001). The correlation between the spectral index and the thermal gas temperature reflects a possible link between the thermal and non-thermal components of the ICM (Feretti et al., 2004b; Orrú et al., 2007). According to this scenario, the flattest spectra correspond to regions with the highest temperature. Moreover, the presence of the halo in 1RXJ0603.3+4214 with an elongated morphology and the relic B to its north implies a possible connection between the halo and the shock wave (van Weeren et al., 2016).

Figure 6.5: *Left:* Spectral index map of the radio halo between 150 MHz and 1.5 GHz at $16''$ resolution. Contour levels are drawn at $[1, 2, 4, 8, \dots] \times 4.5\,\sigma_{\text{rms}}$, where $\sigma_{\text{rms}} = 16\,\mu Jybeam^{-1}$ and are from the VLA image. *Right:* Corresponding spectral index uncertainty map. (Figure adopted from Rajpurohit et al., 2017).

The VLA and LOFAR images allow us to create the spectral index map for present radio halo at high resolution with high accuracy. To make the spectral index map of the halo between 1.5 GHz and 150 MHz, we employ the same weighting and uv-cut, as mentioned in Section 6.2.1. We convolve the LOFAR and VLA images to a common resolution. Pixels with flux densities below $5\sigma_{\mathrm{rms}}$ in each of the images were blanked before making spectral index maps. We did not subtract the extended or point like discrete sources, however, these sources can be well identified from the halo emission. The 11″ spectral index map presented here is used to study the variation of the spectral index when moving from north to south since, we cannot study this variation at higher resolution, e.g., 16″ map. We note that the spectral index uncertainties across the halo are very small and at such a high resolution, these are by far one of the best resolved spectral index maps of a halo ever made.
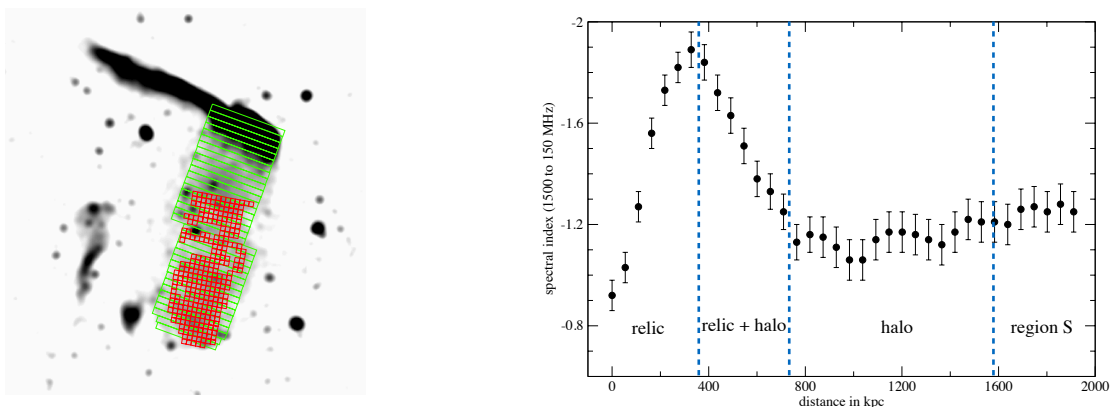
Figure 6.6: *Left:* VLA 1-2 GHz image depicting the regions where spectral indices were extracted. The image has a resolution of 16″. The green boxes have a width of 16″ while red one of 11″ . *Right:* Extracted spectral index across relic B1 and the radio halo, from north to south. Here, 'relic+halo' indicates the combined emission from the Toothbrush and the halo. Systematic uncertainties in the flux-scale were included in the error bars.

The spectral index map of the radio halo at 16″ is shown in Figure 6.5. The spectral index across the entire halo varies between −2.0 and −0.95 and shows a slight gradient from north to south. As argued earlier there is a region where, the halo dominates the surface brightness at 1.5 GHz while the relic dominates at 150 MHz; this region is denoted as 'relic+halo'.

The spectral index distribution from north to south, covering the B1 region of the Toothbrush and the entire radio halo is shown in Figure 6.6 right. Moving from the C1 towards C2, the spectral index varies mainly between −0.90 to −1.90. The spectrum first steepens in the post-shock regions to −1.90 (360 kpc). After this, the spectrum gradually flattens over a distance of about 400 kpc (relic+halo region). For a distance of 800 kpc, the spectrum remains relatively constant with a mean of −1.16 (central halo region). Interestingly, on a smaller scale, the southern edge of the halo region appears
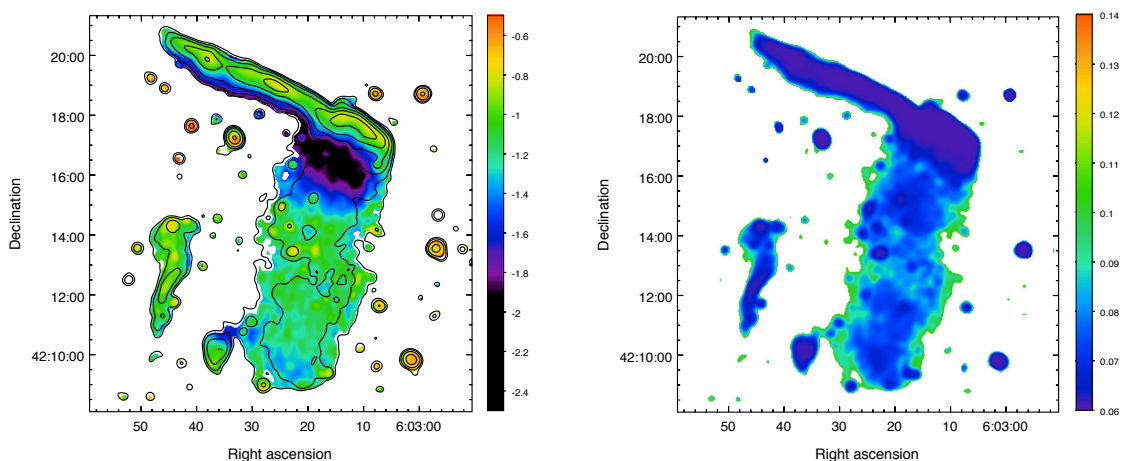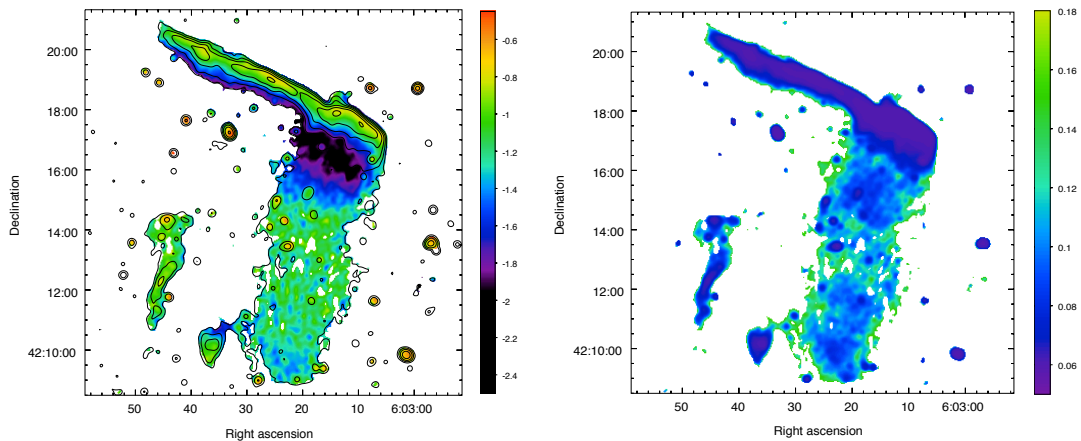
Figure 6.7: *Left:* High resolution spectral index map of the radio halo between 150 MHz and 1.5 GHz at 11″ resolution. The contour levels are drawn at $[1, 2, 4, 8, \dots] \times 4.5\,\sigma_{\mathrm{rms}}$, where $\sigma_{\mathrm{rms}} = 12\,\mu\mathrm{Jy\,beam}^{-1}$ and are from the VLA image. The color bar shows spectral index α from -2.4 to -0.6. *Right:* Corresponding spectral index uncertainty map.

slightly steeper. Moreover, we do not find a region with a steeper spectral index at the eastern part of the halo towards relic E, as found by van Weeren et al., 2016.

The high resolution spectral index map of the radio halo in 1RXS J0603.3+4214 is shown in Figure 6.7. It is evident from this map that the spectrum is steeper in the southern part of the radio halo than the rest of the halo. To study the spectral distribution across the radio halo, we extracted the spectral index in several regions as indicated in Figure 6.6 left panel by red boxes. The regions where the indices were extracted correspond to boxes with the physical sizes of about 36 kpc.

The resultant plot is displayed in Figure 6.8. Out of 278 boxes, 13 boxes with spectral index between -0.95 to -1.00 were excluded because of contamination by other sources (compact and extended). The spectral index across the central region of the radio halo varies mainly between -1.05 and -1.25. To estimate the measurement uncertainties, we followed the approach by Cassano et al. (2013). We find a raw scatter of 0.05 around the mean spectral index. For the radio halo in 1RXS J0603.3+4214, the spectral variations are much smaller than that of the radio halo in A665, A2163, A520, A3562, 1E 0657-55.8, and A2744 (Feretti et al., 2004a; Giacintucci et al., 2005; Orrú et al., 2007; Shimwell et al., 2014). As also seen in Figure 6.5, the southern end of radio halo is steeper and shows a clear spectral index gradient, see Figure 6.8.

6.2.4 Spectral index and temperature distribution

For the radio halo in Abell 2744, a point-to-point correlation has been observed for the first time, indicating that halo regions with flat spectra correspond to regions with
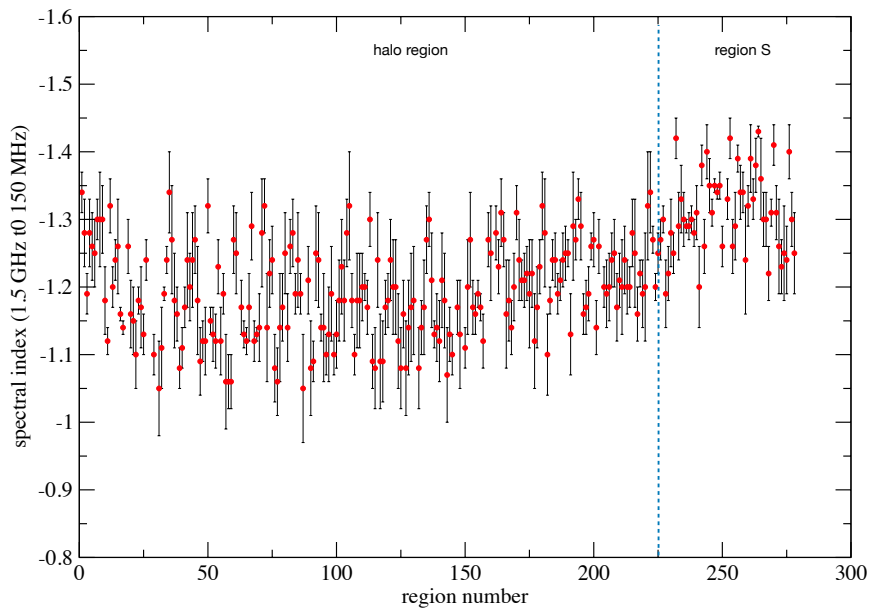
Figure 6.8: Spectral index distribution across the radio halo between 150 MHz and 1.5 GHz. The regions where we extract the spectral indices are shown in Figure 6.6 left panel with red. The region numbering is raw wise (from north to south).

hotter temperatures (Orrú et al., 2007). Such a trend is expected, since a fraction of the gravitational energy which is dissipated during cluster merger events into heating thermal plasma, is converted into re-acceleration of highly relativistic particles and amplification of the ICM magnetic field. However, a recent study of the same radio halo by Pearce et al., 2017 reveals that there is no statistically significant correlation. For the present radio halo, the point to point comparison of our high resolution spectral index map to that of the temperature map does not show any correlation. Hence, we confirm that there is no strong correlation between the radio spectral index and X-ray temperature. However, the southernmost part of the radio halo, i.e., Region S, is characterized by a hot ICM, namely $T = 14\text{-}15$ keV (Figure 3.2 right panel) but shows steeper radio spectrum.

6.2.5 Connection between the relic and the halo ?

The spectral index map of the Toothbrush shows a strong steepening in the downstream areas, while in the relic+halo region, the spectrum flattens progressively. It has been speculated that this spectral behavior indicates a possible connection between shock and turbulence (van Weeren et al., 2016). We note that at 150 MHz, see Figure 6.1, the brush region appears wider with several streams coming out of it, extending from the north to the south. The surface brightness across these streams is very high and the whole emission in this region is mainly dominated by the relic. In contrast, at 1.5 GHz

the same region is dominated by the halo emission. Therefore, the strong steepening and gradual flattening of the spectrum in the 'relic+halo' region could be due to the projection of the halo and the relic emission. It has been suggested, that the relic lies behind the cluster (Kierdorf et al., 2016). Hence, the relic and halo could be separated physically, but in projection, one finds the gradual steepening and flattening.

The southern boundary of the radio halo is relatively well defined and coincides with the southern shock front reported by van Weeren et al. (2016). This part of the radio halo was speculated to be a fainter relic but a uniform spectral index distribution disfavored this scenario. Our spectral index map reveals a spectral index gradient across region S, where the spectrum steepens to -1.4 in some areas. In addition, the region S doesn't appear to be associated with the rest of the halo where the radio emission shows clear similarity to the X-ray emission. The total extent of region S at $1.5\,\mathrm{GHz}$ is about 700 kpc. This region is also characterized by a hot ICM as expected for downstream emission of the southern shock front. Considering all evidences, we suggest that the southern part of the radio halo is actually a fainter relic.

6.3   Summary

We presented deep 1-2 GHz VLA images of the radio halo in the galaxy cluster 1RXS J0603.3+4214. Our observations confirm a giant radio halo present in the cluster. The main results are:

1. The VLA images revealed at least 32 discrete sources, together with several head-tail radio galaxies within the halo region that were not detected in perviously published observations.

2. The radio morphology of the central part of the halo shows close similarity to the X-ray emitting gas. However, the southernmost part of the radio halo appears distinct and may have a different origin.

3. We find that in the central part of the halo, the radio brightness correlates well with the X-ray brightness. A power-law correlation is found between the radio and X-ray surface brightness.

4. The VLA and the LOFAR data allowed us to create a spectral index map of the radio halo with high accuracy. We find that the mean spectral index across the central part of the halo is $\alpha = -1.16 \pm 0.05$. The spectral index of the halo also shows a slight gradient from north to south.

5. In the southernmost part of the radio halo, the radio spectrum is steeper than in the central part of the halo, suggesting a possible connection with the southern shock front detected in Chandra observations.

Chapter 7

Polarization analysis of the Toothbrush

Observations at radio wavelengths provide the best method for detecting magnetic fields. However, magnetic fields in the ICM are notoriously difficult to determine, the low density regions in the outskirts are even more challenging. Radio relics are unique probes of the properties of magnetic fields in the outskirts of galaxy clusters. Several radio relics are known to be polarized, some with high degree of polarization fraction, namely 50% to 60%. The polarization vectors (B-vectors) is often found to be well aligned with the shock surface. Hence the information about the magnetic field in the relics can be derived through the study of polarized emission.

In this chapter, we present the VLA L-band polarimetric observations of the Toothbrush. We first discuss the Faraday effect, Rotation Measures (RM) studies and depolarization. We also introduce the Rotation Measure Synthesis (RM-synthesis) to understand the structure of the magnetic fields.

7.1 Faraday Rotation

One of the most important physical effects to consider when discussing radio polarimetric observations is Faraday rotation. Magnetic field are present in many locations throughout the Universe, from our own galaxy Milky way, to other galaxies and clusters. When a linearly polarized radio wave propagates through a magnetized plasma, this plasma acts as a Faraday screen and rotates the plane of polarization. This phenomenon is called Faraday Rotation. The plane of polarization of the radio wave is rotated by an amount which depends on the Rotation Measure (RM) (Burn, 1966):

$$\psi_{\mathrm{obs}}(\lambda) = \psi_{\mathrm{int}} + \mathrm{RM}\,\lambda^2, \tag{7.1}$$

where $\psi_{\mathrm{obs}}(\lambda)$ is the observed position angle at wavelength λ and ψ_{int} is the intrinsic polarization angle, i.e., the angle before the plane of rotation. The RM could be determined using a linear least-square fit to the polarization angle as a function of frequency, i.e., $\mathrm{RM} = \frac{\Delta\psi}{\Delta\lambda^2}$. However, one major difficulty involved in determining the

RM in this way is the polarization angle is observationally constrained to values between 0 and π, leaving a freedom of addition of $\pm n\pi$ which leads to the so called $n\pi$-ambiguity. To solve this issue, one usually observes the linearly polarized source at at-least three different wavelengths, which removes the $n\pi$-ambiguity.

The RM is related to magnetic field via

$$\mathrm{RM} = 812 \int_{\mathrm{LOS}} \mathrm{n_e B_{\parallel} dl}. \tag{7.2}$$

where RM, the electron density (n_e), the magnetic field $(B_{\parallel})$ component along the line of sight, and the path length (l) are in the units of $\mathrm{rad\,m^{-2}}$, $\mathrm{cm^{-3}}$, $\mu\mathrm{G}$, and pc, respectively. However, the situation becomes complex when multiple emission or rotation screen exist along the line of sight. The angle of Faraday rotation for multiple rotating or emitting screens along the line of sight is characterized by the Faraday depth (ϕ) instead of the RM. Following Burn (1966), Faraday depth is defined as ,

$$\phi = 812 \int_{\mathrm{source}}^{\mathrm{observer}} n_e B_{\parallel} dl. \tag{7.3}$$

In general, for a mixed Faraday rotating and synchrotron emitting medium, the observed polarized intensity originates from a range of Faraday depths.

7.1.1   RM Studies of Galaxy Clusters

Rotation measure studies of galaxy clusters indicate that magnetic field exit on large scales in the ICM (Eilek and Owen, 2002; Pratley et al., 2013; Perley and Taylor, 1991; Feretti et al., 1995; Feretti et al., 1999; Govoni et al., 2017). The Coma cluster has been one of the most important targets for RM studies. A first statistical analysis was performed by (Kim, 1990), who analyzed 18 radio sources and found larger RM in the inner part of the cluster. They reported that the magnetic field is of the order of $\sim 2\,\mu\mathrm{G}$ and a cell size in the range 10-30 kpc. Later on Feretti et al. (1995) found that field is of the oder of $\sim 6\,\mu\mathrm{G}$ with a cell size of ~ 1 kpc. Recently, Bonafede et al. (2013) analyzed the Coma cluster and were able to recover RMs for multiple resolved sources, including the relic. To investigate how well various models of the gas density distribution reproduce the observed RM trends, they used the mean $(<|\mathrm{RM}|>)$ and standard deviation (σ_{RM}) of the RM as a function of radius.

The comparison of the RM maps with the numerical simulations of the magnetic field power spectrum revealed that while some models replicate the distribution in the main body of the Coma cluster, none were able to replicate the trend close to the radio

relic, unless the magnetic field is further amplified in that particular region. Bonafede et al. (2013) also investigated the radial profile and reported that $<|RM|>$ decrease with the distance from the cluster centre, indicating that the magnetic field profile decreases radially. The σ_{RM} profile also decreases with the distance from the cluster centre, suggesting magnetic field fluctuations over a range of spatial scales.

7.2 Depolarization

When the mixture of Faraday depth along the line of sight causes the reduction of the fractional polarization, the source is subjected to depolarization. There are several effects which decrease the fractional polarization of a radio source. These effects could be divided into two categories, instrumental and physical effects. The instrumental effects are of two types: beam and bandwidth depolarization. The observations are performed with a fixed bandwidth and spatial resolution. According to Equation 7.1, the polarization angle rotates as a function of the wavelength. Therefore, within a frequency band, this causes a change in polarization angle from one frequency to the other, causing the bandwidth depolarization. This effect could be minimized by reducing the bandwidth and by using RM-synthesis technique (see Section 7.6). On the other hand, the beam depolarization is caused by the polarized emission with different polarization angles within the telescope beam as the beam smoothens out the polarization with different polarization angles. The only way to correct for the beam depolarization is by observing at a sufficiently high angular resolution.

The physical effects are all wavelength dependent and could be mainly classified into two types:

Internal Faraday dispersion (IFD): Depolarization by the internal Faraday dispersion occurs when the emitting and rotating regions are intermixed and contain a random magnetic field. A random magnetic field produces different amounts of Faraday rotation within the beam and the polarized signal suffers from depolarization if the beam passes through many random directions. For IFD, Burn (1966); Sokoloff et al. (1998) reported that

$$p = p_0 \frac{1 - \exp(-2\lambda^4 \sigma_{RM}^2)}{2\lambda^4 \sigma_{RM}^2}, \tag{7.4}$$

where σ_{RM} is the dispersion in the Rotation measure.

External Faraday dispersion (EFD): Depolarization by the external Faraday dispersion occurs when there is a non-emitting Faraday screen between the observer and

the source of synchrotron emission. For a region that is not emitting synchrotron radiation, the only way to cause depolarization is through a random magnetic field or by varying the magnetic field within the beam. For EFD, Burn (1966); Tribble (1991) reported that

$$p = p_0 \exp(-2\lambda^4 \sigma_{\mathrm{RM}}^2). \tag{7.5}$$

7.3   Toothbrush: previous polarization studies

The WSRT observations revealed that the Toothbrush is highly polarized over its entire length, with a polarization fraction of up to 60 % at 4.9 GHz (van Weeren et al., 2012a). The electric field vectors are mainly perpendicular to the Toothbrush, except at the eastern end of B1. At 4.9 GHz, the polarization fraction across region B1 is between 15 % to 30 %, while for region B2 the polarization fraction is around 50 %. However, at low frequencies (in L-band), the polarization fraction drops significantly, in particular at B1. At 1.38 GHz, the polarization fraction for region B3 is as high as 40 % but for for B1 region it is below 1 %.

Recently, Kierdorf et al. (2016) reported high frequency polarization observations of the Toothbrush, with the Effelsberg 100 m telescope, taken at 4.85 GHz and 8.35 GHz. They found that at 8.35 GHz, the polarization fraction strongly varies across the relic, with 15 % in region B1, a maximum of 45 % in region B2 and 30 % in region B3. At 4.85 GHz, their results, for all three components, are similar to those obtained by van Weeren et al. (2012a).

Kierdorf et al. (2016) also found a significant depolarization for B1 region of the Toothbrush between 8.35 GHz and 1.38 GHz. They reported that the depolarization in region B1 is due to a decrease in electron density and strength of the turbulent magnetic field.

7.4   VLA L-band polarization imaging

After calibrating the VLA data, as described in Section 3.2.1, we produced the Stokes I, Q, U, and V images of the target field. We include data from all configurations, i.e., A , B , C, and D, to create Stokes IQUV images. In order to apply RM-synthesis (see Section 7.6) to our L-band VLA data, we create Stokes IQUV maps of every four neighboring frequency channels to avoid the bandwidth depolarization. Imaging was always done using `robust`=0 weighting. All Q, U and V channelized map were convolved to the same beam size and were corrected for the primary beam attenuation.

We do not find any signal in Stokes V image. This is expected as most of the radio sources only shows linear polarization.

We inspected all Q and U maps to remove the maps affected by RFI. From the Stokes I, Q and U images, we determine the linear polarized intensity ($p = \sqrt{Q^2 + U^2}$), polarization angle ($\psi = 0.5\tan^{-1}\frac{U}{Q}$), and polarization fraction ($m = \frac{\sqrt{(Q^2+U^2)}}{I}$).

7.5 Polarization maps

In Figure 7.1, we show the VLA $1-2$ GHz polarization intensity image of the cluster at different resolutions. Our measurements show that the relic is polarized over its entire length. The fractional polarization changes systematically along the relic. The outer part of the handle (B3) is significantly polarized in L-band. We find that the inner part of the handle (B2) is still polarized in L-band, but significantly less than B3. For region B3 and B2, the average degree of polarization measured from the $35''$ resolution map, are $\sim 14\,\%$ and $\sim 3\%$, respectively. The obtained values are in agreement with those reported by van Weeren et al. (2012a) using the WSRT L-band data. However, the degree of polarization extracted from the $5''$ resolution map for region B3 and B2 are $\sim 26\,\%$ and $\sim 11\,\%$, respectively. This implies that the degree of polarization increases with increasing resolution. At low resolution, regions with different polarization characteristics smoothens the polarization of the source and therefore, the measured polarization is less than the true polarization. This effect will be less if the source is imaged at a higher resolution and our investigation confirms this.

The VLA $1-2$ GHz high resolution polarization intensity image of the Toothbrush with a restoring beam of $2\rlap{.}''25 \times 2\rlap{.}''25$ is shown in Figure 7.2. At such a high resolution the relic is also polarized over its entire length. The polarized intensity is patchy and follows the filamentary structure seen in the total intensity images. The polarization fraction across the Toothbrush varies strongly between $2\,\%$ and $60\,\%$, where it can be measured, see Figure 7.3.

At such a high resolution, our measurement shows that region B3 is highly polarized at $1-2$ GHz, as high as $60\,\%$. The average value of the polarization fraction across the whole B3 region is about $26\,\%$. Interestingly, the arc-shaped filament, labelled as F1, is the only region within B3 where the polarization fraction is less than $\sim 6\,\%$.

At B2 region, the polarization fraction is mostly between $5\,\%$ to $25\,\%$ and varies significantly. The maximum polarization fraction is measured across the northern edge of
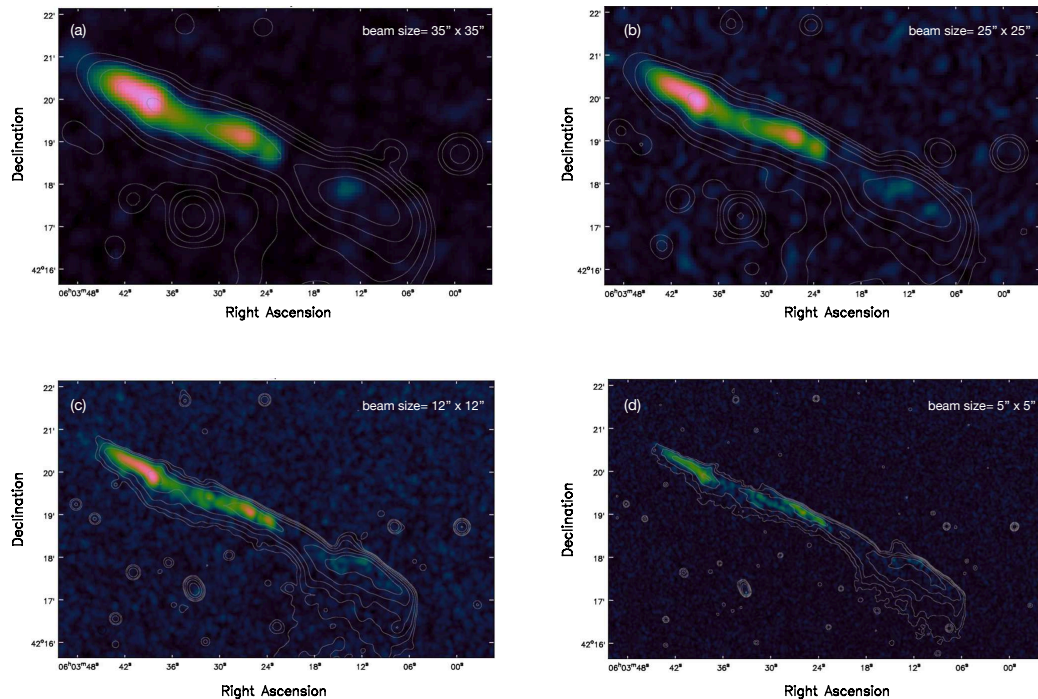
Figure 7.1: VLA $1-2\,$GHz polarization images of the Toothbrush at different resolutions. These images were made by combining A, B, C, and D configuration data, using robust weighting, and tapered to different resolutions. *Top*: panel (a) at $35'' \times 35''$ where $\sigma_{\mathrm{rms}} = 32\,\mu$Jy beam^{-1} and panel (b) at $25'' \times 25''$ where $\sigma_{\mathrm{rms}} = 26\,\mu$Jy beam^{-1}. *Bottom*: panel (c) at $12'' \times 12''$where $\sigma_{\mathrm{rms}} = 14\,\mu$Jy beam^{-1} and panel (d) at $5'' \times 5''$ where $\sigma_{\mathrm{rms}} = 8\,\mu$Jy beam^{-1}. In all images, contour levels are drawn at $[1,\,2,\,4,\,8,\,\ldots] \times 4\,\sigma_{\mathrm{rms}}$ and are from the Stokes I image.
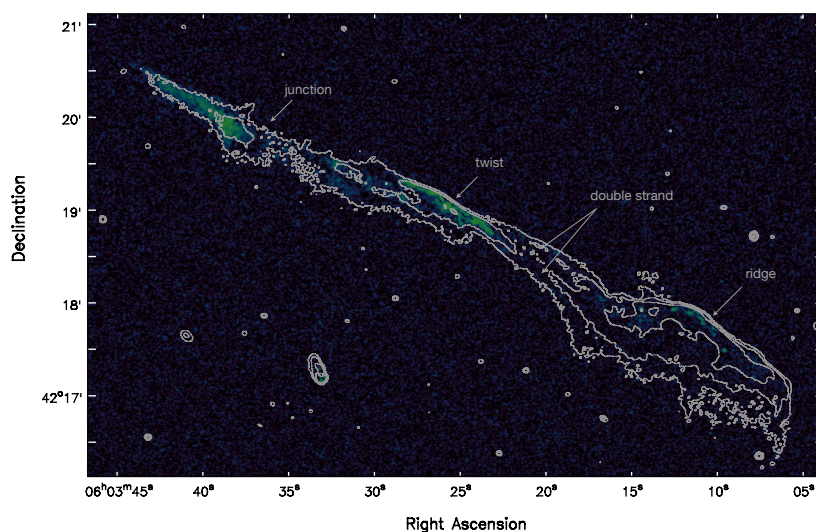
Figure 7.2: High resolution $1-2\,$GHz VLA polarization intensity image of the Toothbrush. The image has a resolution of $2''\!25 \times 2''\!25$. The contour levels are drawn at $[1, 2, 4, 8, \ldots] \times 4.5\,\sigma_{\mathrm{rms}}$, where $\sigma_{\mathrm{rms}} = 6\,\mu$Jy beam^{-1} and are from the Stokes I image.
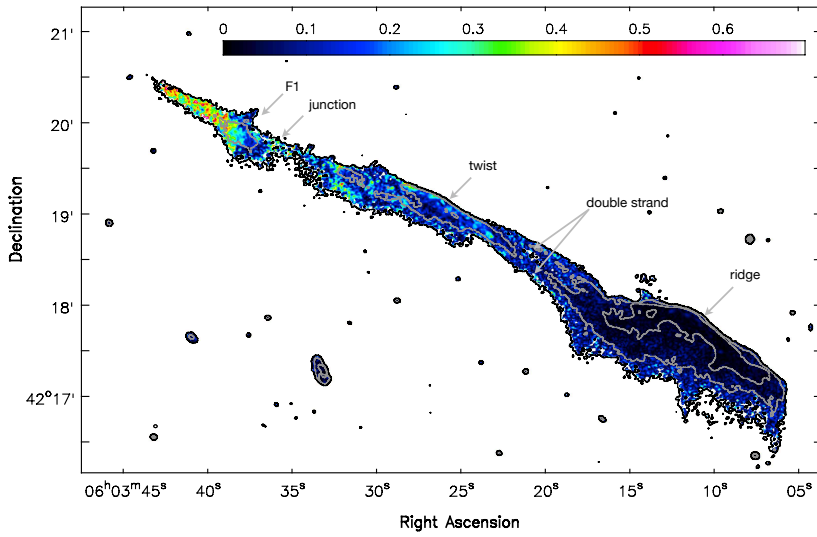
Figure 7.3: VLA $1-2\,$GHz polarization fraction image of the Toothbrush. The image has a resolution of $2''\!.25 \times 2''\!.25$. The contour levels are drawn at $[1, 2, 4, 8, \dots] \times 4.5\,\sigma_{\mathrm{rms}}$, where $\sigma_{\mathrm{rms}} = 6\,\mu\mathrm{Jy\,beam}^{-1}$ and are from the Stokes I image.

the twist region, see Figure 7.3. In the double strand, we find that the northern strand is moderately polarized while the southern is unpolarized.

In the total intensity image of the Toothrush several strands are visible to the east of the B2 region, see Figure 4.3. In the polarized intensity image these strands are easily distinguishable (Figure 7.1 panel d and Figure 7.3). At B1 region, the degree of polarization drops below $3\,\%$. However, the northern edge of the ridge is slightly polarized, see Figure 7.2.

7.6 RM Synthesis

The Rotation Measure Synthesis Technique (RM-synthesis) was first developed by Brentjens and de Bruyn (2005) to recover the extended polarized emission in the Perseus cluster. The technique is based on the theoretical description of Burn, 1966.

According to the Burn (1966), the polarization (P) can be written as a complex vector

$$P(\lambda^2) = \int_{-\infty}^{\infty} mI \exp(2\mathrm{i}[\psi_{\mathrm{int}} + \phi\,\lambda^2])\mathrm{d}\phi, \tag{7.6}$$

where m is the fractional polarization. By introducing a function, $F(\phi)$, in Equation 7.7, we get

$$P(\lambda^2) = \int_{-\infty}^{\infty} F(\phi) \exp(2\mathrm{i}\phi\,\lambda^2])\mathrm{d}\phi. \tag{7.7}$$

In Equation 7.7, $F(\phi)$ is known as the Faraday dispersion (FD) function. The FD distribution describes the amount of polarized flux density that has undergone a certain amount of Faraday rotation at a certain Faraday depth. If the intrinsic polarization angle (ψ_{int}) is constant as a function of λ, then $F(\phi)$ can be measured as

$$F(\phi) = \int_{-\infty}^{\infty} P(\lambda^2) \exp(-2\mathrm{i}\phi\,\lambda^2]) \mathrm{d}\lambda^2. \tag{7.8}$$

According to Brentjens and de Bruyn (2005), the reconstructed Faraday spectrum can be written as:

$$\tilde{F}(\phi) = \int_{-\infty}^{\infty} \tilde{P}(\lambda^2) \exp(-2\mathrm{i}\phi[\lambda^2 - \lambda_0^2]) \mathrm{d}\lambda^2 = \mathrm{F}(\phi) \star \mathrm{R}(\phi), \tag{7.9}$$

where $R(\phi)$ is known as the Rotation Measure Spread Function (RMSF) and is defined as:

$$R(\phi) = K \sum_{i=1}^{N} W(\lambda_i^2) \exp(-2\mathrm{i}\phi[\lambda_{\mathrm{i}}^2 - \lambda_0^2]), \tag{7.10}$$

$$K = \left(\sum_{i=1}^{N} W(\lambda_i^2) \right)^{-1}, \tag{7.11}$$

where $W(\lambda_i^2)$ is the sampling function and represent the bandwidth of the telescope data. Therefore, applying RM-synthesis to the channelized Stokes QU data leads to a data cube, whose third axis determines the Faraday depth. Since the finite frequency band produces an RMSF with sidelobes, the deconvolution might be necessary and is done with the deconvolution algorithm called `RM CLEAN` (Heald, 2009)

The RM spectra of the Toothbrush have been little studied so far. van Weeren et al. (2012a) found a peak RM value for the B3 region of $+10\,\mathrm{rad\,m^{-2}}$ and a significant RM gradient for the B2 region. Kierdorf et al. (2016) found a significant RM gradient across the entire relic and suggested that it is caused by an intergalactic foreground magnetic field. However, the RMs derived in these observations could be affected by averaging over significant local variations. Hence, a significantly better spatial resolution, higher sensitivity, and wide frequency coverage is required to shed light on the magnetic field and Faraday structure of the polarized Toothbrush emission.

We performed a RM-Synthesis on the VLA data using cubes of the Stokes Q and U images, with a resolution of $12'' \times 12''$. The RM-synthesis cube synthesizes a range of Faraday depths from $-1200\,\mathrm{rad\,m^{-2}}$ to $+1200\,\mathrm{rad\,m^{-2}}$, with a step size of $2\,\mathrm{rad\,m^{-2}}$. Since the maximum sensitivity is desired for this, we use the entire wide-band $1-2\,\mathrm{GHz}$ GHz data. These data give a sensitivity to the polarized emission up to a maximum

observable Faraday depth ($\phi_{\max}$) and the resolution in faraday depth ($\delta\phi$) equal to

$$
\begin{aligned}
\mid \phi_{max} \mid &\approx \frac{\sqrt{3}}{\delta\lambda^2} \approx 1.9 \times 10^5 \mathrm{rad\,m}^2, \\
\delta\phi &\approx \frac{2\sqrt{3}}{\Delta\lambda^2} = 58\,\mathrm{rad\,m}^{-2},
\end{aligned}
\tag{7.12}
$$

where, $\Delta\lambda^2 = \lambda_{\max}^2 - \lambda_{\min}^2$.
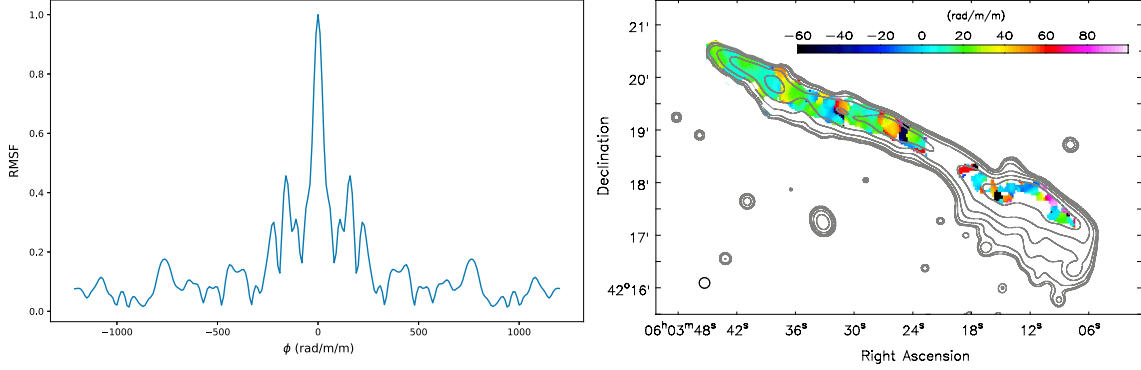
Figure 7.4: *Left*:Rotation measure spread function (MSF) from the $1-2$ GHz VLA data. The FWHM of the RMSF is 58 rad m^{-2}.*Right*: Rotation Measure map of the Toothbrush at $1-2$ GHz. The image has a resolution of $12'' \times 12''$. The contour levels are drawn at $[1, 2, 4, 8, \ldots] \times 4.5\,\sigma_{\mathrm{rms}}$, where $\sigma_{\mathrm{rms}} = 14\,\mu\mathrm{Jy\,beam}^{-1}$.

The RMSF is shown in Figure 7.4 left panel. The first sidelobe of the RMSF is about 40 %. Therefore, in order to remove the sidelobes, we use `RM CLEAN` algorithm (Heald, 2009), cleaning down to 5σ level of the Q and U cubes.

In Figure 7.4 right panel, we show the Rotation Measure map (or Faraday map). The map basically represents the distribution of the peak of $|\tilde{F}(\phi)|$. For the Toothbrush, ϕ_{peak} vary spatially from about -60 to $+110$ rad m^{-2}, which is larger than what was report by van Weeren et al. (2012a), i.e., -53 to $+55\,\mathrm{rad\,m}^{-2}$. The galactic Rotation Measure at the location of 1RXS J0603.3+4214 is about 11.7 ± 4 rad m^{-2}. For region B3, ϕ_{peak} is between $+8\,\mathrm{rad\,m}^{-2}$ to $+53\,\mathrm{rad\,m}^{-2}$. The mean RM is close to the galactic foreground, however, some regions with a distinct morphology, for instance F1, show a shift in the RM.

For region B2, we find a strong gradient from -56 to $+60$ rad m^{-2}. For region B1, we also find a strong gradient between -54 to $+110$ rad m^{-2}. The peak in the Faraday depth ($\phi_{\max}$) for regions B2 and B1, deviates from the average galactic foreground, indicating that the most of the Faraday rotation in these regions is probably caused by the ICM.

7.6.1   Faraday spectra

Our new VLA wideband data allow a detailed investigation of single or multiple RM components, either along the line of sight or intrinsic to the source itself using the RM-synthesis technique. In this section, we show the results obtained from the RM-synthesis for two of the components of the Toothbrush, namely B2 and B3.

7.6.1.1   B3 region

The Faraday spectra of region B3 is shown in Figure 7.5 left panel. For B3, we find multiple peaks in the Faraday spectra, extracted from the clean components.
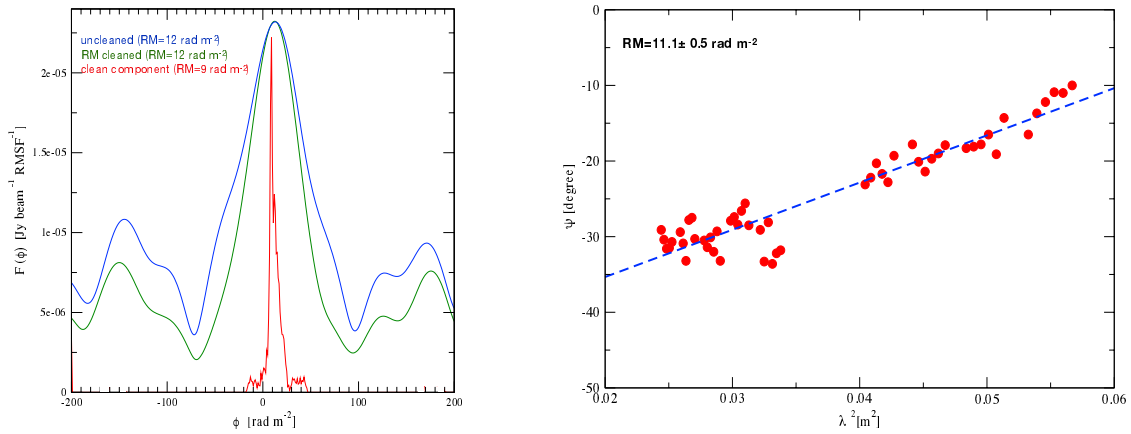
Figure 7.5: *Left*: Faraday spectrum of B3 region extracted from the uncleaned (blue), `RM-CLEAN` (green) and the clean component (red) Faraday cube. *Right*: polarization angle vs. λ^2 for region B3. The dashed line is a linear fit. The Rotation Measure (RM) obtained from the linear fit 11.1 ± 0.5 rad m^2.

The dominant peak is found at about $+9 \, \mathrm{rad \, m^{-2}}$, while the second and third peaks are found at $+12 \, \mathrm{rad \, m^{-2}}$ and $+19 \, \mathrm{rad \, m^{-2}}$, respectively. The ϕ_{peak} for region B3 is very close to the average galactic foreground value, indicating that it does not pass deep into the ICM. The deep Chandra observation confirms the same that, region B3 extends into a region where the ICM is not so dense.

For the entire B3 region, we also derive the RM value using the RM-fit method (Equation 7.1). The resultant plot is shown in Figure 7.5 right panel. A linear fit to the data gives a RM of $+11.1 \pm 0.5 \, \mathrm{rad \, m^{-2}}$, which is consistent with the one obtained from the RM-synthesis technique.

We investigate how the ϕ_{peak} varies within the B3 region with distance increasing from the west to east. To extract the ϕ_{peak}, we created square shaped boxes as shown in Figure 7.6 right panel. The resultant plot is shown in Figure 7.6 left panel. The western end of region B3, i.e., arc-shaped filament (F1), shows a high value of ϕ_{peak}, namely
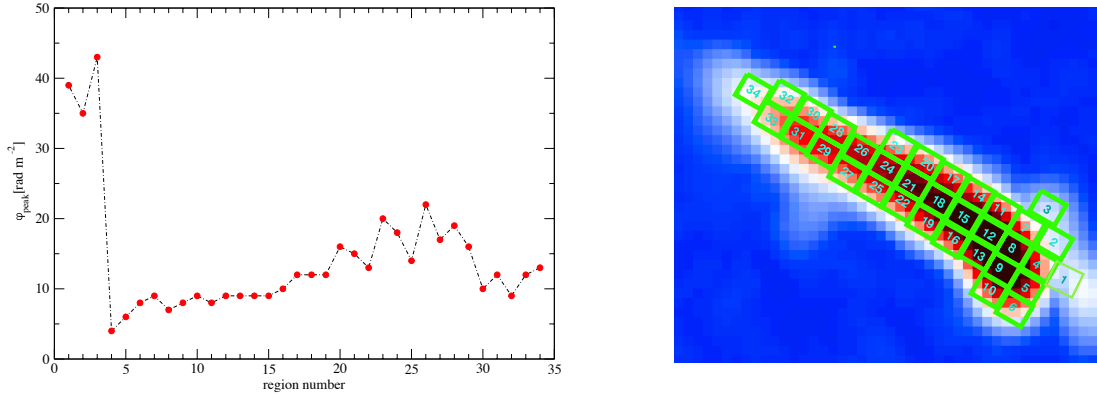
Figure 7.6: *Left*: RM variation across B3 region of the Toothbrush with respect to the distance when moving from west to east. *Right*: Regions used to extract the Faraday spectra at different positions across region B3.

$+40 \, \mathrm{rad \, m^{-2}}$. After that the ϕ_{peak} remains more or less constant, i.e., $+9 \, \mathrm{rad \, m^{-2}}$. At the eastern part of the region B3, ϕ_{peak} is between $+12 \, \mathrm{rad \, m^{-2}}$ to $+19 \, \mathrm{rad \, m^{-2}}$. We notice that the high value of ϕ_{peak} corresponds to the filamentary structures visible within the B3 region.

Figure 7.7: *Left*: VLA $1-2 \, \mathrm{GHz}$ polarization B-vector map of region B3. The total polarized intensity is shown in color scale. The vectors depict the polarization B-vectors. The image has a resolution of $2''\!.25 \times 2''\!.25$. The contour levels are drawn at $[1, 2, 4, 8, \dots] \times 4.5 \, \sigma_{\mathrm{rms}}$, where $\sigma_{\mathrm{rms}} = 6 \, \mu \mathrm{Jy \, beam^{-1}}$ and are from the Stokes I image. The vectors are corrected for the effects of Faraday rotation. The length of B-vectors is same and does not represent the polarization fraction. *Right*: Depolarization of the B3 and B2 component.

The distribution of the magnetic field vectors for region B3 after correcting for Faraday rotation is shown in Figure 7.7 left panel. The B-vectors are more or less parallel to the relic extension.

The fractional polarization in B3 region of the Toothbrush decreases only moderately towards longer wavelengths, see Figure 7.7 right panel. The polarization fraction across region B3 decreases from about 30 % to about 18 % with increasing wavelength. Moreover, we find that the depolarization found in B3 region does not agree with the

IFD or EFD. The polarization fraction across the B3 region decreases from about 21 %
to about 8 % with increasing wavelength.

7.6.1.2   B2 region

The Faraday spectra of region B2 shows a complicated FD distribution. It has been
reported that the RM distribution across B2 region shows a strong RM gradient from
east to west, namely $-10\,\mathrm{rad\,m^{-2}}$ to $+55\,\mathrm{rad\,m^{-2}}$ (van Weeren et al., 2012a). Our VLA
L-band data shows a dominant peak at about $+19\,\mathrm{rad\,m^{-2}}$ plus several other fainter
peaks, see Figure 7.8 left panel. The ϕ_{peak} for region B2 deviates from the galactic
foreground value, indicating that it is located deeper into the ICM. The average RM
is about $+19\,\mathrm{rad\,m^{-2}}$ for the B2 region. However, we find that distinct filamentary
structures in the B2 regions show a large shifts in the RM, about $50\,\mathrm{rad\,m^2}$.
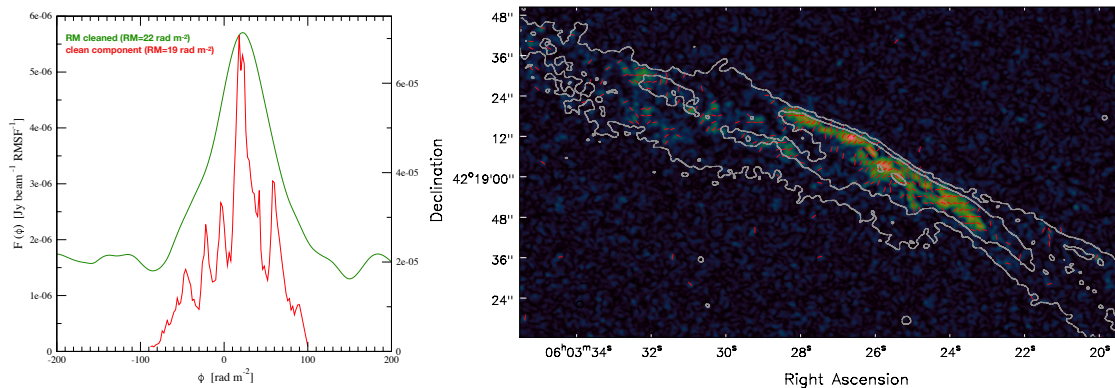
Figure 7.8: *Left*: Faraday spectrum of B2 region extracted from the `RM CLEAN` (green) and the clean
component (red) Faraday cube. *Right*: VLA $1-2\,\mathrm{GHz}$ polarization B-vector map of region B2. The
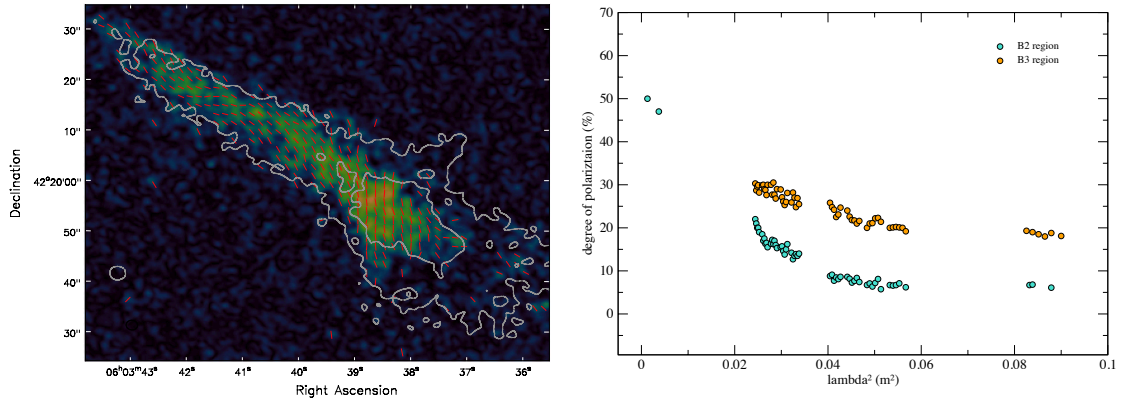total polarized intensity is shown in color scale. The vectors depict the polarization B-vectors. The
image has a resolution of $2\overset{''}{.}25 \times 2\overset{''}{.}25$. The contour levels are drawn at $[1, 2, 4, 8, \dots] \times 4.5\,\sigma_{\mathrm{rms}}$, where
$\sigma_{\mathrm{rms}} = 6\,\mu\mathrm{Jy\,beam^{-1}}$ and are from the Stokes I image. The vectors are corrected for the effects of
Faraday rotation. The length of B-vectors is same and does not represent the polarization fraction.

The distribution of B-field vectors for region B2 after correcting for Faraday rotation
is shown in Figure 7.8 right panel. In contract to the region B3, the orientations of
the B-vectors changes across the B2 region.

7.7   Summary

We presented the VLA $1-2\,\mathrm{GHz}$ polarization maps of the Toothbrush. The main
results are:

1. The Toothbrush is polarized over its entire length in the VLA L-band. The polarization intensity appears patchy and show some filamentary structures, as seen in the total intensity image.

2. We find that region B3 is strongly polarized, as high as 60%. The degree of polarization across the Toothbrush decreases from B3 to B1 region. For B1, the polarization fraction drops below 3%.

3. The degree of polarization depends on the image resolution. We find that the polarization fraction increases with increase in the image resoltuion.

4. The Faraday depth value for region B3 is close the average galactic foreground, namely $+9$ rad m^{-2}. At the arc-shaped filaments, labelled as F1, the polarization fraction drops significantly. We find that the RM value across the arc-shaped filament is high, namely $+40$ rad m^{-2}, as compared to the rest of the areas within B3. We find that the fractional polarization of the B3 region decreases only moderately towards longer wavelength within the L-band.

5. The Faraday depth value of the B2 and B1 regions deviates from the average galactic foreground, indicating that B1 and B2 are located deeper into the ICM of the cluster. We find that the RM value varies strongly across the region B2 and B1.

6. The filamentary features in the low density region (B3) show a shift in RM of about $+30\,\mathrm{rad\,m^{-2}}$. In denser regions (B2) the shifts increases to values of about $+50\,\mathrm{rad\,m^{-2}}$.

7. The brush region of the Toothbrush depolarizes at $1-2\,\mathrm{GHz}$, suggesting that it is located in a region that a significant amount of ICM lies in front and thus, depolarizes the emission.

Chapter 8

A radio relic in CIZA J0649.3+1801

8.1 CIZA J0649.3+1801

The galaxy cluster CIZA J0649.3+1801 is located at a redshift of z = 0.064 and a galactic latitude of $b = 7.66°$. The cluster was first discovered by Ebeling et al. (2002). Together with seven other clusters, it forms part of a supercluster in the Zone of Avoidance (ZOV) near the galactic anti-center and is hidden by our galaxy, the Milky Way. This association is the most notable concentration of clusters in the CIZA cluster sample (Kocevski et al., 2007).

CIZA J0649.3+1801 is a very little studied galaxy cluster. It has a moderate X-ray luminosity of $L_{X,0.1-2.4\,keV} = 2.34 \times 10^{44} erg\,s^{-1}$. In the radio band, the cluster was observed at 610 MHz with the GMRT (van Weeren et al., 2011). A diffuse elongated radio source has been found at the periphery of this cluster with no obvious optical counterpart and has been tentatively classified as a relic. Only a few relics has been found so far at low galactic latitudes because extragalactic objects are difficult to identify in this region of the sky (see Kraan-Korteweg and Lahav, 2000, for a review). Since CIZA J0649+18 is located in the ZOV, studying the radio emission is difficult, in particular the polarization of the objects as galactic foreground strongly affects the polarization properties of any extragalactic source.

8.2 WSRT observations of CIZA J0649.3+1801

The cluster was observed with the WSRT at three different frequencies, namely 1.23 GHz, 1.39 GHz, and 1.71 GHz (PI R. J. van Weeren). The maxi-short configuration was used with the pointing of the telescope at the centre of the cluster. The L-band WSRT observations are summarized in Table 8.1. The WSRT data gives a total integration time of about 34 hrs on the target field. A total bandwidth of 160 MHz was recorded, spread over eight spectral windows, each divided into 64 channels. All four circular polarization products were recorded. For each night, the two calibrators, i.e., 3C48 and 3C286, were observed for 30 minutes, immediately before and after the target observation.

Table 8.1: WSRT L-band observations overview

Wavelength	18 cm	21 cm	25 cm
Frequency range	1660-1786 MHz	1321-1460 MHz	1170-1289 MHz
Telescope configuration	maxi-short	maxi-short	maxi-short
Number of IFs	8	8	8
Bandwidth per IF	20 MHz	20 MHz	20 MHz
No. of channels per IF	64	64	64
Polarization	all Stokes	all Stokes	all Stokes
Observation dates	Dec 16, 2010	Dec 24, 2010	Dec 26, 2010
Total on-source time	12hr	12hr	12hr
Flux calibrator	3C48	3C48	3C48
Polarization calibrator	3C286	3C286	3C286
Dead antennas	RT5, RT3 , RTD	RT5	RT5, RT4

8.2.1   Data reduction: calibration

The data were calibrated and reduced with the `CASA` package (McMullin et al., 2007), version 4.7.0. The data from three different nights were independently calibrated. As a first step in the data reduction, we manually flagged some of the time ranges affected by the shadowing effect. After this, we determined and applied the system temperature (T_{sys}) correction. As a next step, the data were then inspected for RFI removal. The software `AOFlagger` (Offringa et al., 2010) was used for removing RFI. Due to the strong RFI at 18 cm observations, a total of about 50% data were flagged (including dead antennas i.e., RT5, RT4, and RTD, and those affected by the shadowing). For the 21 cm and 25 cm observations about 30% data were flagged in total.

We used the L-band 3C48 and 3C286 model provided by the `CASA` software, and set the fluxes of the calibrator source according to the Perley-Butler 2013. The initial phase solutions were obtained for each spectral windows and were subsequently used to correct for the parallel-hand delays. We flagged the edge channels from each sub-band because of the roll-off of the bandpass. Therefore, the data set contains 50 channels per spectral windows. The bandpass response were determined using the calibrator 3C48. After the bandpass calibration, we performed the gain calibration for both the calibrators.

The L-band receivers of the WSRT antennas have linearly polarized feeds[1]. For polarization calibration, the data were first calibrated for the leakage terms (D-terms) using the unpolarized calibrator 3C48, while the polarization angle correction and the cross-hand delays were determined using the polarized calibrator 3C286. In the end, all the calibration solutions were applied to the target data. The data were then averaged by a factor of 5 in frequency (i.e., five channels per spectral windows).

---

[1]https://www.astron.nl/radio-observatory/astronomers/analysis-wsrt-data/analysis-wsrt-data

.

Table 8.2: Imaging parameter

Wavelength	18 cm	21 cm	25 cm	combined	GMRT
beam size	$75'' \times 60''$	$75'' \times 60''$	$75'' \times 60''$	$63'' \times 25''$	$65'' \times 65''$
weighting	Briggs	Briggs	Briggs	Briggs	Briggs
robust	0.5	0.5	0.5	0.5	0.5
RMS noise	47 μJy	53 μJy	58 μJy	50 μJy	540 μJy

8.2.2   Self-calibration and imaging

After initial imaging of the target field, we ran several rounds of phase only self-calibration, followed by two final round of amplitude-phase calibration. Imaging was always performed using the clean masks. To take into account the spectral behavior of the bright sources, we imaged each band using `nterms = 2`. The Stokes I image was created per band using all spectral windows. The images were produced using the `Briggs` weighting with `robust` parameter of 0.5. We subtracted two bright sources from the uv-data because these two sources were surrounded by rings. However, the source subtraction reduced the rings around them and improved the image quality.

Finally, the data from 18 cm, 21 cm and 25 cm band were combined to create a single deep Stokes I image using `nterms = 2`. The final images were corrected for the primary beam attenuation. The polarization intensity, polarization angle and fractional polarization images were derived from the Stokes I, Q and U images.

8.3   WSRT radio continuum image

The resultant L-band WSRT total intensity image of CIZA J0649.3+1801 field after combining the 18 cm, 21 cm and 25 cm data is shown in Figure 8.1. The diffuse elongated structure is clearly detected in our WSRT image, labelled as 'Relic'. The discrete radio sources embedded within the relic are labelled as A, B and C. The properties of the diffuse radio emission are summarized in Tabel 8.3.

In the WSRT image, the surface brightness across the relic is non-uniform and it appears patchy, in particular the northern end. The relic is bright in the central region but fades at the northern and southern corner.
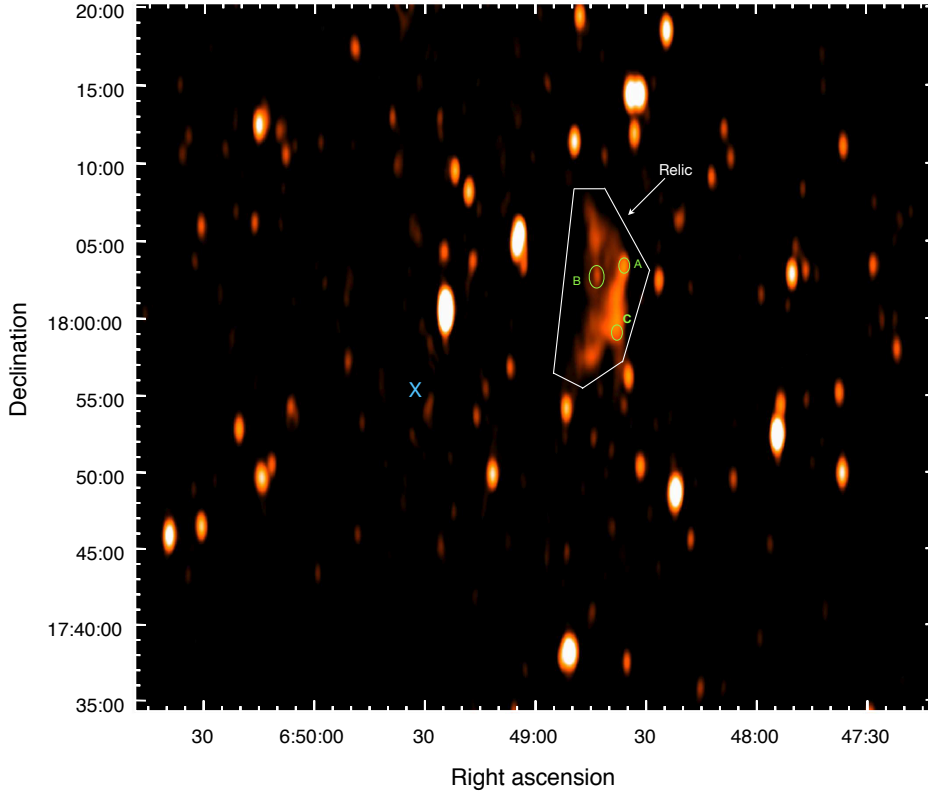
Figure 8.1: CIZA J0649.3+1801 total intensity image after combining the WSRT 18 cm , 21 cm and 25 cm data. The restoring beam is $63'' \times 25''$. Image is created using `Briggs` weighting with `robust` $= 0.5$ and has a noise level of $50\,\mu Jy$ beam^{-1}.

Table 8.3: Flux density measurements and properties of the diffuse radio emission in CIZA J0649+1801

frequency	total flux density	polarized flux density	α_{610}^{1470}	LLS	$\mathcal{M}$
MHz	mJy	mJy		kpc	
1468†	27.1 ± 2.7	4.7 ± 0.5	-1.30 ± 0.04	930	$2.8^{+0.1}_{-0.2}$

† flux measured after combining all WSRT data

Figure 8.2: The total intensity image of the relic in CIZA J0649.3+1801 at three different frequencies. *left*: at 1.2 GHz, *middle*: at 1.4 GHz, *right*: at 1.7 GHz. Contours are drawn at levels of $[1, 2, 4, \ldots] \times 4.5\,\sigma_{\rm rms}$. The rms values are mentioned in Table 8.2.

We also created the total intensity maps at three different wavelengths, namely 25 cm, 21 cm and 18 cm map, see Figure 8.2. The relic is detected in all three WSRT observations. However, we notice that the morphology of the total power emission depends on the observing frequency.
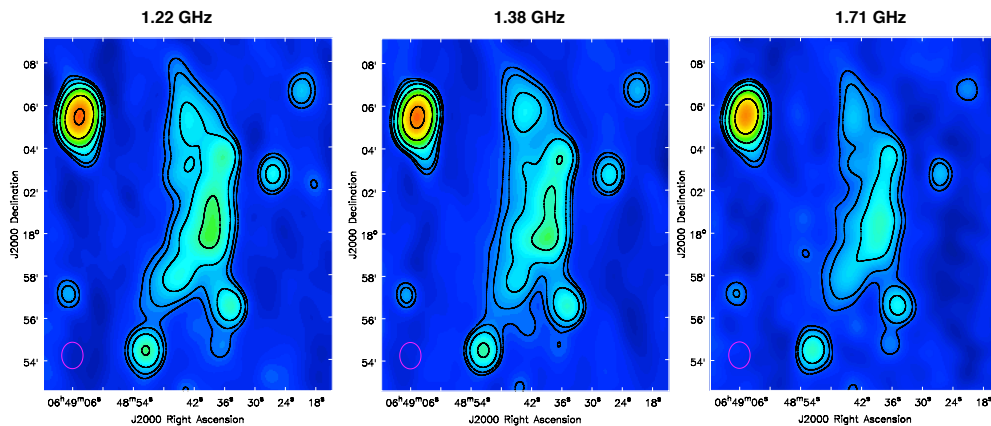
8.3.1 Morphological comparison: WSRT and GMRT

The morphology of the relic in the WSRT image is more or less similar to the GMRT 610 MHz image, see Figure 8.3 for comparison. At 1.48 GHz the relic is more extended. In the WSRT images, it has a total angular extent of about 12.5′ corresponding to a physical size of about 930 kpc, while in the GMRT 610 MHz it is about 800 kpc.

We notice that in the GMRT 610 MHz image the relic is more extended towards the south-east (SE). In contract, the north-east (NE) part of the relic is more extended in the WSRT image. However, at both frequencies, i.e. 610 MHz and 1.47 GHz, the central region of the relic appears brighter.
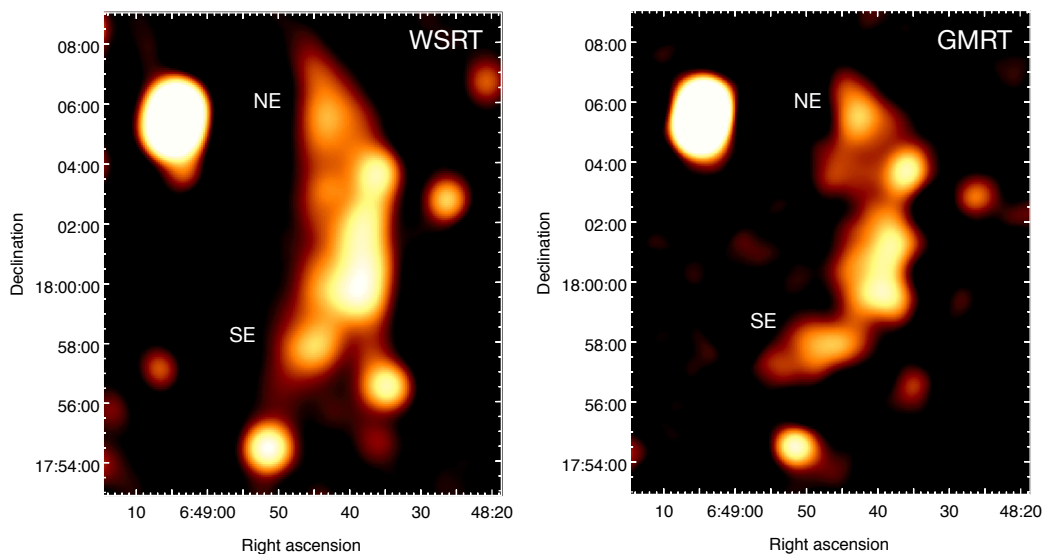
Figure 8.3: A comparison of the radio relic in CIZA J0649.3+1801 between 1.4 GHz and 610 MHz. *Left*: relic emission at 1.4 GHz. Contours are from the WSRT image and are drawn at levels of $[1, 2, 4, \ldots] \times 4.5\,\sigma_{\mathrm{rms}}$, where $\sigma_{\mathrm{rms}} = 50\,\mu\mathrm{Jy}$ beam^{-1}. *Right*: relic emission at 610 MHz. Contours are from the WSRT image and are drawn at levels of $[1, 2, 4, \ldots] \times 4.5\,\sigma_{\mathrm{rms}}$, where $\sigma_{\mathrm{rms}} = 540\,\mu\mathrm{Jy}$ beam^{-1}.

8.4 Integrated radio spectra

To obtain the integrated spectral index of the relic, we create the radio maps at 1713 MHz, 1381 MHz, 1220 MHz, and 610 MHz. To ensures that 'resolving out' large-scale flux distribution has a similar effect on both the GMRT and WSRT data, we apply

an inner uv cut of $0.2\,\mathrm{k}\lambda$ to the GMRT to match the scale of the WSRT data. Here, $0.2\,\lambda$ is the minimum uv-distance in the GMRT data. For imaging, we use `robust`=0.5 and allow for spectral slopes (`nterms` = 2). The GMRT and WSRT images were then convolved to the same beam size, i.e. $65'' \times 65''$.

We assume an absolute flux calibration uncertainty of 10% for the WSRT and GMRT data. For any flux density measurement, we estimate the uncertainty via

$$\Delta S = \sqrt{(0.10S)^2 + N_{\mathrm{beams}}\ (\sigma_{\mathrm{rms}})^2} \tag{8.1}$$

where S is the flux density, σ_{rms} is the RMS noise and N_{beams} is the number of beams.

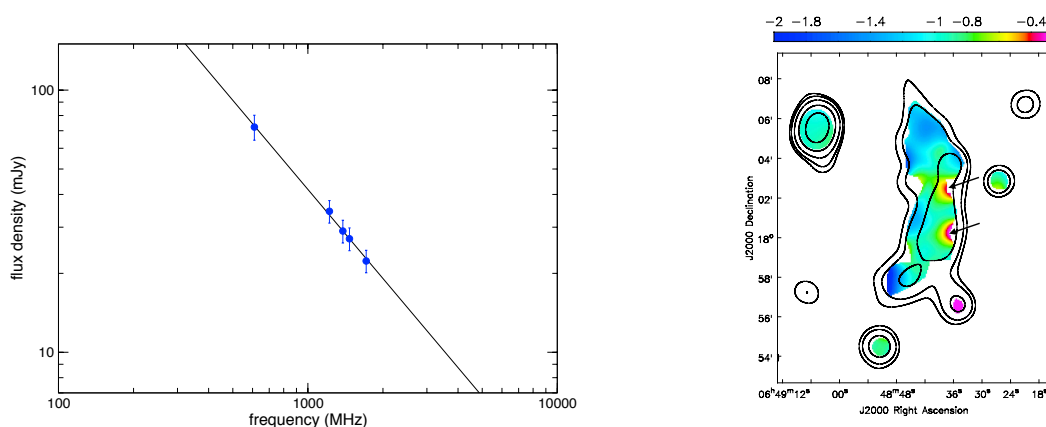
Figure 8.4: *Left*: Integrated spectral index map of the relic in CIZA J0649.3+1801 for 610 MHz to 1.7 GHz. The region where the flux densities are extracted is shown with a red box in Figure 8.1. *Right*: Spectral index map of the relic in CIZA J0649.3+1801 between 1.4 GHz and 610 MHz. Contours are drawn at levels of $[1, 2, 4, \dots] \times 4.0\,\sigma_{\mathrm{rms}}$, where $\sigma_{\mathrm{rms}} = 540\,\mu\mathrm{Jy}$ beam^{-1} and are from the GMRT 610 MHz image.

The total flux densities were extracted in a region where the radio brightness was above the $4\,\sigma$ level and using the same area at all observed frequencies, see Figure 8.1 for the region. The measured flux density of the relic at different frequencies are reported in Table 8.3. Due to the poor resolution of the WSRT, it is not possible to properly take into account the flux of the compact sources, embedded with the relic. Therefore, we extract the flux over the entire relic. However, the flux contribution from these point sources is very small, indicating that the dominant contributor to the flux density is the relic.

The integrated spectral index of the relic obtained by combining our flux density measurements at 1713 MHz, 1470 MHz, 1381 MHz, 1220 MHz, and 610 MHz is shown in Figure 8.4. We find a spectral index of 1.30 ± 0.04 for the relic which is typical for most of the known relics. The spectrum is fitted well by a single power law without any break in this frequency range. From the integrated spectral index, we derive a Mach number of $\mathcal{M} = 2.8^{+0.1}_{-0.2}$.

8.5 Spectral index map

To create the spectral index map of the relic, we use the WSRT and GMRT images mentioned in Section 8.4. Pixels with a flux density below $4\,\sigma_{\mathrm{rms}}$ in either image were blanked. The $65''$ resolution spectral index map of the relic between 610 MHz and 1.47 GHz is shown in Figure 2.2.

The spectral index across the relic varies roughly between -0.78 to -2.0, excluding the two regions with somewhat flatter spectra located at the western edge of the relic. A clear spectral index steepening towards the cluster centre is visible, i.e., from west to east. From spectral index map, we obtain a Mach number of $\mathcal{M} = 2.8^{+0.3}_{-0.2}$ which agrees to the one derived from the overall spectrum.

Table 8.4: Total intensity and polarization flux density measurements of the diffuse radio emission in CIZA J0649+1801

frequency	total flux density	polarized flux density
MHz	mJy	mJy
1713	22.3 ± 2.2	4.9 ± 0.5
1381	29.0 ± 2.9	4.7 ± 0.5
1220	34.5 ± 3.4	4.2 ± 0.5
610	82.3 ± 7.9	-

8.6 Polarization maps

To study the polarization properties of the diffuse source, we create Stokes I, Q, and U images. Our polarization images revels that the relic is highly polarized, as high as 40%-45%, see Figure 8.5. The polarization fraction across the relic varies between $5\,\%$ and $45\,\%$, where it can be measured. The WSRT observations also shows a decrease in the polarization fraction towards the lower frequencies, as has been seen for very well studied radio relics, e.g., in A2256 (Brentjens, 2008), A2255 (Pizzo et al., 2011) and 1RXS J0603.3+4214 (van Weeren et al., 2012b).

The mean value of the polarization fraction at 1.7 GHz, 1.4 GHz and 1.2 GHz are $22\,\%$, $16\,\%$ and $12\,\%$, respectively (see Table 8.4).

8.7 Summary

We reported the WSRT observations of the galaxy cluster CIZA J0649.3+1801. These observations were conducted at three different frequencies, namely at 1713 MHz, 1381 MHz,
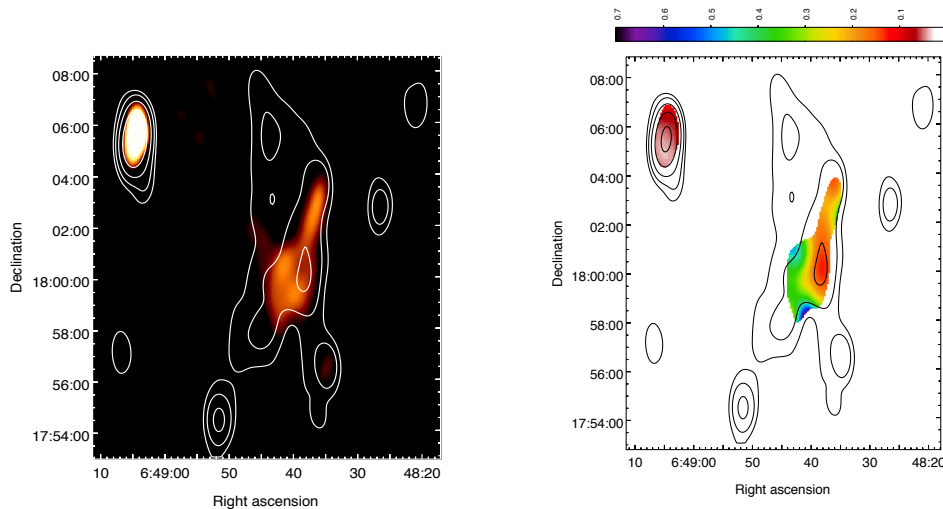
Figure 8.5: WSRT 1.4 GHz polarization maps of the radio relic in CIZA J0649.3+1801. *Left*: polarization intensity image overlaid with the total intensity contours. *Right*: polarization fraction across the relic overlaid with the total intensity contours. In both the images, contours are drawn at levels of $[1, 2, 4, \ldots] \times 4.5 \, \sigma_{\mathrm{rms}}$, where $\sigma_{\mathrm{rms}} = 50 \, \mu\mathrm{Jy} \, \mathrm{beam}^{-1}$.

and 1220 MHz. These observations were aimed to investigate the polarization properties of the diffuse emission detected in the cluster. The main results are:

1. We classified the diffuse emission in CIZA J0649.3+1801 as a radio relic.

2. The relic has an integrated spectral index of -1.30 ± 0.04. The spectral index map between 610 MHz and 1.48 GHz shows a hint of spectral gradient towards the cluster center.

3. The Mach number obtained from the overall spectrum agrees well to the one obtained from the spectral index map, namely $\mathcal{M} = 2.8^{+0.1}_{-0.2}$.

4. The multi-frequency WSRT observations reveal that the relic is highly polarized, as high as 45%, with a mean polarization of $\sim 17\%$ at 1.48 GHz.

Conclusions

In this thesis we aim at improving our knowledge of the origin of diffuse radio emission in galaxy clusters through interferometric radio observations. The presence of diffuse synchrotron emission in galaxy clusters, like relics, halos, and mini-halos, plays a fundamental role in understanding the particle acceleration mechanisms and magnetic field properties. The particle acceleration mechanisms which explain the presence of a large population of relativistic electrons in clusters is debated.

Radio relics are important probes of particle acceleration and magnetic fields at the cluster outskirts. Relics are related to ongoing merger events and their association with the merger driven shocks is now well established. Cosmological shocks are capable of accelerating particles and amplifying magnetic fields. In this thesis, we performed a careful analysis of the galaxy cluster 1RXS J0603.3+4214 which hosts a bright large relic, known as the Toothbrush, and a giant elongated radio halo.

The cluster 1RXS J0603.3+4214 was observed with the VLA using A, B, C, and D configurations. The calibration of the wideband data is challenging and time consuming. The bright sources in the field need a high dynamic range and every calibration step should be done carefully. The data handing is also channelling. Thanks to the wide-band receivers, the final images showed a noise level that is very low. For a restoring beam of $1''$, we achieve a noise level of $2\,\mu\mathrm{Jy}$ over a broad frequency range of $1-2\,\mathrm{GHz}$. The wideband data lead to high sensitivity and permit high resolution imaging. This allowed us to reveal detailed structures that are surprisingly not smooth but may provide insight into magnetic fields.

Our new VLA observations provide the most detailed image of the Toothbrush so far, revealing enigmatic filamentary structures. We found that the bright brush part of the Toothbrush has a prominent narrow ridge with a clear sharp outer edge. The ridge has a width of about 25 kpc and branches to the west. The brush region is remarkably filamentary and consists of small arc-shaped filaments, 'bristles'. The complexity of the filamentary structures identified in the Toothbrush rule out the fact that radio relics are caused by a smooth shock surface. The spectral index map of the Toothbrush between $150\,\mathrm{MHz}$ and $1.5\,\mathrm{GHz}$ shows that the spectral index at the ridge is between -0.70 to -0.80, indicating a Mach number of $\mathcal{M} = 3.3^{+0.4}_{-0.3}$. We find a correlation between the spectral index map and the brightness across the northern edge of the Toothbrush. Our investigation shows that a uv-cut has a similar effect on VLA, GMRT, and LOFAR data. For the Toothbrush, we obtained an integrated spectral index of $\alpha = -1.15 \pm 0.05$, suggesting a Mach number of $\mathcal{M} = 3.8^{+0.3}_{-0.2}$.

The VLA L-band observations allowed us to investigate the polarization properties of the Toothbrush in detail. The fractional polarization increases towards the periphery in the frequency range of $1-2\,$GHz. The handle shows a high degree of polarization in L-band while the brush region of the Toothbrush is almost completely depolarized, indicating that it is located in a region where a significant amount of ICM lies in front and thus, depolarizes the emission. The fractional polarization across the B3 region decreases moderately towards longer wavelengths within the L-band. The B1 and B2 regions show complex Faraday spectra, suggesting that some of the Faraday depth distributions likely arise from the intracluster medium. The Rotation Measure (RM) synthesis analysis reveals that the filamentary features in the low density region (B3) show a shift in RM of about $+30\,\mathrm{rad\,m^{-2}}$. In denser regions (B2) the shifts increase to values of about $+50\,\mathrm{rad\,m^{-2}}$.

The radio morphology of the large central region of the halo shows a close similarity to the X-ray emitting gas, confirming the connection between the hot gas and relativistic plasma. We find that the radio brightness correlates well with the X-ray brightness in the central region of the halo. The derived power-law shows a slope of $b = 1.25 \pm 0.16$. The southernmost region of the halo appears distinct, indicating it may have a different origin. The average spectral index across the central region of the radio halo is $\alpha = -1.16 \pm 0.05$ and shows a slight gradient from north to south. In the southernmost part, the radio spectrum is steeper than the halo. The same region also shows a hint of a spectral index gradient, suggesting a possible connection with the southern shock detected in Chandra observations. The sensitive and high resolution radio map allowed us to identify 32 compact radio sources within the radio halo that were not detected previously. These sources will contribute $25\,\%$ of the flux measured for the halo, if not subtracted in low resolution radio maps.

For another cluster CIZA J0649.3+1801, we confirm the presence of a diffuse emission source. The cluster was observed with the WSRT telescope. We find that the source has a steep spectrum with spectral index of $\alpha = -1.30 \pm 0.04$ and shows a spectral gradient towards the cluster center, which is typical for relics. These observations revealed that at $1.5\,$GHz, the polarization fraction across the source varies between $5\,\%$ to $45\,\%$. This evidence suggests that it is a radio relic.

Bibliography

Ackermann, M. et al. (2014). "Search for Cosmic-Ray-induced Gamma-Ray Emission in Galaxy Clusters". In: ApJ 787, 18, p. 18. arXiv: 1308.5654 [astro-ph.HE].

Ackermann, M. et al. (2016). "Search for Gamma-Ray Emission from the Coma Cluster with Six Years of Fermi-LAT Data". In: ApJ 819, 149, p. 149. arXiv: 1507.08995 [astro-ph.HE].

Akamatsu, H. et al. (2012). "X-Ray View of the Shock Front in the Merging Cluster Abell 3376 with Suzaku". In: PASJ 64, 67, p. 67. arXiv: 1112.5955.

Andrei, A. H. et al. (2009). "The large quasar reference frame (LQRF). An optical representation of the ICRS". In: A&A 505, pp. 385–404. arXiv: 0907.2403.

Basu, K. (2012). "A Sunyaev-Zel'dovich take on cluster radio haloes - I. Global scaling and bi-modality using Planck data". In: MNRAS 421, pp. L112–L116. arXiv: 1111.2856 [astro-ph.CO].

Basu, K. et al. (2016). "The impact of the SZ effect on cm-wavelength (1-30 GHz) observations of galaxy cluster radio relics". In: A&A 591, A142, A142. arXiv: 1511.03245.

Becker, R. H., R. L. White, and A. L. Edwards (1991). "A new catalog of 53,522 4.85 GHz sources". In: ApJS 75, pp. 1–229.

Blandford, R. and D. Eichler (1987). "Particle acceleration at astrophysical shocks: A theory of cosmic ray origin". In: Phys. Rep. 154, pp. 1–75.

Blasi, P. (2000). "Stochastic Acceleration and Nonthermal Radiation in Clusters of Galaxies". In: ApJ 532, pp. L9–L12. eprint: astro-ph/0001344.

Blasi, P. and S. Colafrancesco (1999). "Cosmic rays, radio halos and nonthermal X-ray emission in clusters of galaxies". In: *Astroparticle Physics* 12, pp. 169–183. eprint: astro-ph/9905122.

Blumenthal, G. R. and R. J. Gould (1970). "Bremsstrahlung, Synchrotron Radiation, and Compton Scattering of High-Energy Electrons Traversing Dilute Gases". In: *Reviews of Modern Physics* 42, pp. 237–271.

Böhringer, H. et al. (2004). "The ROSAT-ESO Flux Limited X-ray (REFLEX) Galaxy cluster survey. V. The cluster catalogue". In: A&A 425, pp. 367–383. eprint: astro-ph/0405546.

Böhringer, Hans and Norbert Werner (2010). "X-ray spectroscopy of galaxy clusters: studying astrophysical processes in the largest celestial laboratories". In: *The Astronomy and Astrophysics Review* 18.1, pp. 127–196. URL: https://doi.org/10.1007/s00159-009-0023-3.

Bonafede, A. et al. (2009). "Double relics in Abell 2345 and Abell 1240. Spectral index and polarization analysis". In: A&A 494, pp. 429–442. arXiv: 0810.2223.

Bonafede, A. et al. (2012). "Discovery of radio haloes and double relics in distant MACS galaxy clusters: clues to the efficiency of particle acceleration". In: MNRAS 426, pp. 40–56. arXiv: 1206.6102.

Bonafede, A. et al. (2013). "Measurements and simulation of Faraday rotation across the Coma radio relic". In: MNRAS 433, pp. 3208–3226. arXiv: 1305.7228.

Bonafede, A. et al. (2017). "On the absence of radio haloes in clusters with double relics". In: MNRAS 470, pp. 3465–3475. arXiv: 1706.04203.

Brentjens, M. A. (2008). "Deep Westerbork observations of Abell 2256 at 350 MHz". In: A&A 489, pp. 69–83. arXiv: 0807.4467.

Brentjens, M. A. and A. G. de Bruyn (2005). "Faraday rotation measure synthesis". In: A&A 441, pp. 1217–1228. eprint: astro-ph/0507349.

Brown, S. and L. Rudnick (2011). "Diffuse radio emission in/around the Coma cluster: beyond simple accretion". In: MNRAS 412, pp. 2–12. arXiv: 1009.4258.

Brüggen, M., R. J. van Weeren, and H. J. A. Röttgering (2012). "Simulating the toothbrush: evidence for a triple merger of galaxy clusters". In: MNRAS 425, pp. L76–L80. arXiv: 1206.6118.

Brunetti, G. and T. W. Jones (2014). "Cosmic Rays in Galaxy Clusters and Their Nonthermal Emission". In: *International Journal of Modern Physics D* 23, 1430007-98, pp. 1430007–98. arXiv: 1401.7519.

Brunetti, G. et al. (2001). "Particle reacceleration in the Coma cluster: radio properties and hard X-ray emission". In: MNRAS 320, pp. 365–378. eprint: astro-ph/0008518.

Brunetti, G. et al. (2004). "Alfvénic reacceleration of relativistic particles in galaxy clusters: MHD waves, leptons and hadrons". In: MNRAS 350, pp. 1174–1194. eprint: astro-ph/0312482.

Brunetti, G. et al. (2012). "Probing the origin of giant radio haloes through radio and γ-ray data: the case of the Coma cluster". In: MNRAS 426, pp. 956–968. arXiv: 1207.3025 [astro-ph.HE].

Burn, B. J. (1966). "On the Depolarization of Discrete Radio Sources by Faraday Dispersion". In: *Monthly Notices of the Royal Astronomical Society* 133.1, pp. 67–83. eprint: /oup/backfile/content_public/journal/mnras/133/1/10.1093_mnras_133.1.67/2/mnras133-0067.pdf. URL: +http://dx.doi.org/10.1093/mnras/133.1.67.

Carilli, C. L. and G. B. Taylor (2002). "Cluster Magnetic Fields". In: ARA&A 40, pp. 319–348. eprint: astro-ph/0110655.

Cassano, R. et al. (2010). "On the Connection Between Giant Radio Halos and Cluster Mergers". In: ApJ 721, pp. L82–L85. arXiv: 1008.3624 [astro-ph.CO].

Cassano, R. et al. (2013). "Revisiting Scaling Relations for Giant Radio Halos in Galaxy Clusters". In: ApJ 777, 141, p. 141. arXiv: 1306.4379.

Clowe, D. et al. (2006). "A Direct Empirical Proof of the Existence of Dark Matter". In: ApJ 648, pp. L109–L113. eprint: astro-ph/0608407.

Condon, J. J. et al. (1998). "The NRAO VLA Sky Survey". In: AJ 115, pp. 1693–1716.

Cornwell, T. J., K. Golap, and S. Bhatnagar (2008). "The Noncoplanar Baselines Effect in Radio Interferometry: The W-Projection Algorithm". In: *IEEE Journal of Selected Topics in Signal Processing* 2, pp. 647–657. arXiv: 0807.4161.

Croston, J. H. et al. (2005). "An X-Ray Study of Magnetic Field Strengths and Particle Content in the Lobes of FR II Radio Sources". In: ApJ 626, pp. 733–747. eprint: astro-ph/0503203.

de Gasperin, F. et al. (2015). "A powerful double radio relic system discovered in PSZ1 G108.18-11.53: evidence for a shock with non-uniform Mach number?" In: MNRAS 453, pp. 3483–3498. arXiv: 1508.02901 [astro-ph.HE].

de Kool, M. and M. C. Begelman (1989). "Effects of thermal plasma on self-absorbed synchrotron sources in active galactic nuclei". In: ApJ 345, pp. 135–139.

Dennison, B. (1980). "Formation of radio halos in clusters of galaxies from cosmic-ray protons". In: ApJ 239, pp. L93–L96.

Dolag, K. and T. A. Enßlin (2000). "Radio halos of galaxy clusters from hadronic secondary electron injection in realistic magnetic field configurations". In: A&A 362, pp. 151–157. eprint: astro-ph/0008333.

Drury, L. O. (1983). "An introduction to the theory of diffusive shock acceleration of energetic particles in tenuous plasmas". In: *Reports on Progress in Physics* 46, pp. 973–1027.

Ebeling, H. et al. (1998). "The ROSAT Brightest Cluster Sample - I. The compilation of the sample and the cluster log N-log S distribution". In: MNRAS 301, pp. 881–914. eprint: astro-ph/9812394.

Ebeling, H., C. R. Mullis, and R. B. Tully (2002). "A Systematic X-Ray Search for Clusters of Galaxies behind the Milky Way". In: ApJ 580, pp. 774–788.

Eckert, D. et al. (2016). "A shock front at the radio relic of Abell 2744". In: MNRAS 461, pp. 1302–1307. arXiv: 1603.02272 [astro-ph.HE].

Eilek, J. A. and F. N. Owen (2002). "Magnetic Fields in Cluster Cores: Faraday Rotation in A400 and A2634". In: ApJ 567, pp. 202–220. eprint: astro-ph/0109177.

Ellison, D. C. and S. P. Reynolds (1991). "Electron acceleration in a nonlinear shock model with applications to supernova remnants". In: ApJ 382, pp. 242–254.

Enßlin, T. A. and M. Brüggen (2002). "On the formation of cluster radio relics". In: MNRAS 331, pp. 1011–1019. eprint: astro-ph/0104233.

Enßlin, T. A. and Gopal-Krishna (2001). "Are cluster radio relics revived fossil radio cocoons?" In: *Particles and Fields in Radio Galaxies Conference*. Ed. by R. A. Laing and K. M. Blundell. Vol. 250. Astronomical Society of the Pacific Conference Series, p. 454. eprint: astro-ph/0010600.

Ensslin, T. A. et al. (1998). "Cluster radio relics as a tracer of shock waves of the large-scale structure formation". In: A&A 332, pp. 395–409. eprint: astro-ph/9712293.

Ettori, S. et al. (2013). "Mass Profiles of Galaxy Clusters from X-ray Analysis". In: Space Sci. Rev. 177, pp. 119–154. arXiv: 1303.3530.

Feretti, L. et al. (1995). "The magnetic field in the Coma cluster." In: A&A 302, p. 680. eprint: astro-ph/9504058.

Feretti, L. et al. (1999). "The radio galaxies and the magnetic field in Abell 119". In: A&A 344, pp. 472–482. eprint: astro-ph/9902019.

Feretti, L. et al. (2001). "The giant radio halo in Abell 2163". In: A&A 373, pp. 106–112. eprint: astro-ph/0104451.

Feretti, L. et al. (2004a). "Properties and Spectral Behaviour of Cluster Radio Halos". In: *Journal of Korean Astronomical Society* 37, pp. 315–322. eprint: astro-ph/0412424.

Feretti, L. et al. (2004b). "Spectral index maps of the radio halos in Abell 665 and Abell 2163". In: A&A 423, pp. 111–119. eprint: astro-ph/0404283.

Feretti, L. et al. (2012). "Clusters of galaxies: observational properties of the diffuse radio emission". In: A&A Rev. 20, 54, p. 54. arXiv: 1205.1919.

Ferrari, C. et al. (2008). "Observations of Extended Radio Emission in Clusters". In: Space Sci. Rev. 134, pp. 93–118. arXiv: 0801.0985.

Ficarra, A., G. Grueff, and G. Tomassetti (1985). "A new Bologna sky survey at 408 MHz". In: A&AS 59, pp. 255–347.

Fujita, Y. and C. L. Sarazin (2001). "Nonthermal Emission from Accreting and Merging Clusters of Galaxies". In: ApJ 563, pp. 660–672. eprint: astro-ph/0108369.

Giacintucci, S. et al. (2005). "Spectral properties and origin of the radio halo in A3562". In: A&A 440, pp. 867–879. eprint: astro-ph/0505614.

Giacintucci, S. et al. (2008). "Shock acceleration as origin of the radio relic in A 521?" In: A&A 486, pp. 347–358. arXiv: 0803.4127.

Giovannini, G. et al. (2009). "Radio halos in nearby (z 0.4) clusters of galaxies". In: A&A 507, pp. 1257–1270. arXiv: 0909.0911.

Govoni, F. and L. Feretti (2004). "Magnetic Fields in Clusters of Galaxies". In: *International Journal of Modern Physics D* 13, pp. 1549–1594. eprint: astro-ph/0410182.

Govoni, F. et al. (2001a). "A comparison of radio and X-ray morphologies of four clusters of galaxies containing radio halos". In: A&A 369, pp. 441–449. eprint: astro-ph/0101418.

Govoni, F. et al. (2001b). "Radio and X-ray diffuse emission in six clusters of galaxies". In: A&A 376, pp. 803–819. eprint: astro-ph/0107275.

Govoni, F. et al. (2005). "A2255: The first detection of filamentary polarized emission in a radio halo". In: A&A 430, pp. L5–L8. eprint: astro-ph/0411720.

Govoni, F. et al. (2017). "Sardinia Radio Telescope observations of Abell 194. The intracluster magnetic field power spectrum". In: A&A 603, A122, A122. arXiv: 1703.08688.

Gregory, P. C. and J. J. Condon (1991). "The 87GB catalog of radio sources covering delta between O and + 75 deg at 4.85 GHz". In: ApJS 75, pp. 1011–1291.

Hardcastle, M. J. and J. H. Croston (2005). "The Chandra view of extended X-ray emission from Pictor A". In: MNRAS 363, pp. 649–660. eprint: astro-ph/0507694.

Heald, G. (2009). "The Faraday rotation measure synthesis technique". In: *IAU Symposium*. Ed. by K. G. Strassmeier, A. G. Kosovichev, and J. E. Beckman. Vol. 259. IAU Symposium, pp. 591–602.

Hoang, D. N. et al. (2017). "Deep LOFAR observations of the merging galaxy cluster CIZA J2242.8+5301". In: *ArXiv e-prints*. arXiv: 1706.09903.

Hoeft, M. and M. Brüggen (2007). "Radio signature of cosmological structure formation shocks". In: MNRAS 375, pp. 77–91. eprint: astro-ph/0609831.

Hudson, D. S. et al. (2010). "What is a cool-core cluster? a detailed analysis of the cores of the X-ray flux-limited HIFLUGCS cluster sample". In: A&A 513, A37, A37. arXiv: 0911.0409.

Jõeveer, M., J. Einasto, and E. Tago (1978). "Spatial distribution of galaxies and of clusters of galaxies in the southern galactic hemisphere". In: MNRAS 185, pp. 357–370.

Jaffe, W. J. (1977). "Origin and transport of electrons in the halo radio source in the Coma cluster". In: ApJ 212, pp. 1–7.

Jee, M. J. et al. (2016). "MC2: Mapping the Dark Matter Distribution of the "Toothbrush" Cluster RX J0603.3+4214 with Hubble Space Telescope and Subaru Weak Lensing". In: ApJ 817, 179, p. 179. arXiv: 1510.03486.

Jeltema, T. E. and S. Profumo (2011). "Implications of Fermi Observations For Hadronic Models of Radio Halos in Clusters of Galaxies". In: ApJ 728, 53, p. 53. arXiv: 1006.1648.

Kale, R. et al. (2012). "Spectral and polarization study of the double relics in Abell 3376 using the Giant Metrewave Radio Telescope and the Very Large Array". In: MNRAS 426, pp. 1204–1211. arXiv: 1206.3389.

Kang, H. and D. Ryu (2011). "Re-acceleration of Non-thermal Particles at Weak Cosmological Shock Waves". In: ApJ 734, 18, p. 18. arXiv: 1102.2561.

Kang, H., D. Ryu, and T. W. Jones (2012). "Diffusive Shock Acceleration Simulations of Radio Relics". In: ApJ 756, 97, p. 97. arXiv: 1205.1895 [astro-ph.HE].

Katz-Stone, D. M., L. Rudnick, and M. C. Anderson (1993). "Determining the shape of spectra in extended radio sources". In: ApJ 407, pp. 549–555.

Kellermann, K. I. (1966). "The radio source 1934-63". In: *Australian Journal of Physics* 19, p. 195.

Kellermann, K. I. and I. I. K. Pauliny-Toth (1968). "Further Observations of Variable Radio Sources". In: ApJ 152, p. 639.

Kempner, J. C. et al. (2004). "Conference Note: A Taxonomy of Extended Radio Sources in Clusters of Galaxies". In: *The Riddle of Cooling Flows in Galaxies and Clusters of galaxies*. Ed. by T. Reiprich, J. Kempner, and N. Soker, p. 335. eprint: astro-ph/0310263.

Kierdorf, M. et al. (2016). "Relics in galaxy clusters at high radio frequencies". In: *ArXiv e-prints*. arXiv: 1612.01764.

Kim, K.-T. (1990). "On the origin of the radio halo in the Coma cluster of galaxies." In: *Nuovo Cimento B Serie* 105, pp. 845–856.

Kocevski, D. D. et al. (2007). "A Systematic X-Ray Search for Clusters of Galaxies behind the Milky Way. II. The Second CIZA Subsample". In: ApJ 662, pp. 224–235. eprint: astro-ph/0512321.

Komissarov, S. S. and A. G. Gubanov (1994). "Relic radio galaxies: evolution of synchrotron spectrum". In: A&A 285, pp. 27–43.

Kraan-Korteweg, R. C. and O. Lahav (2000). "The Universe behind the Milky Way". In: A&A Rev. 10, pp. 211–261. eprint: astro-ph/0005501.

Lane, W. M. et al. (2012). "VLSS redux: Software improvements applied to the Very Large Array Low-Frequency Sky Survey". In: *Radio Science* 47, RS0K04, RS0K04. arXiv: 1205.4695 [astro-ph.IM].

Large, M. I., D. S. Mathewson, and C. G. T. Haslam (1959). "A High-Resolution Survey of the Coma Cluster of Galaxies at 408 Mc./s." In: Nature 183, pp. 1663–1664.

Liang, H. et al. (2000). "A Powerful Radio Halo in the Hottest Known Cluster of Galaxies 1E 0657-56". In: ApJ 544, pp. 686–701. eprint: astro-ph/0006072.

Lindner, R. R. et al. (2014). "The Radio Relics and Halo of El Gordo, a Massive z = 0.870 Cluster Merger". In: ApJ 786, 49, p. 49. arXiv: 1310.6786.

Longair, M. S. (1981). *High energy astrophysics*.

Macario, G. et al. (2011). "A Shock Front in the Merging Galaxy Cluster A754: X-ray and Radio Observations". In: ApJ 728, 82, p. 82. arXiv: 1010.5209.

Mann, A. W. and H. Ebeling (2012). "X-ray-optical classification of cluster mergers and the evolution of the cluster merger fraction". In: MNRAS 420, pp. 2120–2138. arXiv: 1111.2396.

Marecki, A. et al. (1999). "Gigahertz Peaked Spectrum sources from the Jodrell Bank-VLA Astrometric Survey. I. Sources in the region 35degr = delta = 75degr". In: A&AS 135, pp. 273–289. eprint: astro-ph/9811128.

Mazzotta, P. and S. Giacintucci (2008). "Do Radio Core-Halos and Cold Fronts in Non-Major-Merging Clusters Originate from the Same Gas Sloshing?" In: ApJ 675, L9, p. L9. arXiv: 0801.1905.

McMullin, J. P. et al. (2007). "CASA Architecture and Applications". In: *Astronomical Data Analysis Software and Systems XVI*. Ed. by R. A. Shaw, F. Hill, and D. J. Bell. Vol. 376. Astronomical Society of the Pacific Conference Series, p. 127.

Miniati, F. et al. (2000). "Properties of Cosmic Shock Waves in Large-Scale Structure Formation". In: ApJ 542, pp. 608–621. eprint: astro-ph/0005444.

Mohan, N. and D. Rafferty (2015). *PyBDSM: Python Blob Detection and Source Measurement*. Astrophysics Source Code Library. ascl: 1502.007.

Molendi, S. and F. Pizzolato (2001). "Is the Gas in Cooling Flows Multiphase?" In: ApJ 560, pp. 194–200. eprint: astro-ph/0106552.

O'Dea, C. P. (1998). "The Compact Steep-Spectrum and Gigahertz Peaked-Spectrum Radio Sources". In: PASP 110, pp. 493–532.

Offringa, A. R. et al. (2010). "Post-correlation radio frequency interference classification methods". In: MNRAS 405, pp. 155–167. arXiv: 1002.1957 [astro-ph.IM].

Ogrean, G. A. et al. (2013). "Challenges to our understanding of radio relics: X-ray observations of the Toothbrush cluster". In: MNRAS 433, pp. 812–824. arXiv: 1303.1533.

Orrú, E. et al. (2007). "Low-frequency study of two clusters of galaxies: A2744 and A2219". In: A&A 467, pp. 943–954. eprint: astro-ph/0701776.

Owen, F. N. et al. (2014). "Wideband Very Large Array Observations of A2256. I. Continuum, Rotation Measure, and Spectral Imaging". In: ApJ 794, 24, p. 24. arXiv: 1408.5931.

Owers, M. S. et al. (2011). "The Dissection of Abell 2744: A Rich Cluster Growing Through Major and Minor Mergers". In: ApJ 728, 27, p. 27. arXiv: 1012.1315.

Patnaik, A. R. et al. (1992). "Interferometer phase calibration sources. I - The region 35-75 deg". In: MNRAS 254, pp. 655–676.

Pearce, C. J. J. et al. (2017). "VLA Radio Observations of the HST Frontier Fields Cluster Abell 2744: The Discovery of New Radio Relics". In: *ArXiv e-prints*. arXiv: 1708.03367.

Perley, R. A. and B. J. Butler (2013). "An Accurate Flux Density Scale from 1 to 50 GHz". In: ApJS 204, 19, p. 19. arXiv: 1211.1300 [astro-ph.IM].

Perley, R. A. and G. B. Taylor (1991). "VLA observations of 3C 295 - A young radio galaxy?" In: AJ 101, pp. 1623–1631.

Petrosian, V. (2001). "On the Nonthermal Emission and Acceleration of Electrons in Coma and Other Clusters of Galaxies". In: ApJ 557, pp. 560–572. eprint: astro-ph/0101145.

Pinzke, A., S. P. Oh, and C. Pfrommer (2013). "Giant radio relics in galaxy clusters: reacceleration of fossil relativistic electrons?" In: MNRAS 435, pp. 1061–1082. arXiv: 1301.5644 [astro-ph.CO].

Pizzo, R. F. et al. (2011). "Deep multi-frequency rotation measure tomography of the galaxy cluster A2255". In: A&A 525, A104, A104. arXiv: 1008.3530.

Pratley, L. et al. (2013). "Using head-tail galaxies to constrain the intracluster magnetic field: an in-depth study of PKS J0334-3900". In: MNRAS 432, pp. 243–257. arXiv: 1303.2847.

Rajpurohit, K. et al. (2017). "Deep VLA observations of the cluster 1RXS J0603.3+4214 in the frequency range 1 to 2 GHz". In: *ArXiv e-prints*. arXiv: 1712.01327.

Rau, U. and T. J. Cornwell (2011). "A multi-scale multi-frequency deconvolution algorithm for synthesis imaging in radio interferometry". In: A&A 532, A71, A71. arXiv: 1106.2745 [astro-ph.IM].

Reiprich, T. H. and H. Böhringer (2002). "The Mass Function of an X-Ray Flux-limited Sample of Galaxy Clusters". In: ApJ 567, pp. 716–740. eprint: astro-ph/0111285.

Rephaeli, Y. (1979). "Relativistic electrons in the intracluster space of clusters of galaxies - The hard X-ray spectra and heating of the gas". In: ApJ 227, pp. 364–369.

Rosati, P. (1997). "A serendipitous deep cluster survey from ROSAT-PSPC pointed observations." In: *Astrophysical Letters and Communications* 36, pp. 205–210.

Rottgering, H. J. A. et al. (1997). "The extended radio emission in the luminous X-ray cluster A3667". In: MNRAS 290, pp. 577–584.

Rybicki, G. B. and A. P. Lightman (1979). *Radiative processes in astrophysics.*

– (1985). *Radiative processes in astrophysics.*

Ryu, D. et al. (2003). "Cosmological Shock Waves and Their Role in the Large-Scale Structure of the Universe". In: ApJ 593, pp. 599–610. eprint: astro-ph/0305164.

Sarazin, C. L. (1999). "The Energy Spectrum of Primary Cosmic-Ray Electrons in Clusters of Galaxies and Inverse Compton Emission". In: ApJ 520, pp. 529–547. eprint: astro-ph/9901061.

Sarazin, C. L., A. Finoguenov, and D. R. Wik (2013). "Merger shocks in Abell 3667 and the Cygnus A cluster". In: *Astronomische Nachrichten* 334, p. 346. arXiv: 1211.4823.

Shimwell, T. W. et al. (2014). "Deep radio observations of the radio halo of the bullet cluster 1E 0657-55.8". In: MNRAS 440, pp. 2901–2915. arXiv: 1403.2393.

Shimwell, T. W. et al. (2015). "Another shock for the Bullet cluster, and the source of seed electrons for radio relics". In: MNRAS 449, pp. 1486–1494. arXiv: 1502.01064 [astro-ph.HE].

Sokoloff, D. D. et al. (1998). "Depolarization and Faraday effects in galaxies". In: MN-RAS 299, pp. 189–206.

Springel, V. et al. (2005). "Simulations of the formation, evolution and clustering of galaxies and quasars". In: Nature 435, pp. 629–636. eprint: astro-ph/0504097.

Stroe, A. et al. (2013). "Discovery of spectral curvature in the shock downstream region: CIZA J2242.8+5301". In: A&A 555, A110, A110. arXiv: 1305.0005.

Stroe, A. et al. (2016). "The widest frequency radio relic spectra: observations from 150 MHz to 30 GHz". In: MNRAS 455, pp. 2402–2416. arXiv: 1510.06739.

Sunyaev, R. A. and Y. B. Zeldovich (1972). "The Observations of Relic Radiation as a Test of the Nature of X-Ray Radiation from the Clusters of Galaxies". In: *Comments on Astrophysics and Space Physics* 4, p. 173.

Tribble, P. C. (1991). "Depolarization of extended radio sources by a foreground Faraday screen". In: MNRAS 250, pp. 726–736.

Uchida, Y. et al. (2016). "Suzaku observations of a shock front tracing the western edge of the giant radio halo in the Coma Cluster". In: PASJ 68, S20, S20. arXiv: 1509.01901 [astro-ph.HE].

Vacca, V. et al. (2014). "Spectral index image of the radio halo in the cluster Abell 520, which hosts the famous bow shock". In: A&A 561, A52, A52. arXiv: 1310.2870.

van Weeren, R. J. et al. (2010). "Particle Acceleration on Megaparsec Scales in a Merging Galaxy Cluster". In: *Science* 330, pp. 347–. arXiv: 1010.4306 [astro-ph.CO].

van Weeren, R. J. et al. (2011). "Radio continuum observations of new radio halos and relics from the NVSS and WENSS surveys. Relic orientations, cluster X-ray luminosity, and redshift distributions". In: A&A 533, A35, A35. arXiv: 1107.5597.

van Weeren, R. J. et al. (2012a). "The "toothbrush-relic": evidence for a coherent linear 2-Mpc scale shock wave in a massive merging galaxy cluster?" In: A&A 546, A124, A124. arXiv: 1209.2196.

– (2012b). "The "toothbrush-relic": evidence for a coherent linear 2-Mpc scale shock wave in a massive merging galaxy cluster?" In: A&A 546, A124, A124. arXiv: 1209.2196.

van Weeren, R. J. et al. (2016). "LOFAR, VLA, and Chandra Observations of the Toothbrush Galaxy Cluster". In: ApJ 818, 204, p. 204. arXiv: 1601.06029 [astro-ph.HE].

van Weeren, R. J. et al. (2017a). "Chandra and JVLA observations of HST Frontier Fields cluster MACS J0717.5+3745". In: *ArXiv e-prints*. arXiv: 1701.04096.

van Weeren, R. J. et al. (2017b). "The case for electron re-acceleration at galaxy cluster shocks". In: *Nature Astronomy* 1, 0005, p. 0005. arXiv: 1701.01439 [astro-ph.HE].

Vazza, F. and M. Brüggen (2014). "Do radio relics challenge diffusive shock acceleration?" In: MNRAS 437, pp. 2291–2296. arXiv: 1310.5707.

Vazza, F. et al. (2014). "On the amplification of magnetic fields in cosmic filaments and galaxy clusters". In: MNRAS 445, pp. 3706–3722. arXiv: `1409.2640`.

Venturi, T. et al. (2013). "Low frequency follow up of radio haloes and relics in the GMRT Radio Halo Cluster Survey". In: A&A 551, A24, A24. arXiv: `1210.7617`.

Voges, W. et al. (1999). "The ROSAT all-sky survey bright source catalogue". In: A&A 349, pp. 389–405. eprint: `astro-ph/9909315`.

Ehrenwörtliche Erklärung

Ich erkläre hiermit ehrenwörtlich, dass ich die vorliegende Arbeit selbstständig, ohne unzulässige Hilfe Dritter und ohne Benutzung anderer als der angegebenen Hilfsmittel und Literatur angefertigt habe. Die aus anderen Quellen direkt oder indirekt übernommenen Daten und Konzepte sind unter Angabe der Quelle gekennzeichnet.

Bei der Auswahl und Auswertung folgenden Materials haben mir die nachstehend aufgeführten Personen in der jeweils beschriebenen Weise entgeltlich/unentgeltlich geholfen:

1. Dr. Matthias Hoeft − Betreuung der vorliegenden Arbeit.

2. Dr. Reinout van Weeren − Zuververfügungstellung der VLA L-Band Beobachtung und Unterstützung bei der Kalibration der Daten.

3. Prof. Lawrence Rudnick − Hilfe bei der wissenschaftlichen Untersuchung und Interpretation des Magnetfelds des „Toothbrush"-Relikts.

Weitere Personen waren an der inhaltlich-materiellen Erstellung der vorliegenden Arbeit nicht beteiligt. Insbesondere habe ich hierfür nicht die entgeltliche Hilfe von Vermittlungs-beziehungsweise Beratungsdiensten (Promotionsberater oder andere Personen) in Anspruch genommen.

Niemand hat von mir unmittelbar oder mittelbar geldwerte Leistungen für Arbeiten erhalten, die im Zusammenhang mit dem Inhalt der vorgelegten Dissertation stehen.

Diese Arbeit ist weder im In-noch im Ausland in gleicher noch in ähnlicher Fassung Bestandteil einer anderen Studien-oder Prüfungsleistung.

Die geltende Promotionsordnung der Physikalisch-Astronomischen Fakultät der Friedrich-Schiller-Universität Jena ist mir bekannt.

Ich versichere ehrenwörtlich, dass ich nach bestem Wissen die reine Wahrheit gesagt und nichts verschwiegen habe.

Tautenburg, den 6 Februar 2018

_____

Kamlesh Rajpurohit

Publications

1. **Rajpurohit, K**, M. Hoeft, R. J. van Weeren, L. Rudnick, H. J. A. Röttgering, W. R. Forman, M. Brüggen, J. H. Croston, F. Andrade-Santos, W. A. Dawson, H. T. Intema, R. P. Kraft, C. Jones, and M. James Jee. Deep VLA Observations of the Cluster 1RXS J0603.3+4214 in the Frequency Range of 1-2 GHz, *The Astrophysical Journal*, 852, 65 (2018)

2. Singal, A. K. and **Rajpurohit, K**. Dependence of Fanaroff-Riley break of radio galaxies on luminosity and redshift, *Astrophysics and Space Science*, 353, 233 (2014)

3. Singal, A. K. and **Rajpurohit, K**. Fanaroff-Riley dichotomy of radio galaxies and the Malmquist bias, *Monthly notices of the Royal Astronomical Society*, 442, 1656 (2014)

4. Molera Calves, G. Cimo, G. Pogrebenko, S. V. Duev, D., Bocanegra-Baham., **Rajpurohit, K.** Scintillation of Venus and Mars Express radio signal on interplanetary and ionosphere plasma, *Proceedings of the 12th European VLBI Network Symposium and Users Meeting (EVN 2014)*.

Talks

2017

– Deep L-band VLA observations of the Toothbrush cluster. *Diffuse Synchrotron Emission in Clusters of Galaxies - What's Next?*, Leiden, October 2017.

– Deep L-band VLA observations of the Toothbrush cluster. *GLOW Annual Assembly and GLOW-SKA Meeting*, Würzburg, October 2017.

– LOFAR, GMRT and JVLA study of the Toothbrush: filaments and inhomogeneous. *National Astronomy Meeting - LOFAR session*, Hull, England, July 2017.

– A spectacular view of the Toothbrush: filaments and inhomogeneous magnetic fields. *The Broad Impact of Low Frequency Observing and the 4th LOFAR Users Meeting*, Bologna, Italy, June 2017.

– VLA observations of the Toothbrush cluster. Colloquium, *Thüringer Landessternwarte Tautenburg*, Germany, June 2017.

– The Toothbrush relic at high resolution. *Diffuse Emission in Galaxy Clusters FOR 1254 Meeting 2017*, Garching, May 2017.

2016

– The Toothbrush radio relic in high resolution. *GLOW Annual Assembly 2016, Leibniz-Institut für Astrophysik Potsdam*, Germany, December 2016.

– The high resolution JVLA view of Toothbrush Relic. *Annual Meeting of the DFG Research Unit 1254*, Berlin-Dahlem, Germany, September 2016.

2015

– Diffuse radio emission in galaxy clusters. *Physical Research Laboratory (PRL)*, Ahmedabad, India, December 2015.

– Diffuse radio emission in CIZA J0649+18. Poster presentation at *the Magnetic Fields in the Universe V conference*, Corsica, France, October 2015.

– Diffuse radio emission in CIZA J0649+18. *Astronomical Society 88th Annual Meeting*, Kiel, September 2015.

– A radio relic in CIZA J0649.3+1801? *45th Young European Radio Astronomy Conference*, Ventspils, Latvia, August 2015.

– A radio relic in CIZA J0649.3+1801? *Annual Meeting of the DFG Research Unit 1254*, Schloss Ringberg, July 2015.

– Diffuse Radio Emission in Galaxy Clusters. *TLS-Bamberg Joint Seminar*, Bamberg, Germany, June 2015.

– Radio relic in CIZA J0649+18. *Workshop of the Clusters Group of the Forschergruppe Cosmic Magnetism*, Hamburg-Bergedorf, Germany, March 2015

2014

– Scintillation of radio emissions from planetary spacecraft and The radio relic in CIZA J0649.3+1801. *Annual Meeting of the DFG Research Unit 1254*, Eitrof, Germany, September 2014.

– Scintillation of radio emissions from planetary spacecraft. *ASTRON summer school 2014*, Dwingeloo, August 2014.